Material Properties and Microstructures of Electron Beam Welding Similar and Dissimilar Titanium Alloys.

Ryan Mitchell

A thesis submitted in partial fulfilment of the

Master of Engineering (ME)

AUT

U N I V E R S I T Y

TE WĀNANGA ARONUI O TAMAKI MAKAU RAU

School of Engineering

AUT University

2011

Table of Contents

List of Figures

List of Tables

Nomenclature

Al_{eq} -   Aluminium Equivalent

Mo_{eq} -   Molybdenum Equivalent

HCP   -   Hexagonally Close Packed lattice structure of atoms

BCC   -   Body Centred Cubic lattice structure of atoms

FCC   -   Face Centred Cubic lattice structure of atoms

σ_{UTS} -   Ultimate tensile strength

$\sigma_{Y_{0.2}}$ -   0.2% Yield strength

e_t -   Elongation % (tensile)

e_b -   Elongation % (bending)

M_s -   Martensitic start temperature

α   -   HCP titanium phase

β   -   BCC titanium phase

ω   -   Trigonal or hexagonal (not HCP) crystallographic phase

β'   -   Second bcc phase exhibited as a result of a miscibility gap in solubility of molybdenum (Mo) in titanium.

$α_2$ -   Hexagonal ordered Ti_3Al intermetallic phase

γ   -   FCC TiAl intermetallic phase

α'   -   Hexagonal martensite phase

α"   -   Orthorhombic martensite phase

Attestation of Authorship

I hereby declare this submission is my own work and that, to the best of my knowledge and belief, it contains no material previously published or written by another person (except where explicitly defined in the acknowledgements), nor material to a substantial extent has been submitted for the award of any other degree or diploma of a university or other institute of higher learning

Name: <u>Ryan James Mitchell</u>

Signed: _____

Date: _____

List of Co-authored Publications

Mitchell, R.M., Short, A.B., Pasang, T., Littlefair, G., *Characteristics of Electron Beam Welded Ti & Ti alloys*. in *SIF 2010*. 2010. Auckland University, New Zealand

Pasang, T., Sabol, J.C., Misiolek, W.Z., Mitchell, R.M., Short, A.B., *Strain Distribution in Tensile Test of Electron Beam Welded Dissimilar Titanium Alloys*. in *ASMET 2011*. 2011. Planneralm, Austria.

Pasang, T., Sabol, J.C., Misiolek, W.Z., Mitchell, R.M., Short, A.B., Littlefair, G., *Metallurgical Characterization of Deformed Electron Beam Welded Dissimilar Titanium Alloys*, in *ICTP 2011*. 2011: Aachen, Germany. (Also to be published in Steel Research Institute Journal, 2011).

Pasang, T., Sabol, J.C., Misiolek, W.Z. Mitchell, R.M., Short, A.B., Littlefair, G., Thome, A.J., *Metallurgy and Deformation of Electron Beam Welded Similar Titanium Alloys*. in *MESIC 2011*. 2011. Cadiz, Spain.

Acknowledgements

I would like to take this opportunity to thank a number of the people, whose help has allowed this project to be successful.

Abstract

Titanium is considered one of the best engineering materials for industrial applications with the different alloys offering a range of properties, which include low density, high fatigue life, corrosion resistance and high strength. Electron beam welding (EBW) is a high energy density welding process that occurs in an inert high vacuum environment. Welding of dissimilar metals or alloys offers the opportunity to take advantage of different material properties in different areas of a single part.

The research aim of this master's project was to identify the properties and microstructure of electron beam welding similar and dissimilar titanium alloys.

Similar and dissimilar titanium alloy butt joint welds were created using an electron beam process. The welds consisted of commercially pure titanium (CP Ti), $\alpha+\beta$ alloy Ti6Al4V (Ti64) and β alloy Ti5Al5V5Mo3Cr (Ti5553). Microstructure was studied through the use of metallography and optical microscopy. Electron microprobe microanalysis (EPMA) was performed to identify the chemical composition across the welded samples. Mechanical testing was performed on welded samples to study the joint integrity and fracture characteristics. A scanning electron microscope investigation was performed on the fracture surface to reveal their fracture modes.

Visually acceptable crack free electron beam welds were achieved for all similar and dissimilar combinations of titanium alloys. EPMA (electron microprobe microanalysis) scans showed that the dissimilar welds were well mixed with consistent composition across their fusion zones. Microhardness profiles of similarly welded CP Ti and Ti64 showed no significant change of the hardness in HAZ or fusion zones. Similarly welded Ti5553 alloy microhardness profiles showed softening in the HAZ and fusion zones. Dissimilar welds with Ti5553 showed a significant increase in hardness in the fusion zone.

Most weldments exhibited mechanical properties comparable to the base metal, with negligible loss in ductility exhibited during tensile testing. Ti5553 to Ti64 and Ti5553 to Ti5553 weldments both failed prematurely below the tensile strength of both materials and exhibited very little elongation. Porosity was observed in the Ti5553 to Ti64 fusion zone.

Early investigation using the Aramis system showed some confidence of significant elongation occurring in the fusion zones of similar and dissimilarly electron beam welded Ti5553.

1.0   Introduction

1.1   Electron Beam Welding Overview

1.1.1   The Beginnings of Electron Beam Welding

It had been known since the early 1900's that a beam of electrons accelerated in a vacuum would induce heating in a target upon which the beam hit. Before the 1950's some experimental machines had been developed that could perform melting, drilling and spot welds, but no commercial need had been identfied for the electron beam technology [1, 2].

Electron beam welding arose as a viable industrial process in the 1950's as an answer to welding refractory metals for the nuclear industry. Due to some of their beneficial properties refractory metals were identified as potential canning materials for the uranic fuels. The problem that refractory materials face is that impurities in its fusion welds decrease corrosion resistance, strength and ductility. Refractory materials are extremely reactive with oxygen and nitrogen at temperatures over 300°C so an inert environment for welding is required. Inert gas shielding techniques of the time were not sufficient to produce welds without large impurity levels, and it was found that the best results, while using shielding gas, were achieved after pre-weld evacuation (vacuum) of the vessels. It was identified that a complete vacuum environment would provide less potential for impurity contamination than the best shield gas environment could. Arc welding, and other contemporary welding methods could not operate in a vacuum environment so a new welding technology was required [1, 2].

In 1957 Dr J. A. Stohr, of the French atomic energy commission, published the first electron beam welding development. This early EBW machine operated at 15kV, using electrostatic focusing and with the work piece as the anode. This first machine produced a weld with a neat uniform external appearance and depth to width ratios double that of TIG welds of the age [1, 2].

In 1958 German electron beam melting researchers, who had independently been working in parallel to Stohr, used a 125kV, 2.5kW machine to demonstrate much higher depth to width ratios than that of Stohr's. This was the first time the potential of deep penetration EBW was highlighted [1, 2].

Most early machines used a fixed beam position in the vacuum chamber, but in 1959 the first mobile gun within the vacuum chamber was produced [1, 2].

Around 1960, Hamilton Standard, a division of United Aircraft, took an interest in electron beam welding technology as aerospace and aero engine industries began to develop. The aerospace industry is one of the main non-nuclear users of EBW and the industry has driven a lot of the development of the technique and technology to present day [1, 2].

1.1.2 Electron Beam Welding Process

Electron beam welding is performed by concentrating a beam of high energy electrons onto a seam or surface of fusible material. The electrons in the beam create heat when they strike any matter in their path transferring their energy to the target material. By moving either the electron beam or the target work piece along a weld seam, the beam melts a narrow zone of parent metal, leaving a uniform high purity weld behind it [3].

Using an electron beam as a heat source for fusion welding demonstrates a number of distinctive characteristics compared to other fusion welding heat sources. Electron beam welding generally occurs in a high vacuum environment [3-5]. Usually welding is performed without the use of filler wire or other added material making autogenous welds [3]. At high energies the beam can produce welds with up to 20:1 depth-to-width ratios. As a result of the high depth to width ratios of the fusion zones, electron beam welds have minimal heat affected zones (HAZ) with minimal distortion of the substrates. The welds are of a constant high quality, often the highest achieved by fusion welding processes [3, 5].

Electron beam welding machines offer precise control over the beam power output, which can be also be varied over an extremely wide range on the same machine. The thermal energy is transferred to the work piece in a highly localised manner and a high percentage of the beam's energy, up to 90%, is transferred to the substrate [3-5]. The beam can be easily shaped, defocused, deflected, oscillated or split and as electron beam welding controls are automated the beam power and path are highly repeatable [3].

1.2 Introduction to Titanium

1.2.1 The Place in Industry for Titanium

Titanium is the fourth most abundant structural metal and ninth among all elements present on the earths surface [6, 7]. Titanium and its alloys began to be used commercially in the early 1950s and as it is available in a range of high specific strengths with various beneficial material properties, such as high fatigue life, toughness, excellent resistance to corrosion and low density, leads to it being considered one of the best engineering materials for industrial application [2, 3, 6, 8-11]. The mechanical properties of these alloys are strongly dependent on chemical composition and thermo-mechanical processing [12].

Titanium is highly reactive with oxygen, as a result when the bare metal is exposed to air at room temperature an immediate stable and adherent oxide layer is formed. This oxide layer gives titanium excellent corrosion resistance at temperatures up to 600°C when the oxide layer allows high levels of oxygen defusion through it [6, 13].

The high cost of production and difficulty processing titanium has limited the use of titanium to certain niche applications [6, 14]. The largest consumer of titanium alloys is the aerospace industry though in recent years, the proportion of titanium and its alloys being used has increased in a range of areas including: chemical machine building, shipbuilding, the auto industry, equipment for the oil and gas industry, the food

industry, medical, and civil engineering [15, 16]. Some of the desirable characteristics for titanium selection for different industrial uses are shown in Figure 1-1.
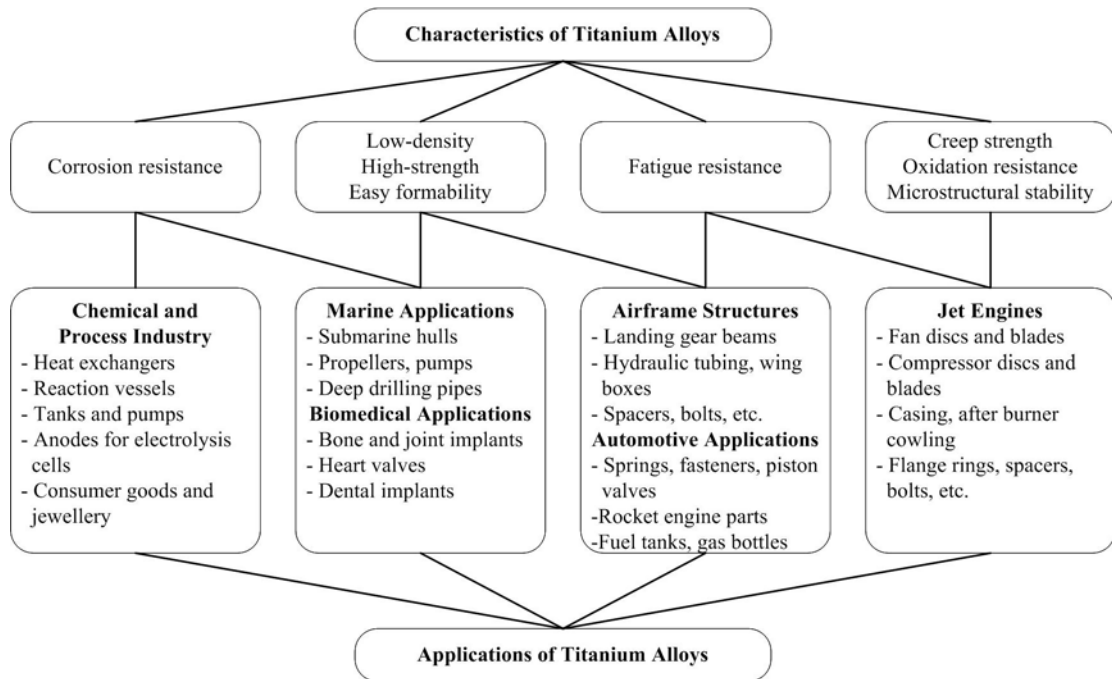
Figure 1-1: General characteristics and typical applications of titanium alloys [17].

1.2.2 Element Identification/Raw Material

In 1791 William Gregor was the first person to report the presence of an unknown element in magnetic iron sand (ilmenite). Four years later Martin Klaproth independently analysed rutile and identified an oxide of the same element reported by Gregor. Klaproth poetically named the element titanium after the great Greek mythical titans who were gods held captive in the earth's crust, similar to the hard to extract ore [6, 7].

Estimates assume a worldwide reserve of titanium oxide of 650 billion metric tons [7]. Figure 1-2 shows the distribution of titanium oxide worldwide. Titanium oxide occurs in a number of forms in nature, these are ilmenite ($FeTiO_3$), rutile (tetragonal TiO_2), anatase (tetragonal TiO_2), brookite (rhombic TiO_2), perovskite ($CaTiO_3$), sphene ($CaTiSiO_5$) and geikielite ($MgTiO_3$) [18]. The most common and important mineral sources for titanium refinement are ilmenite and rutile [6, 18].
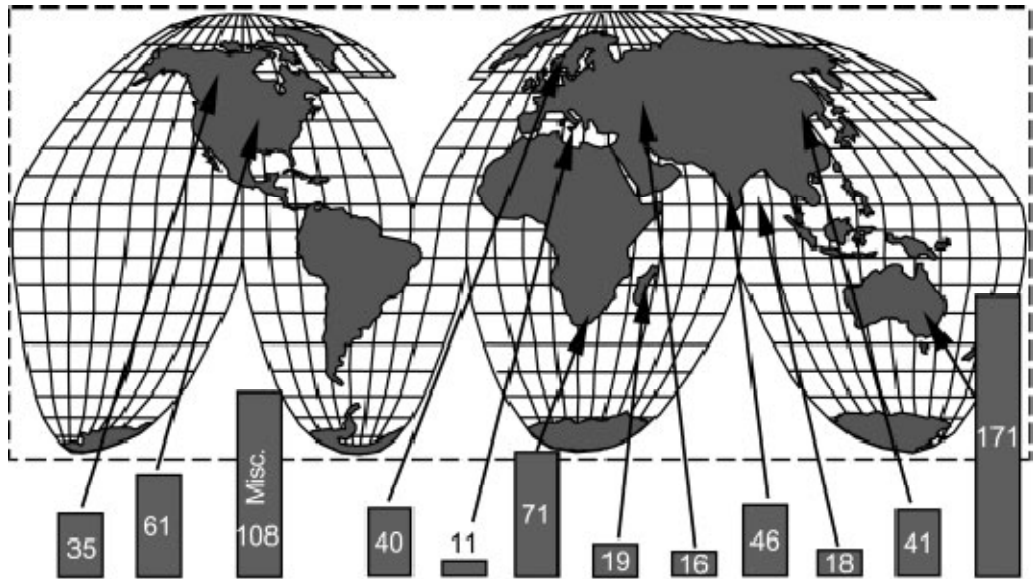
Figure 1-2: Distribution of global titanium oxide deposits (in billions of metric tons, 1999) [7].

1.2.3 Development of Titanium Metal Refinement Process

For almost 150 years after the discovery the element titanium attempts to isolate the metal from the titanium ore resulted in only small quantities of a brittle titanium metal. Kroll's work from 1937-1940 changed this as he developed a commercially attractive refining process that gave pure titanium metal through the reduction of titanium tetrachloride ($TiCl_3$) with magnesium in an inert gas atmosphere. The titanium metal formed as a result of this process is called titanium sponge as it has a porous and spongy appearance as shown in Figure 1-3 [6].

Figure 1-3: Vacuum-distilled titanium sponge [18].

Titanium sponge is the base material for production of all titanium-based products as well as for alloying additions to titanium-stabilised special steels [7]. The Kroll's process is still the dominant process to produce titanium today and has remained essentially unchanged since its initial development [6].

1.2.4 Titanium Processing

The production of titanium is a three-step process:

1. The first step is the manufacture of titanium sponge using the previously described Krolls process [19].

2. The titanium sponge is then crushed into grainy powder and mixed with any required alloying metals, such as aluminium or molybdenum, and melted in a vacuum arc reduction furnace to produce titanium ingots [19].

3. These ingots from the first melt are then used as consumable electrodes in a second melt. This process is called double consumable electrode vacuum melting. For very pure and clean titanium with very homogenous structures, an additional third melt may be carried out [19].

Once cast ingots have been produced they can be processed into a range of products for industry including raw forgings, slabs, billets and plates. As titanium microstructures are sensitive to thermal history, various heat treatments may be performed on the on the titanium products to achieve homogeneous microstructures with desirable mechanical properties. A general overview of the titanium production process is shown in Figure 1-4.
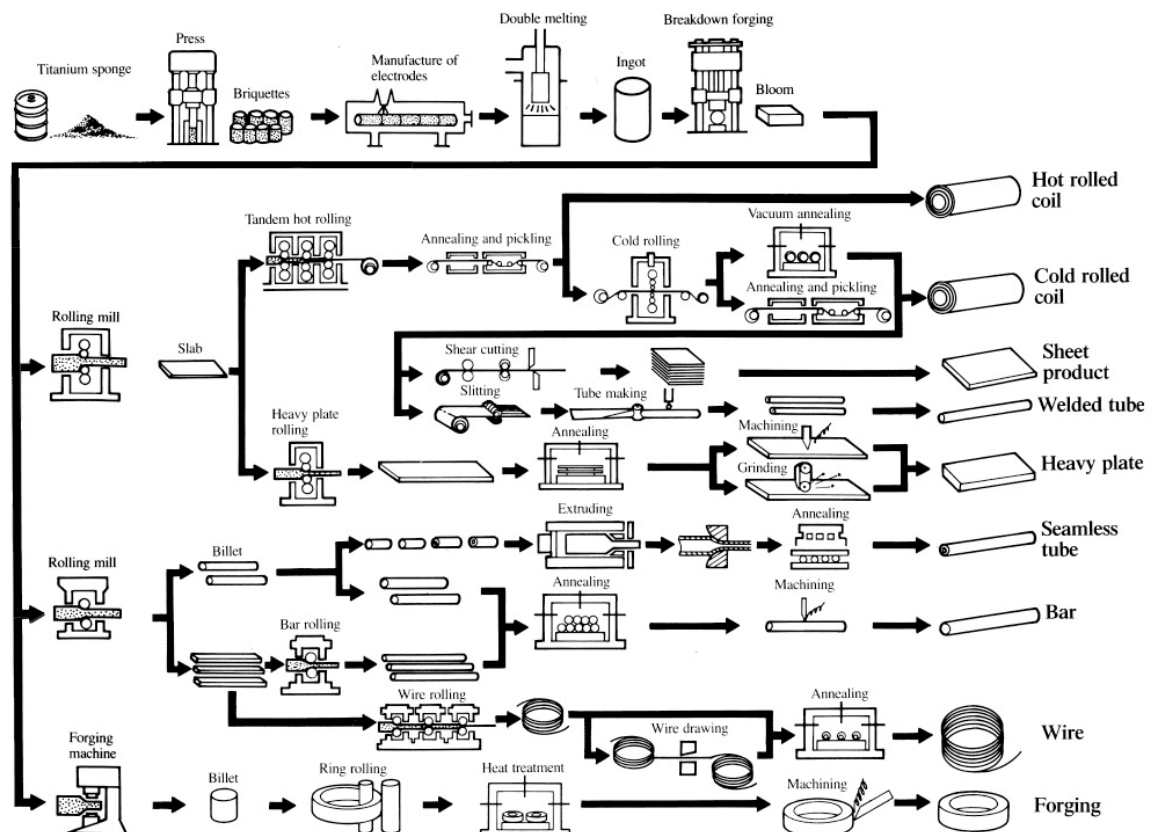
Figure 1-4: Overview of the titanium production cycle for ingot and mill products [20].

Titanium alloys tend to be more difficult to process compared to other common engineering materials such as aluminium and steels, as they have higher flow stress and lower ductility [21].

1.2.5   Fusion Welding of Titanium

Titanium's high material production cost has been a driving force behind efforts to decrease machining scrap for titanium parts. The aerospace industry refers to the ratio of starting material to that of the final part as the buy-to-fly ratio [22]. Welding components like that shown in Figure 1-5, offers a way to reduce the up to 95% of scrap that can come from forging and machining fabrication methods [2, 16].
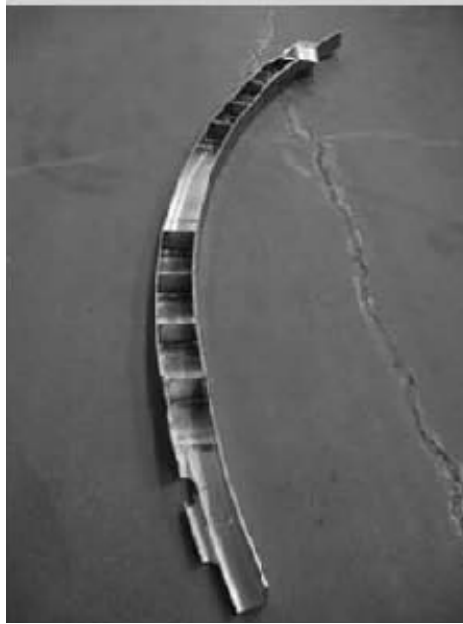
Figure 1-5: Welded component with buy-to-fly ratio of 3:1, originally machined from a plate with a buy-to-fly ratio of 30:1 [22].

Titanium is a unique material, which requires special attention especially in welding [9, 14]. The welding technology of titanium is complicated due to the fact that from temperatures above $350°C$, and particularly in the molten stage, titanium is very reactive towards atmospheric gases such as oxygen, nitrogen, carbon or hydrogen causing severe embrittlement [3, 11, 23, 24]. It is for this reasons that titanium welding requires an inert environment when it is welded, either through a vacuum or inert gas. The HAZ of titanium welds may be partially or completely transformed to β phase during the heating cycle. The room temperature microstructure of a titanium weldment and HAZ is directly influenced by the heat input, cooling rate and welding process used, these affect the size and shape of the prior β grains and the phase transformations that take place during subsequent cooling [25].

Some fusion welding methods for titanium can be performed autogenously thus requiring no filler metal. The composition of theses weldments will essentially be the same as the initial base material. When filler metals are required, the filler metal is usually matched to the same titanium grade that is to be joined. If increased ductility is

wanted in a weld of unalloyed titanium, a titanium filler metal with less oxygen, nitrogen, carbon or hydrogen may be used. Unalloyed filler metal can also be used with Ti-5Al-2.5Sn and Ti6Al4V for improved joint ductility. The unalloyed filler dilutes the concentration of β stabilisers and decreases the β retained during cooling [20, 26].

1.3 Fusion Welding of Similar and Dissimilar Metals or Alloys

Up until the end of the 19th century, sections of metal were fused through a process of heating and hammering called forge welding. Today a variety of different welding processes are available, and are used in various fabrication processes for joining materials of a wide range of compositions, part shapes and sizes [27]. An incredibly wide range of items and structures can only be made through the application of one or several welds [28].

In recent years, there has been renewed interest in moving the fabrication of aerospace components from conventional manufacturing processes, using machining, forgings and castings or mechanically fastening, to components manufactured using welded joints [5]. Complex parts generated by machining, from a solid billet to the final shape, can have as much as 95% of the original material wasted as scrap [5, 28]. The machining costs associated with the removal of a large proportion of the material can make up as much as 40% of the total costs of a final part [23]. One approach that has been employed to reduce the machining costs and extensive material usage is to use a welding process to join simple pieces to complex structures [23].

There are three main zones in a fusion weld, (i) the base metal (BM) which consists of the original substrate microstructure, (ii) the fusion zone (FZ) where the substrate is fully melted and resolidified and (iii) the heat affected zone (HAZ) located between the fusion zone and the base metal where the original substrate microstructure is changed due to the heat of the welding process but is not melted [4].
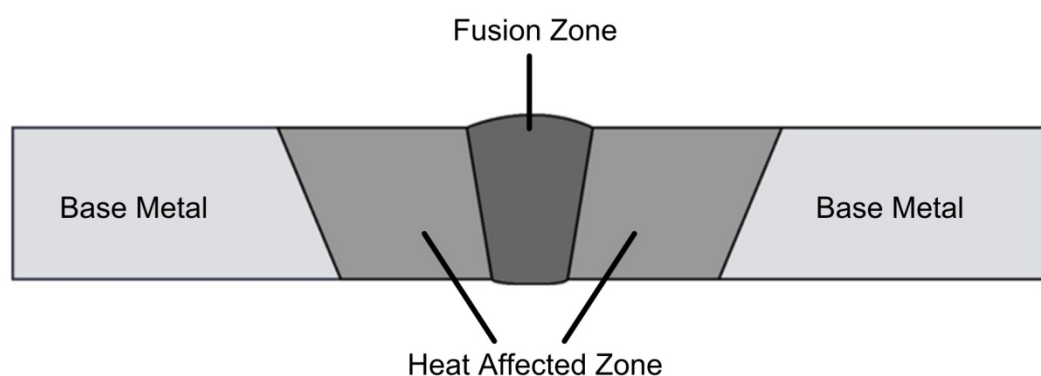
Figure 1-6: Weld cross section.

Welds are often made between dissimilar metals or alloys to take advantage of the different material properties for different parts of an assembly. These properties can include strength, ductility or corrosion resistance [29]. Dissimilar welding may allow for material cost savings within a part. Dissimilar welds often occur between various types of mild steels, tool steels and stainless steels used in construction industries or tool

manufacture [24]. An example of this is a composite bandsaw blade where high speed steel teeth are joined to a spring steel belt [30]. One of the challenges associated with the welding of dissimilar materials is the potential formation of unwanted inter-metallic compounds or unwanted microstructural phase formation in the fusion zone. Differences in chemical compositions and thermal expansion coefficients of dissimilar substrates can result in different residual stresses across the different regions of the weldment as well as the migration of interstitial elements from one substrate to the other [8].

1.4   The Aim of the Research

The aim of the research was to identify the properties and microstructure of electron beam welded (EBW) similar and dissimilar titanium alloys with a particular focus on commercially pure titanium (CP Ti), α+β alloy Ti6Al4V (Ti64) and β alloy Ti5Al5V5Mo3Cr (Ti5553).

2.0 Literature Review

2.1 Titanium Alloys

2.1.1 Alloy Structures of Titanium and the Effects of Interstitial Elements

Pure titanium exhibits an allotropic phase change at 882˚C similar to that of Iron at 912˚C. Below 882˚C pure titanium has a Hexagonally Close-Packed (HCP) α phase crystal structure (Figure 2-1a). Above 882˚C pure titanium has a Body-Centred Cubic (BCC) β phase crystal structure (Figure 2-1b).
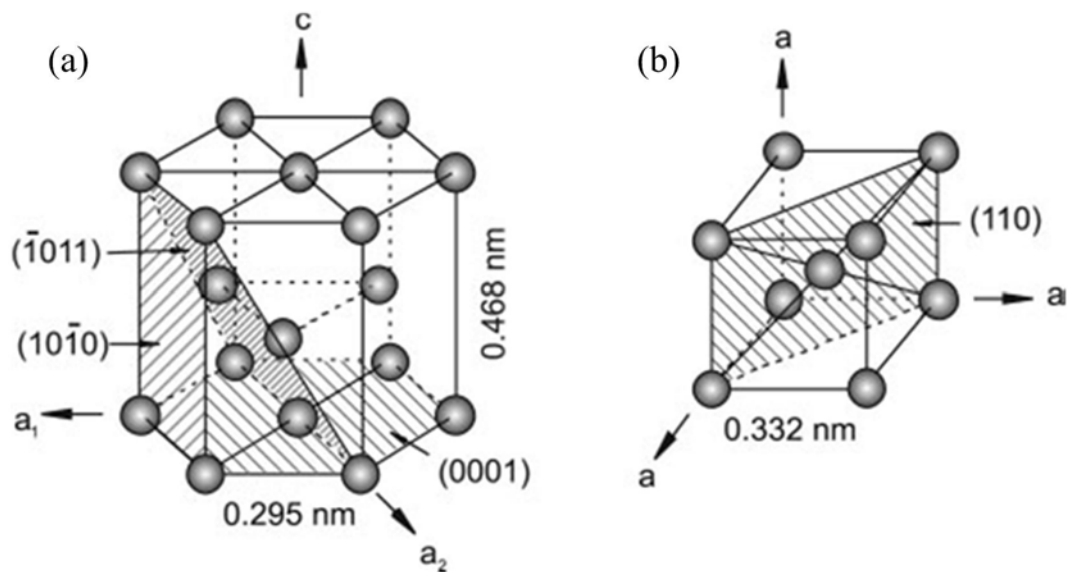
Figure 2-1: Crystal structure of a) hcp α and b) bcc β phase [7].

The β transus is defined as the lowest equilibrium temperature above which the material is 100% β [31]. The cubic β structure is found only at high temperatures, unless the titanium is alloyed with other elements which allow the cubic structure to exist at lower temperatures [20]. The exact transform temperature of titanium alloys is strongly influenced by the different alloying elements and their concentrations. The effect caused by alloying elements in titanium can be classified into four types as shown in Figure 2-2. The α-stabilising elements (Figure 2-2a) increase the α phase field to higher temperatures raising the β transus temperature. Both β isomorphous elements (Figure 2-2b) and β eutectoid elements (Figure 2-2c) move the β transus to lower temperatures, though β eutectoid elements can also lead to the formation of inter-metallic compounds. The neutral (Figure 2-2d) elements have little or no affect on the β-transus temperature [6, 7].
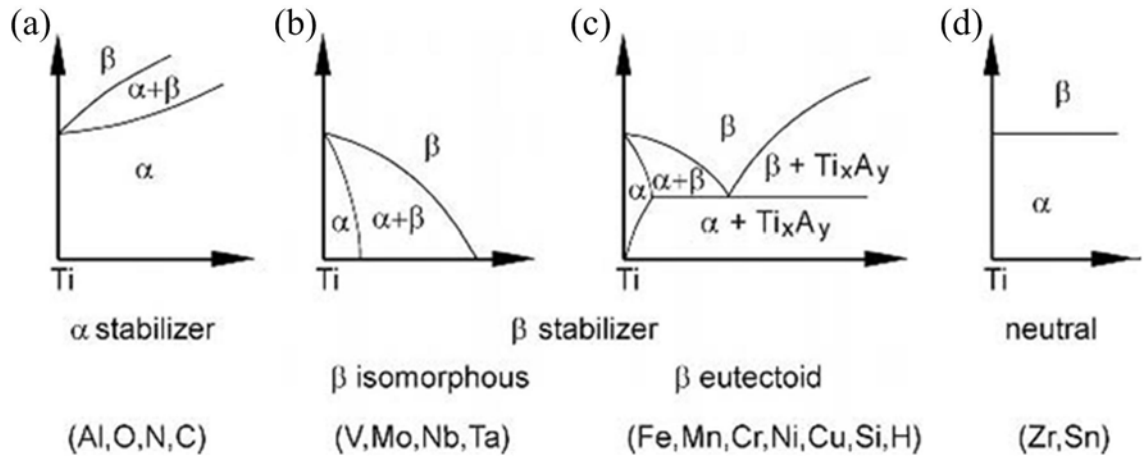
Figure 2-2: Effect of alloying elements on phase diagrams of titanium alloys (schematically) [6].

H. W. Rosenberg attempted to express the effect of α stabilising elements in multi-component titanium alloys as an equivalent aluminium content by developing the following equation [6, 14, 18, 32]:

$$Al_{eq} = Al + 0.33Sn + 0.17Zr + 10 \cdot O$$

(Equation 2.1)

As the value for the aluminium equivalent (Al_{eq}) increases through the addition of α stabilising elements to pure titanium, the value for the β transus temperature increases. The Al_{eq} value can indicate the capacity of the alloy to obtain a given hardness [16].

E. K. Molchanova later expressed a rule for describing the effect of β stabilising elements in multi-component titanium alloys. He developed it in terms of an equivalent of molybdenum content by developing the following equation [6, 14, 18, 32].

$$Mo_{eq} = Mo + 0.67V + 0.28Nb + 0.2Ta + 0.4W + 2.5Fe + 1.25Cr + 1.7Mn + 1.25Ni + 1.7Co$$

(Equation 2.2)

Increases in the value of the molybdenum equivalent (Mo_{eq}) lead to more stable β alloys by bringing down the β transus temperature. The Mo_{eq} value can indicate the capacity to obtain an ultimate tensile strength (UTS) and hardness in the aged condition [16].

Titanium alloys are traditionally classified into α alloys, α+β alloys, and β alloys based on their position in a pseudo-binary β isomorphous phase diagram [6, 19]. The position of a particular alloy is governed by the value of the Mo_{eq}. An example of a β isomorphous phase diagram with the relative positions of some common alloys is shown in Figure 2-3.
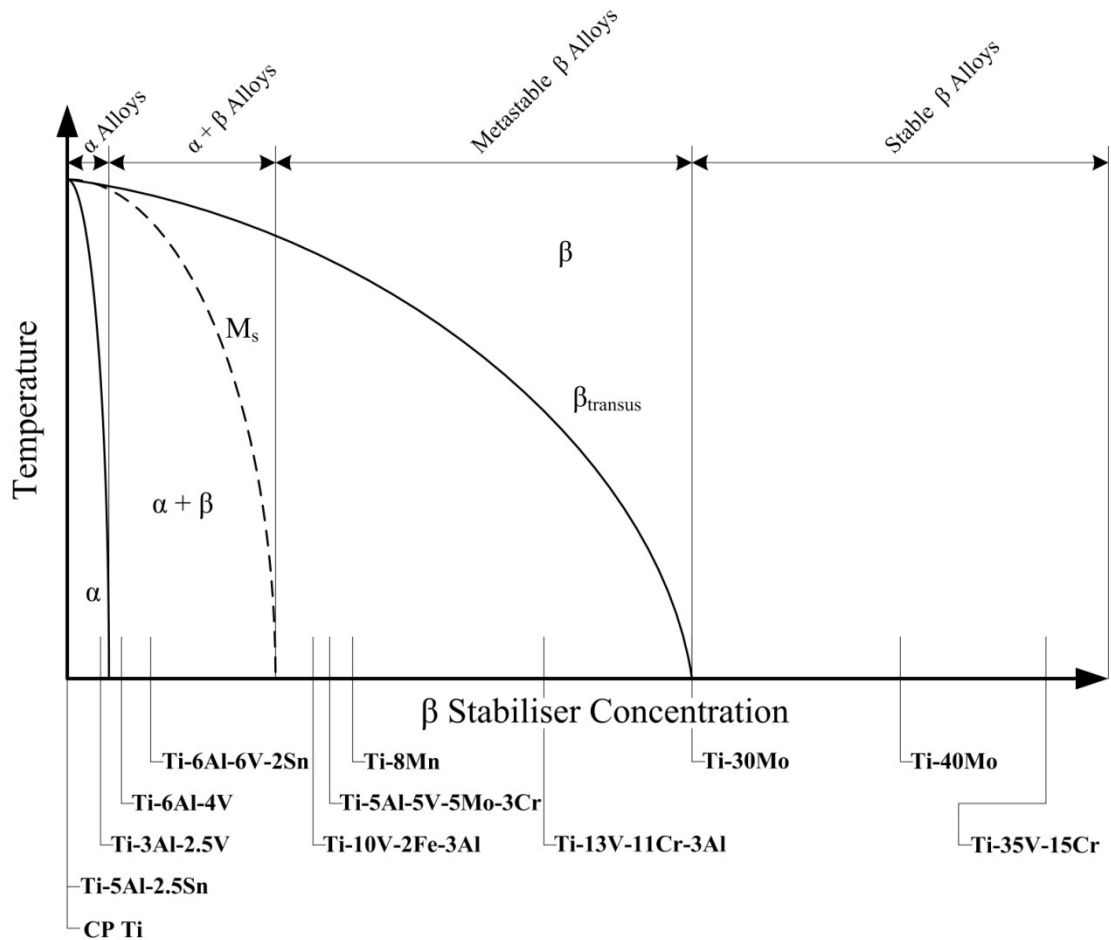
Figure 2-3: Titanium alloy Mo_{eq} mapped onto a β isomorphous phase diagram [6, 7, 33].

Various different phases can occur in titanium alloys depending on chemical composition and thermal history of the sample. Some of the typical phases that can be found are listed below:

α   -   HCP titanium phase

β   -   BCC titanium phase

ω   -   Trigonal or hexagonal (not HCP) crystallographic phase

β'   -   Second bcc phase exhibited as a result of a miscibility gap in solubility of molybdenum (Mo) in titanium.

$α_2$ -   Hexagonal ordered Ti_3Al intermetallic phase

γ   -   FCC TiAl intermetallic phase

α'   -   Hexagonal martensite phase

α"   -   Orthorhombic martensite phase

Oxygen and nitrogen take up interstitial positions in the titanium crystal matrix. As the amounts of oxygen and nitrogen in the alloy increase, the ultimate tensile strength of the alloys, especially in the α alloys, increases. At the same time the toughness of the alloy decreases until the material eventually becomes quite brittle. This trade off and variation in material properties as a result of oxygen and nitrogen content shows the care that must be taken to prevent contamination of the titanium metal during production and processing since titanium is highly reactive with oxygen. This interstitial effect is exploited to produce grades of titanium with higher allowable oxygen and nitrogen contents which have higher tensile strengths and decreased ductility [20].

Hydrogen in solution in titanium has little affect on mechanical properties. The problem hydrogen causes in titanium is the formation of hydrides. Hydrides form after hydrogen diffuses into the material as a result of exposure to either gaseous or cathodic hydrogen. Precipitation of the hydride results in a loss of ductility (embrittlement) and/or a reduction in the stress intensity threshold for crack propagation [20].

2.1.2 Commercially Pure Titanium (CP Ti) and Titanium α Alloy

Very high purity titanium, with a chemical purity of at least 99.9%, is not used widely as a commercial commodity. The high cost and difficulty associated with its production led to the development of commercially pure grades where the titanium content is less than 99.55%. These commercially pure grades have the same general mechanical properties as very high purity titanium [20].

Commercially pure titanium alloys are classified as α phase titanium alloys with β transus temperatures higher than that of pure titanium which is 882°C. The composition and β transus temperature for commercially pure titanium ASTM grade 1–4 can be seen in Table 2-1.

All α titanium alloys are based on the low temperature, hexagonal close packed allotropic form of titanium (Figure 2-1a). α alloys can contain α phase stabilising substitutional alloying elements like Al or Sn or interstitial elements like oxygen, carbon, or nitrogen that are soluble in α phase. Some of these alloys also contain very small additions of limited α solubility elements such as Fe, V, and Mo which are usually associated with α+β alloys or β alloys [6].

Some of the common commercially pure titanium and α alloys are shown with their mechanical properties and their β transus temperatures in Table 2-1.

Table 2-1: Commercially pure titanium and α alloys with their mechanical properties and β transus temperature [6, 20].

Common Name	Alloy Composition (wt %)	σ_{UTS} (MPa)	$\sigma_{y0.2}$ (MPa)	T_{β} (°C)
Pure Titanium	-	-	-	882
CP Ti Grade 1	0.2 Fe, 0.18 O	240	170	890
CP Ti Grade 2	0.3 Fe, 0.25 O	340	275	915
CP Ti Grade 3	0.3 Fe, 0.35 O	450	380	920
CP Ti Grade 4	0.5 Fe, 0.40 O	550	480	950
Grade 7 Ti	0.2 Pd	340	275	915
Grade 12 Ti	0.3 Mo, 0.8 Ni	480	380	880
Ti-3Al-2.5V	3.0 Al, 2.5 V	620	520	935
Ti-5Al-2.5Sn	5.0 Al, 2.5 Sn	790	760	1040

Aluminium an α stabilising element is the most widely used alloying element in titanium alloys. Aluminium is the only common metal that has large solubilities in both the α and β phases while also raising the beta transus temperature [34]. The binary Ti-Al phase diagram (Figure 2-4) shows that with increasing aluminium content the intermetallic phases Ti_3Al (α_2) or TiAl (γ) will be formed. The aluminium content in most titanium alloys is limited to about 6%, to avoid any appreciable amount of intermetallic phases forming [6].
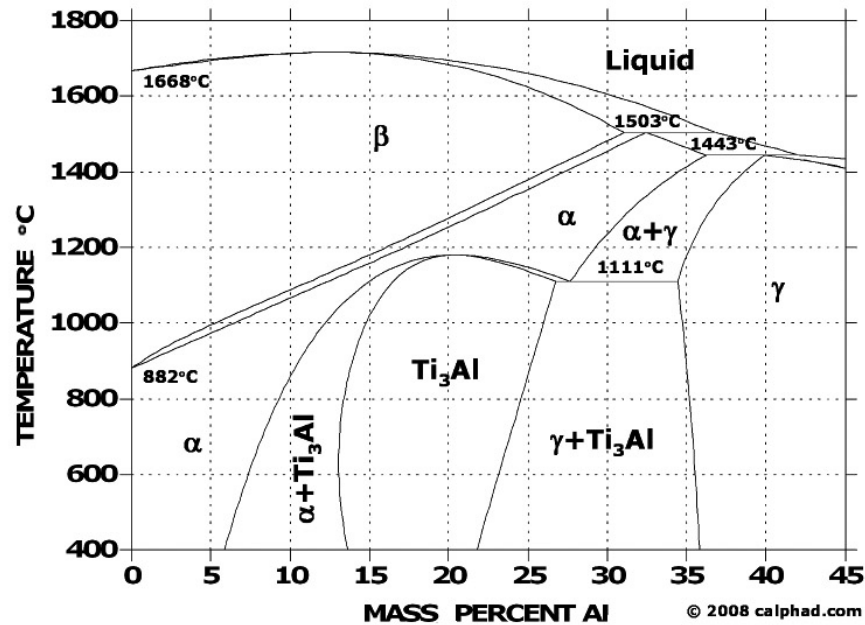
Figure 2-4: Titanium-aluminium binary system phase diagram [34].

As commercially pure titanium is a single phase alloy as 100% of the microstructure at room temperature is α phase, the microstructure is governed by the type of annealing process that has be undertaken and whether the alloy has been cold worked [20]. The cooling rate of the commercially pure alloy from above the β transus of the alloy influence the final microstructure due to the effect it has on the β to α transformation, which varies the final α grain size and shape [20].

Commercially pure titanium is widely used in the chemical and processing industries, where resistance to corrosion and deformability are major concerns [17]. The HCP crystal structure of commercially pure titanium is favourable in creep critical applications due to its level of diffusivity [35]. Commercially pure titanium is also used in medical implant applications due to its biocompatibility.

Comparative to other titanium alloys, α-phase alloys are relatively weak in strength. α phase alloys do offer a number of desirable qualities which include corrosion resistance, good weldability, biocompatibility, resistance to creep, being receptive to heat treatment and a relative ease of processing and fabrication [10].

Expected phases to find in commercially pure and α titanium alloys at room temperature are predominately α phase, with the potential for massive α' phase martensite to form in pure or low solute alloys and acicular α' phase martensite in higher solute alloys when samples have been rapidly cooled from above the β transus. No β phase is expected to be retained in these alloys [35].

Annealing of commercially pure titanium can be performed at temperatures both above and below the β transus temperature. Table 2-2 demonstrates the effect thermal history can have on the material properties of commercially pure titanium. The three conditions in Table 2-2 correspond to the three microstructures shown in Figure 2-5.

Table 2-2: Properties of commercially pure titanium grade 1 after annealing in the α region or β region and cooling to ambient temperatures [20].

Figure 2-5	Anneal Temp, 1 hour (°C)	Type of Anneal	Cooling from Anneal	$\sigma_{y0.2}$ (MPa)	σ_{UTS} (MPa)
(a)	800	α	water quenched	124	248
(b)	1000	β	water quenched	228	290
(c)	1000	β	furnace cooled	165	262
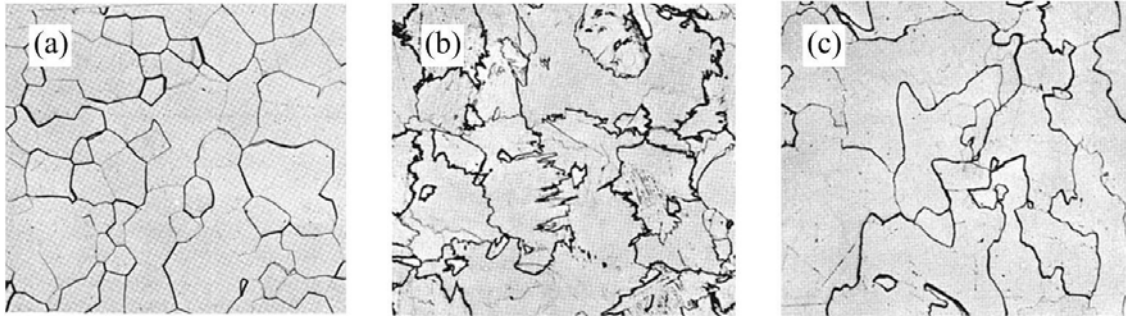
Figure 2-5: Microstructure of CP Ti under different annealing conditions. a) 800 °C, water quench, b) 1000 °C, water quench, c) 1000 °C, furnace cooled. (All 100× optical micrographs) [20].

Equiaxed microstructure in commercially pure titanium can be formed as a result of α region annealing at 800 °C and it is shown in Figure 2-5a. The equiaxed microstructure is weaker than that of both the β annealed microstructures shown in Figure 2-5b and Figure 2-5c. The microstructure that formed as a result of quenching in Figure 2-5b has rough edges to the grains but has the highest strength of the three microstructures shown in Figure 2-5 [20].

The effects of interstitial elements on the β to α transition after β annealing of commercially pure titanium is demonstrated in Figure 2-6. The microstructure of Figure 2-6a (relatively pure titanium) has little visible evidence of any Widmanstätten structure, where as both Figure 2-6b (Ti 0.3wt% oxygen) and the Figure 2-6c (Ti 0.3wt% nitrogen) show the distinctive transformed β cross hatched Widmanstätten structure. Though nitrogen levels in commercially pure titanium grades 1-4 are kept well below that shown in Figure 2-6c, oxygen levels of grades 2-4 are all close to or greater than the Ti 0.3wt% oxygen shown in Figure 2-6b.
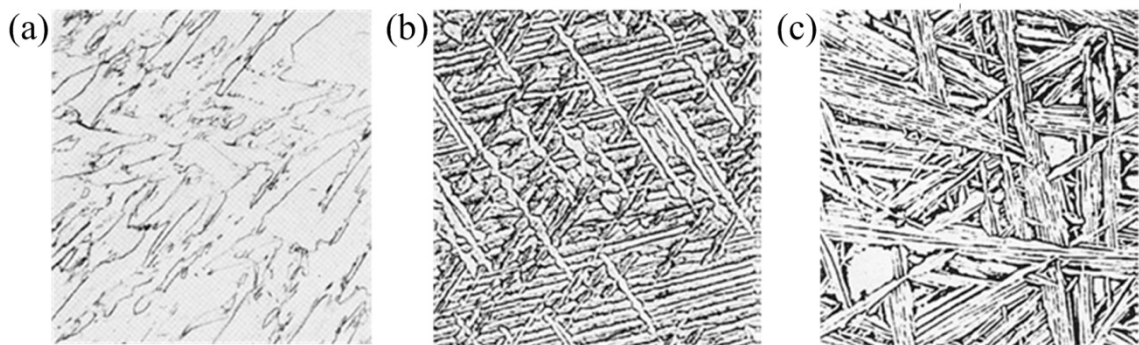
Figure 2-6: Microstructural variation in commercially pure titanium as a result of interstitial oxygen and nitrogen. a) Relatively pure, b) Ti 0.3wt% oxygen, c) Ti 0.3wt% nitrogen. (All 150× optical micrographs) [20].

2.1.3   α+β Alloy Titanium

When both α and β stabilising elements are added to titanium, both α phase and β phase structures may be retained in the alloy at room temperature. Alloys in α+β systems must contain one or more α stabiliser, the most common of which is aluminium, and one or more β stabiliser like vanadium or molybdenum. Just like α alloys, α+β alloys are fully transformed to β when they are heated above the β transus. Unlike α alloys when the α+β alloys cool to room temperature they retain significant proportions of untransformed β phase [20].

Some of the common α+β alloys and their β transus temperatures are given in Table 2-3.

Table 2-3: α+β Alloys with their β transus temperature [6].

Common Name	Alloy Composition (wt %)	T_β (°C)
Ti-811	8.0 Al, 1.0 V, 1.0 Mo	1040
IMI 685	6.0 Al, 5.0 Zr, 0.5 Mo, 0.25 Si	1020
IMI 834	5.8 Al, 4.0 Sn, 3.5 Zr, 0.5 Mo, 0.7 Nb, 0.35 Si, 0.06 C	1045
Ti-6242	6.0 Al, 2.0 Sn, 4.0 Zr, 2.0 Mo, 0.1 Si	995
Ti-64	6.0 Al, 4.0 V, 0.20 O	995
Ti-64 ELI	6.0 Al, 4.0 V, 0.13 O	975
Ti-662	6.0 A, 6.0 V, 2.0 Sn	945
IMI 550	4.0 Al, 2.0 Sn, 4.0 Mo, 0.5 Si	975

Expected phases to find in α+β titanium can range significantly depending on the thermo-mechanical pathway it has been subjected to. Some of both α and β phases are expected to be present but α', α'', α_2 and ω may also be present in various proportions.

α+β alloys have three distinctly different types of microstructures that can be obtained as a result of changing the thermo-mechanical processing route to reach the final microstructure. These three microstructure types are, (i) fully lamellar structures as shown in Figure 2-7a, (ii) bi-modal or duplex microstructures shown in Figure 2-7b, and (iii) fully equiaxed structures which are shown in Figure 2-7c. Bimodal structures contain aspects of both lamellar and equiaxed structures [6]. As a result of the basic material properties and the range of microstructures that can be formed through heat treatment, the α+β alloys offer a range of excellent ductility and strength combinations when proper heat treatment is used [10].
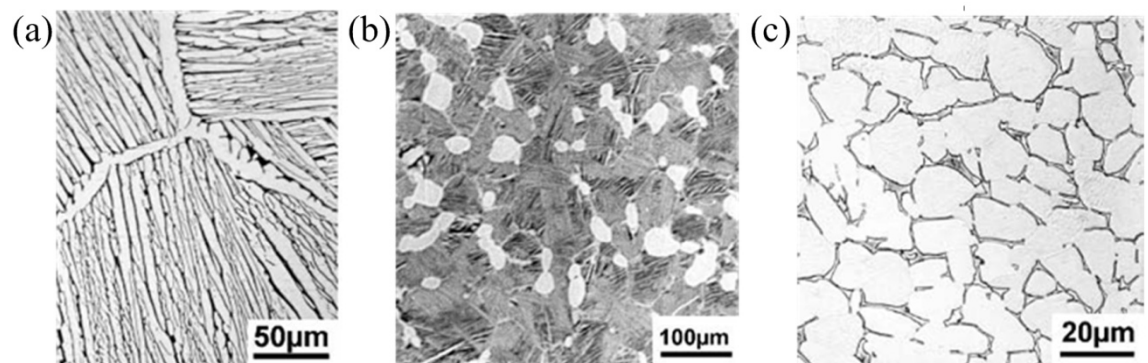
Figure 2-7: a) Laminar Ti-6242, b) bi-modal IMI 834 alloy, c) fully equiaxed Ti6242 [6].

Lamellar microstructures (Figure 2-7a) can be obtained fairly easily through a β phase field annealing treatment. For this reason lamellar microstructure is also referred to as β annealed structure [6]. Figure 2-8 shows how the lamellar microstructure forms as it slowly cools from temperatures above the β transus.
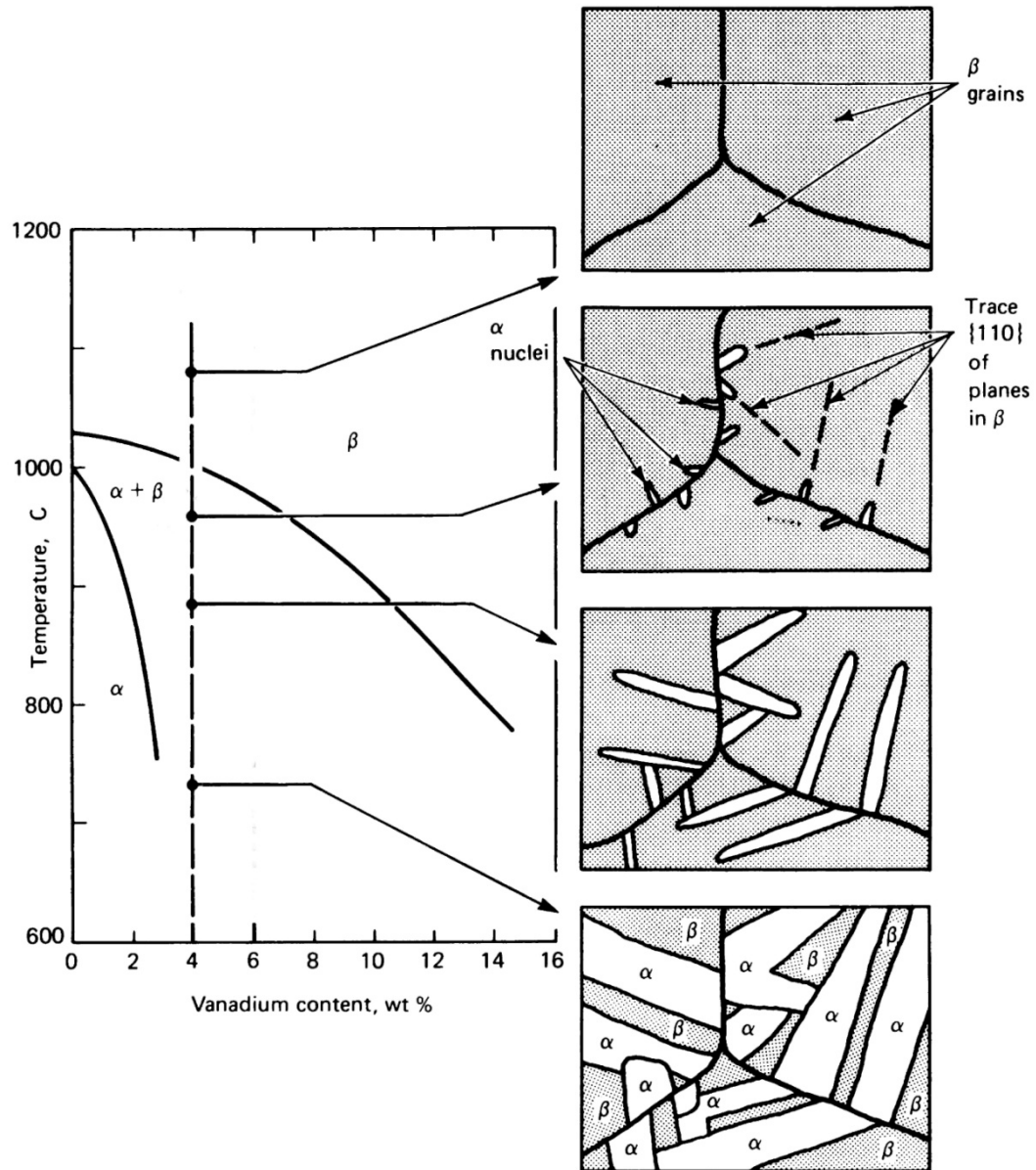
Figure 2-8: Schematic of the microstructures achieved at various intermediate temperatures by slowly cooling from above the β transus showing the development of a Widmanstätten structure in an α+β alloy (Ti6Al4V) [20].

If the α+β titanium microstructure is within critical parameters after β field homogenization is performed, a bimodal microstructure (Figure 2-7b) can be formed through controlled α+β field deformation, recrystallisation and annealing [35]. These steps are shown schematically in Figure 2-9.
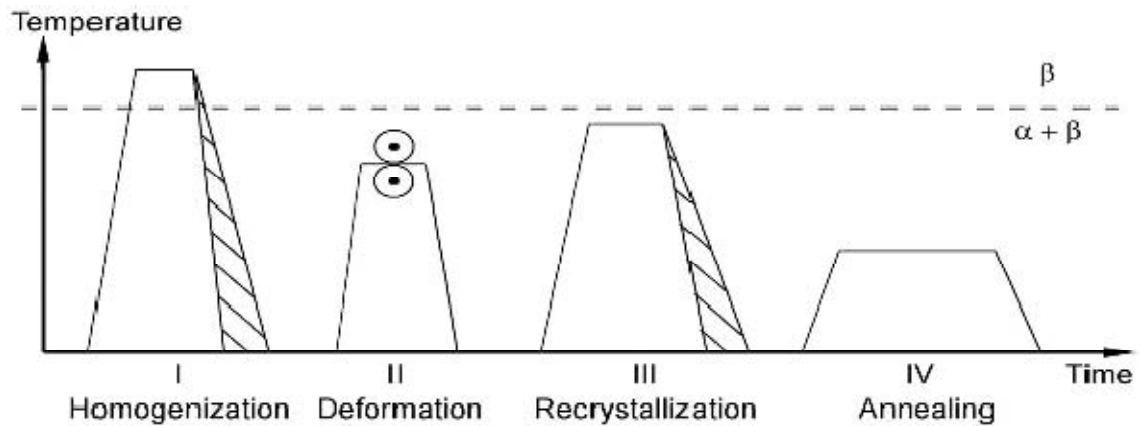
Figure 2-9: Processing route for bi-modal microstructures of α+β titanium alloys (schematically) [6].

The other pathway to the formation of the bimodal microstructure (Figure 2-7b) occurs when thermo mechanical working of an α+β titanium alloy leaves sufficient retained strain energy and is subsequently heat treated below the β transus in the α+β region. A portion of α re-crystallises as equiaxed α and the remaining β undergoes transformation to acicular/lath α with retained β in between [35].

If the cooling rate from the β phase annealing temperature is sufficiently low, only the α phase grains grow during the cooling process. The resulting microstructure is a fully equiaxed structure of the α grains (Figure 2-7c) with the equilibrium volume fraction of β phase separated to the triple-points between the grains [6].

The effect of the range of microstructural structures that can occur on cooling from prior β grains means that welds can have significant effects on mechanical properties in α+β titanium alloys, both in the fusion zones and the heat affected zones [14].

2.1.4 Ti6Al4V (Ti64) Alloy

Ti6Al4V (Ti64) is an α+β type alloy and is the most commonly used titanium alloy, making up over 50% of the market in the USA titanium market in 1999 and made up 45% of the total weight of all titanium alloys shipped for the last half of the twentieth century [6, 11, 16, 20].

There are currently no other titanium alloys that look to replace Ti6Al4V as the dominant alloy of choice. Ti6Al4V alloy exhibits good basic material properties such as strength, toughness and excellent corrosion resistance with the processing advantages of good workability and shop fabricability. Ti6Al4V is widely commercially available, and has been used in industry for so long, there is a great deal of production experience that has led to its reliable and economic usage [20, 36].

As a result of its dominance in the titanium market, wrought Ti6Al4V has become the standard titanium alloy against which other titanium alloys are compared when a titanium alloy is selected for a specific application. Ti6Al4V also is the standard alloy selected for castings that must exhibit superior strength characteristics. With a proven track record for more than fifty years, Ti6Al4V looks to continue to be the most used titanium alloy for many years to come in the future [20, 36].

The alloy strength, biocompatibility and commercial availability have been key aspects to the rise in the use of Ti6Al4V as a medically implantable material. Simple manufacturing methods for implants like casting or machining from a billet, may be used for application like orthopaedic prostheses. Welding makes it possible to produce many kinds of complex medical products from Ti6Al4V such as pacemakers, defibrillators and insulin pumps [25].

Ti6Al4V has temperature limitations that restricts its use to applications that operate below 400 °C as atmospheric oxygen and hydrogen can cause severe embrittlement above this temperature [20].

Some typical values for Ti6Al4V strength and elongation as a result of different aging processes are shown in Table 2-1.

Table 2-4: Ti6Al4V tensile mechanical properties 25 °C [20].

Heat Treatment	Heat Treatment Cycle	$\sigma_{y0.2}$ (MPa)	σ_{UTS} (MPa)	Elongation (%)
Mill annealed	α+β hot work, anneal at 705˚C for 30min to several hours, air cool	945	1069	10
Duplex annealed	Solution treat at 50–75 °C below the T_β, air cool, age for 2–8 hours at 540–675 °C	917	965	18
Solution treated and aged	Solution treat at 40 °C below the T_β, water quench, age for 2–8 h at 535–675 °C	1103	1151	13

The great variations of microstructures that can be formed from Ti6Al4V alloy through variations in thermal history are demonstrated in Figure 2-10 [20]:

(a) α' + β; prior beta grain boundaries.
(b) Primary α and α' + β.
(c) Primary α and α' + β.
(d) Primary α and metastable β.
(e) Acicular α + β; prior beta grain boundaries.
(f) Primary α and acicular α + β.
(g) Primary α and acicular α + β.
(h) Primary α and β.
(i) Plate-like α + β; prior grain boundaries.
(j) Equiaxed α and intergranular β.
(k) Equiaxed α and intergranular β.
(l) Equiaxed α and intergranular β.
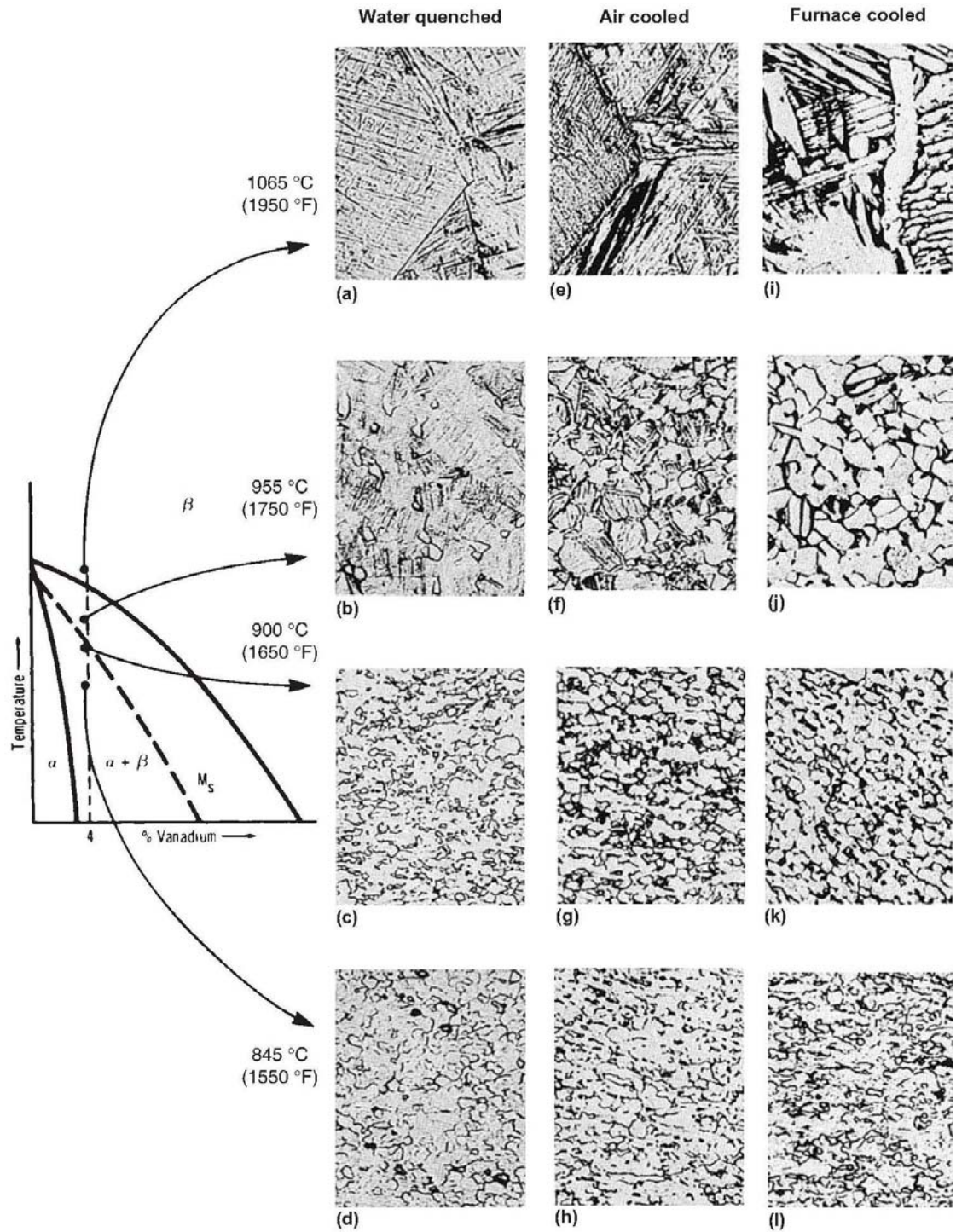
Figure 2-10: Effect of solution temperature and cooling rate on the microstructure of Ti6Al4V (all images at 250x magnification) [20].

21

2.1.5 β Alloy Titanium

A titanium alloy with a Mo_{eq} (see equation 2.2 on page 10) value of above 30 is required for an alloy to be classified as a stable β phase titanium alloy [7]. Metastable β alloys are alloys that contain sufficient β stabilising alloying element to retain the β phase without the formation of martensite when it is quenched from above the β transus to room temperature (see Figure 2-3) [20]. Commercially, metastable β alloys are commonly referred to as β alloys. Metastable β alloys require a minimum Mo_{eq} value of 10 to retain the β phase when quenched to room temperature [32]. The higher the Mo_{eq} value is for an alloy, the higher the volume retention of the β phase should be, for the same cooling conditions.

Metastable β titanium alloys can retain fully β-phase microstructure, have good corrosion resistance and are receptive to forging. These qualities make them candidates to be used in demanding structural applications particularly in the aerospace industry where light weight, impact toughness and high-strength properties are required [10, 37, 38]. Some of the common β alloys and their β transus temperatures are given in Table 2-5.

Table 2-5: β Alloys with their β transus temperature [6].

Common Name	Alloy Composition (wt %)	$T_β$ (°C)
Ti-6246	6.0 Al, 2.0 Sn, 4.0 Zr, 6.0 Mo	940
Ti-17	5.0 Al, 2.0 Sn, 2.0 Zr, 4.0 Mo, 4.0 Cr	890
SP-700	4.5 Al, 3.0 V, 2.0 Mo, 2.0 Fe	900
Beta-CEZ	5.0 Al, 2.0 Sn, 2.0 Cr, 4.0 Mo, 4.0Zr, 1.0 Fe	890
Ti-5-5-5-3*	5.0 Al, 5.0 V, 5.0 Mo, 3.0 Cr*	856*
Ti-10-2-3	10.0 V, 2.0 Fe, 3.0 Al	800
Beta 21S	15.0 Mo, 2.7 Nb, 3.0 Al, 0.2 Si	810
Ti-LCB	4.5 Fe, 6.8 Mo, 1.5 Al	810
Ti-15-3	15.0 V, 3.0 Cr, 3.0 Al, 3.0 Sn	760
Beta C	3.0 Al, 8.0 V, 6.0 Cr, 4.0 Mo, 4.0 Zr	730
B120VCA	13.0 V, 11.0 Cr, 3.0 Al	700
* Ti5553 values from [39]		

Properties of β alloys vary significantly depending on composition and thermo mechanical processing. β alloys have the ability to be aged to adjust the strength and ductility of the alloy, depending on the application a β alloy can either be stronger or more ductile than Ti6Al4V. Many β alloys can be forged more easily and at lower temperatures than alloys like Ti6Al4V. β alloys can offer much better fatigue resistance and impact resistance than Ti6Al4V. β alloys tend to be more difficult to cast and weld.

Metastable β alloys have been chosen for applications like landing gear, thrust links or pylon fittings due to the high strengths, improved fatigue, warm strength and toughness performance they have compared to Ti6Al4V [23, 40, 41].

The mechanical properties of metastable β alloys are largely governed by the morphology, distribution, size and volume fraction of the various precipitates including

α phase precipitates [40, 41]. These precipitates create a high number of interfaces that act as dislocation barriers, increasing the alloy strength [41].

There are two significant metastable phases, ω and β', which are observed in β titanium alloys, these are shown in Figure 2-11 [6].
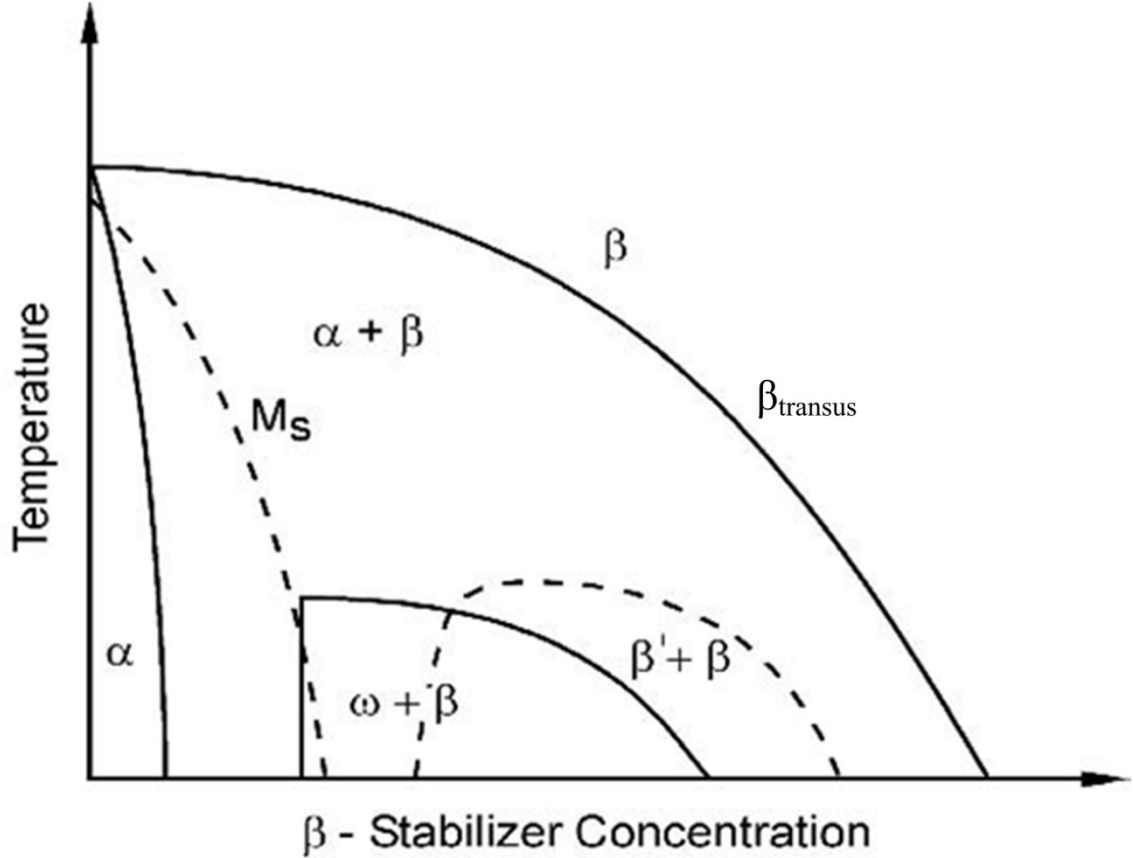
Figure 2-11: Metastable (ω+β) and (β'+β) phase fields in a β isomorphous phase diagram (schematically) [6].

β' phase is a second BCC phase that is formed where a specific concentration of β stabilising element cannot be stably held in the β titanium matrix. This occurs with higher concentrated alloys as a result of a miscibility gap. The two BCC phases β and β' have different β stabilising element concentrations and can also be described as β_{lean} and β_{rich} [6].

The ω phase occurs in lower concentration alloys compared to the β' phase forming alloys as shown in Figure 2-11. There is an intersecting range of concentrations where either ω phase, β' phase or both could form on cooling. From a crystallographic viewpoint, the ω phase has a trigonal symmetry in heavily β stabilised alloys and a hexagonal (not hexagonal close-packed) symmetry in leaner alloys [6, 42].

There are two different forms of ω phase that are conventionally distinguished. They consist of athermal ω phase, which precipitates without diffusion on cooling, and isothermal ω phase, which precipitates from the β phase during low-temperature ageing [40].

The athermal ω phase forms as uniform dispersion of extremely fine particles (size 2-4 nm). Isothermal ω phase occurs as a result of the athermal ω phase growth when it is annealed in the metastable ω+β phase temperature field. Isothermal ω phase has the same crystallographic symmetry as the athermal ω phase it was grown from. Isothermal ω phase is solute lean with respect to the β phase it is formed in [6]. The isothermal ω phase has been reported as having either cuboidal or ellipsoidal morphologies [41].

Excellent mechanical properties may be achieved in metastable β phase titanium alloys through ageing below the β-transus temperature. This will precipitate a fine dispersion of hexagonal α phase particles throughout the β phase matrix [37, 38, 42].

It has been established that the nucleation sites for the α phase within the β phase matrix of β titanium alloys include β grain boundaries, β-ω phase interfaces, β-β' phase interfaces and other matrix defects such as intermetallic particles and dislocations [41, 43].

In metastable β-titanium alloys as a result of the much lower β transus temperature of the material, the α-phase is formed at much lower temperatures and therefore, the transformation occurs much more slowly than the α-phase formation in α+β alloys [37].

Historically due to political divisions that existed between the former Soviet Union Russian States and the USA, Japan and Europe, titanium alloys development was pursued separately. This has led to the independent development of alloy systems. Since the 1970s, β alloy VT22 (Ti5Al5V5Mo1Cr1Fe) has been a widely used titanium alloy in the Russian Aerospace industry for high load components and units [15]. Both Figure 2-12 and Figure 2-13 show Russian aerospace parts that have been made using the VT22 β alloy.
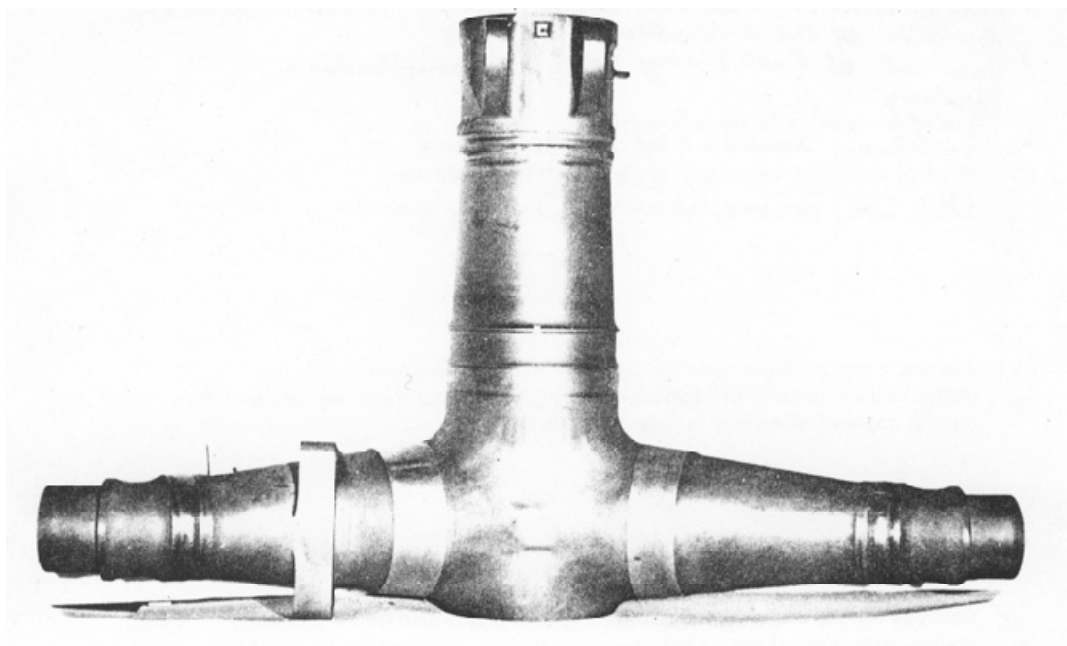
Figure 2-12: Landing gear beam from alloy VT22 for IL76 airliner. Dimensions, 1200×1400 mm [15].

24
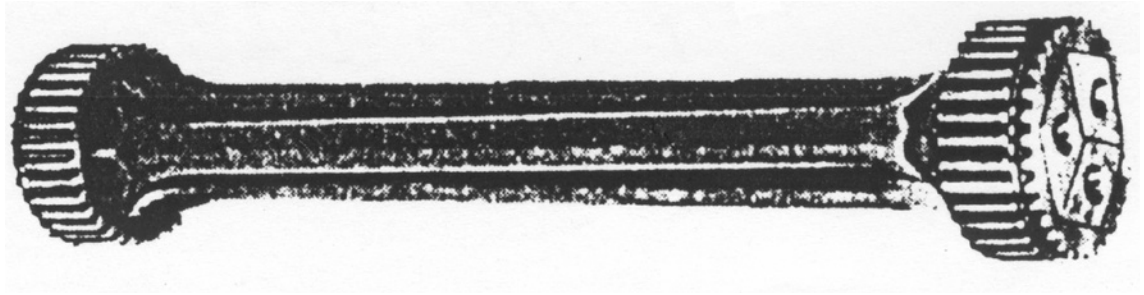
Figure 2-13: VT22 titanium alloy torsion assembly for the Lunokhod moon robot [15].

The most common titanium alloy used in the west for commercial sector landing gears is β alloy Ti10V2Fe3Al. Ti10V2Fe3Al offers a number of advantages for forged parts over the most common alloy Ti6Al4V, such as lower required forging temperatures and pressures which results in the ability to fabricate more complicated shapes at a lower cost [44]. β forging Ti10V2Fe3Al gives high strength with low ductility, but final α+β forging offers increased ductility at the expense of some strength. Ti10V2Fe3Al is somewhat difficult to melt and its mechanical properties decrease with increasing thickness. With the onset of globalisation and dissolution of the former Soviet Union, the formally separated Russian alloy systems are now available in the western countries [45].

2.1.6   Ti5Al5V5Mo3Cr (Ti5553) Alloy

Ti5Al5V5Mo3Cr (Ti5553) is a relatively new metastable β alloy that is a modification of the old Russian alloy VT22 (Ti5Al5V5Mo1Cr1Fe) [6, 16, 41]. Ti5553 compared to Ti10V2Fe3Al has shown less sensitivity to forming variables, offering a larger processing window while giving higher tensile strength capabilities for larger thickness (200mm) [22, 32, 41, 46].

Ti5553 has been specified for commercial use in the landing gear of the new Boeing 787 Dreamliner and is also being looked at as a possible replacement titanium alloy for existing landing gear assemblies in other aircraft [16, 22, 38, 47].

Figure 2-14: Ti5553 landing gear for the Dreamliner [48].

2.1.6.1   Expected Phases to Exist in Ti5553

As Ti5553 is a metastable titanium alloy, it contains enough β stabilising elements to prevent the formation of either α' phase or α'' phase martensite upon quenching from above the β transus temperature. Therefore a β-rich microstructure is obtained though small athermal ω phase precipitates do form during quenching [41, 43, 46]. No α phase should be present as a result of quenching. Annealing at low temperatures will grow the existing athermal ω phase precipitates into larger isothermal ω phase and stable α phase will nucleate from β grain boundaries and ω-β phase interfaces [43]. The α phase precipitates preferentially on β grain boundaries and ω-β phase interfaces due to lattice disorder that occurs in these sites [38].

Annealing at higher temperatures still below the β transus, leads to dissolution of ω phase and continued growth of α phase precipitates [43].

It has been shown that the alloying elements, during low temperature (350˚C) annealing of quenched Ti5553 precipitates have a non-equilibrium composition, nearly identical to that of the β matrix in the nucleating α phase. Further aging at higher temperatures (600˚C) leads to a pronounced partitioning of alloying elements between the α phase and β phase [43]. This means Al, being an α stabiliser, prefers to segregate to the α precipitates, while V, Mo, Cr, and Fe, being β stabilisers, prefer to segregate to the β matrix [49].

2.1.6.2 Mechanical Properties and Microstructures of Ti5553.

The allowable range for Ti5553 element composition as specified by manufacturer Timetal is given in Table 2-6.

Table 2-6: Chemical composition of Ti5553 (wt %) [39].

Element	wt %
Aluminium	4.4 – 5.7
Molybdenum	4.0 – 5.5
Vanadium	4.0 – 5.5
Chromium	2.5 – 3.5
Iron	0.3 – 0.5

The mechanical properties that result from the four aging treatments are listed in Table 2-7. The photomicrographs in Figure 2-15 correspond to the four different aging conditions shown in Table 2-7.

Table 2-7: Mechanical properties and conditions for Ti5553 shown in Figure 2-15 [39].

Figure	Heat Treatment Stages		Tensile properties		
	3 hour Soak (ST), air cooled. (˚C)	8 hour Soak (Age), air cooled. (˚C)	σ_{UTS} (MPa)	$\sigma_{y0.2}$ (MPa)	Elongation (%)
Figure 2-15 (a)	804	610	1294	1218	7
Figure 2-15 (b)	804	660	1163	1100	13
Figure 2-15 (c)	832	610	1332	1218	5
Figure 2-15 (d)	832	660	1189	1104	9

The photomicrographs in Figure 2-15 show microstructures after aging soaks at different temperatures. Bright spots on these photomicrographs indicate areas of α phase in the β matrix. The α phase nucleates and grows as a result of heat treatment and shows significantly more growth when aged for 8 hours at 610˚C than at 660˚C.
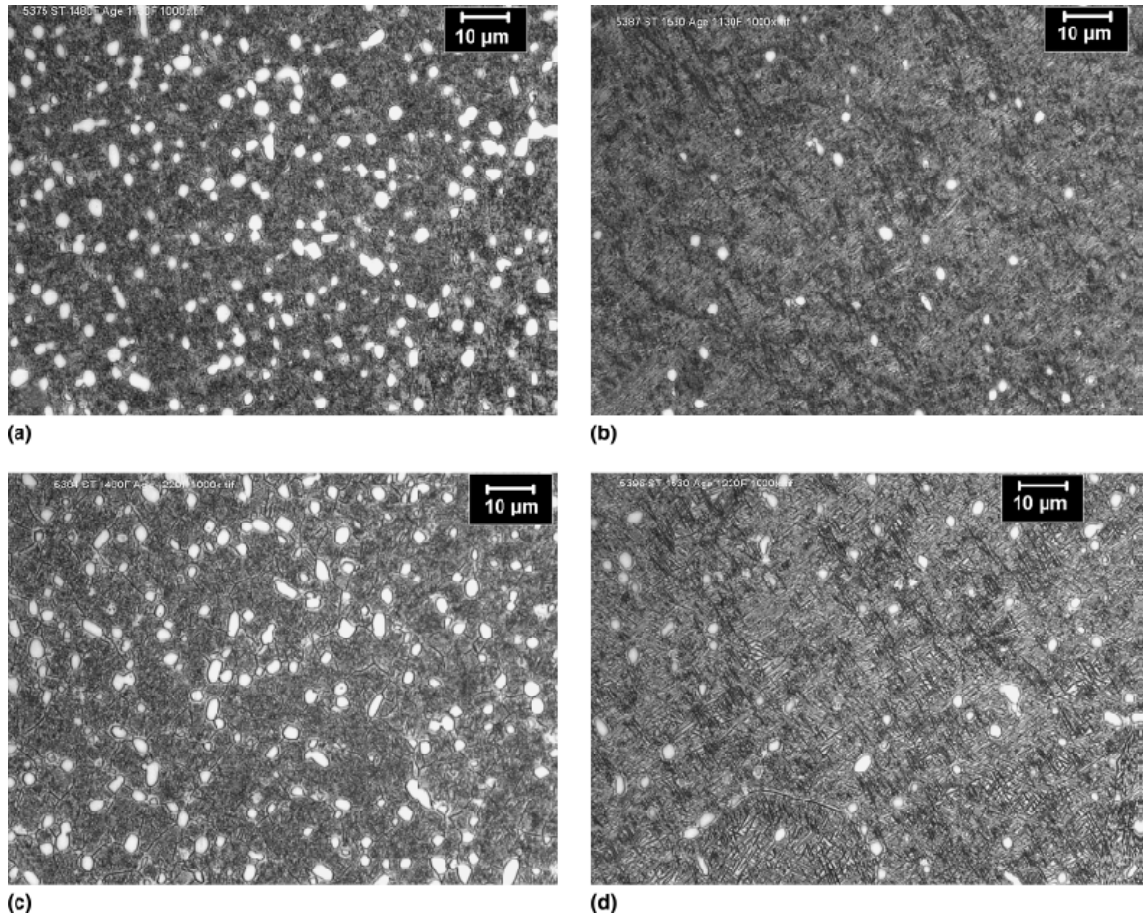
Figure 2-15: Photomicrographs Ti5553 billet in several different STA conditions, a) ST 804˚C, Age 610˚C, b) ST 804˚C, Age 660˚C, c) ST 832˚C, Age 610˚C, d) ST 832˚C, Age 660˚C, [39].

Typical microstructure for Ti5553 alloy after 1 hour aging soaks at various temperatures are shown in Figure 2-16. Figure 2-16a shows sparsely distributed equiaxed α phase. Figure 2-16b shows β grain boundaries completely covered in parallel plates growing towards the centre of the grain. The close up view shown in Figure 2-16c shows the β matrix completely entangled with homogeneously nucleated fine α phase precipitates [50].
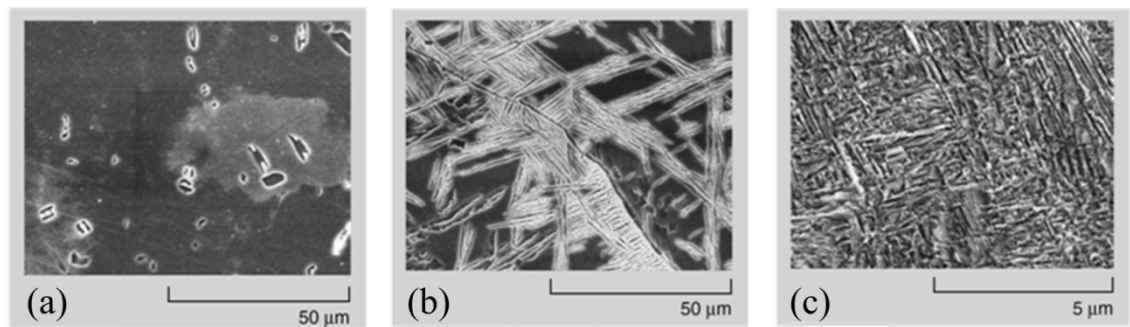
Figure 2-16: Scanning electron micrographs of solution treated and aged Ti-5553 alloy for 1 hour at different aging temperatures: (a) 800°C, (b) 700°C, and (c) 500°C. [50].

2.2   Electron Beam Welding

2.2.1   The Mechanism of Electron Beam Welding

When an electron meets the surface of a solid or a liquid, it penetrates a thin layer with no significant drop in velocity before it encounters resistance from the target material and decreases its velocity. The lower the density of the target material the deeper the electron will penetrate. As the electrons velocity decreases, their kinetic energy is transferred to the target material in the form of heat. The amount of heating and the depth of penetration that is achieved from an electron beam is dependent on the accelerating voltage (which is the initial energy of each electron), the beam current (which is the number of electrons impacting the target surface per unit time), and the density of the target material [2, 4].

At very low power densities the electron beam will cause only heating without any melt of the target occurring (Figure 2-17a). This function has the potential to be used for preheating material before welding or post weld heat treatments. As this method does not require a tightly focused beam, a defocused beam could cover a large area.

At low power densities, caused by either a defocused beam or a low beam current, the electron beam energy is only transferred to areas near the surface of the target material. This forms shallow weld pools and the welding mode is called conduction mode welding (Figure 2-17b).

When high power densities are employed, temperatures well above the sublimation temperature of the target material can be achieved. The vaporisation of some of the target material is the key to deep penetration welds in electron beam welding. The electrons can penetrate many times greater through vapour than in the solid due to the large differences in density. The vapour pressure opens up a hole in the hot zone of the weld pool allowing the beam to penetrate deeper with the potential to pass through the other side of the target material. This type of welding is called keyhole welding (Figure 2-17c) [2, 51].
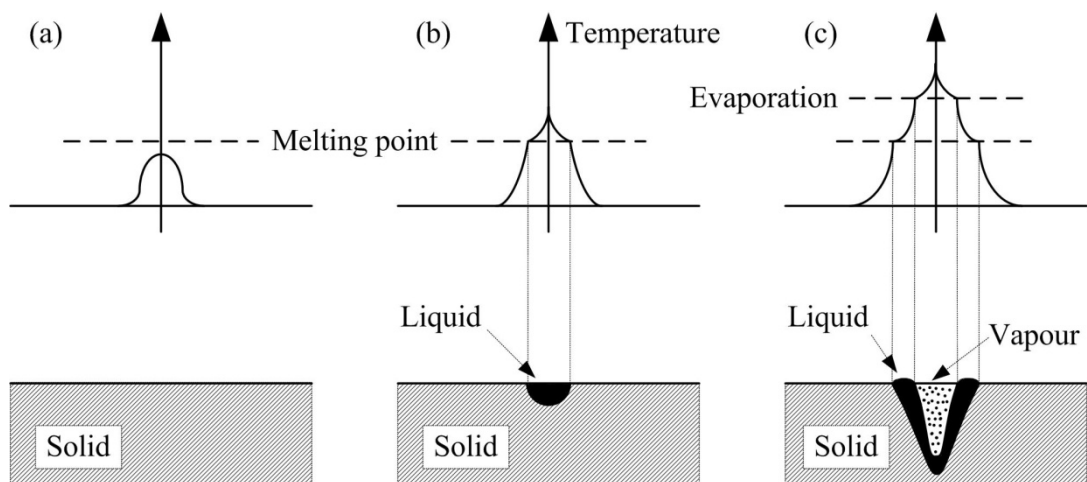
Figure 2-17: Effect of power density on thermal effects of an electron beam (a) heating without melting, (b) melting without deep penetration, (c) deep penetration [2].

The hole opened up by the vapour may collapse due to the surface tension of the weld pool, but if the vapour pressure can stay high enough then the hole can be kept open for as long as there is sufficient power supplied to the material from the electron beam [2]. The instability of the hole in the weld pool, and its collapse can lead to inconsistencies in the root of the weld.

2.2.2 Desirable Features of Heating with an Electron Beam

2.2.2.1 Chemical Purity

Unlike any welding processes where charged ions can lead to chemical impurities from the ionised gas environment used to transfer energy, electron beam welding is performed in a high vacuum environment where the chemically inert electron beam carries the energy to the target material [2].

2.2.2.2 Controlled Guidance to Preselected Areas

As the electron beam cross-section is controlled by electrostatic or magnetic lenses it can be easily deflected or focused to rapidly guide the beams energy to predetermined positions and vary power densities rapidly [2].

2.2.2.3 Wide Range of Powers

The power level can be altered by changing the beam current or the accelerating voltage. The level of variation available allows the same electron beam welding machines to be used over a large range of thicknesses, from over 150mm (Figure 2-18a) to as thin as 0.1mm foils (Figure 2-18b) [2].
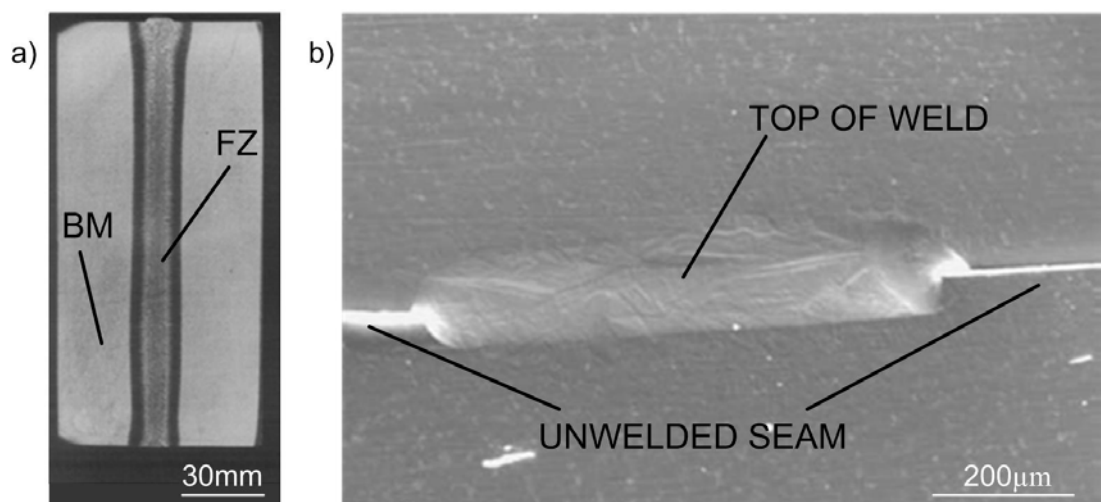
Figure 2-18: EBW of (a) 150mm thick Cr-Mo steel (cross section) [30] and (b) stainless steel foil (top view) [52].

2.2.2.4 Control of Power Density

As power density is a function of area, power and time, it can be varied through control of the power output of the beam through adjustments to the beam current and accelerating voltage, or through manipulation of the beam. The beam can be defocused and spread over a large area or focused to a fine spot for a high density beam. Rapid beam oscillation and beam deflection can be used to decrease the beam density of a fine

focus beam with rapid travel speeds that decrease the time the beam is in one spot. Electron beam welder power densities can range from $0.1 W/mm^2$ to $10^7 W/mm^2$ [2].

2.2.2.5 High Power Efficiency

Nearly all the power input into the electron gun is transferred into heat in the target material. There is some minor loss due to the formation of X rays and secondary electrons, but this loss can be as low as 1% [2].

2.2.3 Undesirable Features of Heating by Electron Beam

2.2.3.1 The Need for a Vacuum

An electron beam cannot be generated outside of a high vacuum environment. Vacuum chambers can take a long time to pump down which has to be factored into manufacturing times. The chamber size may limit the size or shape of the components that can be handled. Operation of low vacuum or no vacuum work chambers offer a solution to reduce or remove the long pump down times, but welds performed in this environment lose some of the benefits working in a vacuum environment can offer. A high vacuum environment is still required for the gun assembly to operate even in the low or no vacuum electron beam welding machines. Materials like wood can be an issue in vacuum chambers, as they can slowly bleed captured gases affecting the vacuum level. This effect may limit what composite items can be electron beam welded eg. a file with a wooden handle could cause problems [2, 36].

2.2.3.2 Unwanted Material Evaporation

Materials with a high vapour pressure near their melting point will evaporate during the fusion process. If these materials are part of an alloy then compositional control can become very complicated and additions may be required to compensate for the evaporation losses [2].

2.2.3.3 High Capital Cost

Compared with traditional welding equipment the high cost for a vacuum plant and high voltage equipment makes for a significant capital outlay when setting up and electron beam welding machine [2, 53].

2.2.3.4 Radiation Hazards

When electrons impact any surface during electron beam welding X-rays are formed. As a result of the X-ray radiation, shielding is required. Regular radiation certification is required for all machines and operators to ensure electron beam welding can be performed safely [2, 53].

2.2.3.5 Magnetic Fields

Electron beams can be distorted or deflected by the presence of magnetic fields. Magnetic materials to be welded and any fixtures must be demagnetised before welding or the beam may not be able to follow the desired path. Magnetic fields can also be formed during the welding of dissimilar materials [2, 53].

2.2.3.6 Rapid Cooling and High Thermal Gradients

Electron beam welding can have high thermal gradients and cooling rates compared to other heating sources. As electron beam welding uses concentrated and efficient heat input with high depth to width ratios, the distance from vaporisation to base metal out of the HAZ can be very small. The localised heat also means that the remaining work piece will act like a heat sink pulling the heat away from the weld area very quickly. Rapid cooling can be an issue for materials like iron or titanium that can form brittle/hard microstructures. There is also the potential to suffer from porosity in the thin, rapid cooling weldments as shown in Figure 2-19 as gases do not have time to escape before the molten metal freezes [35].
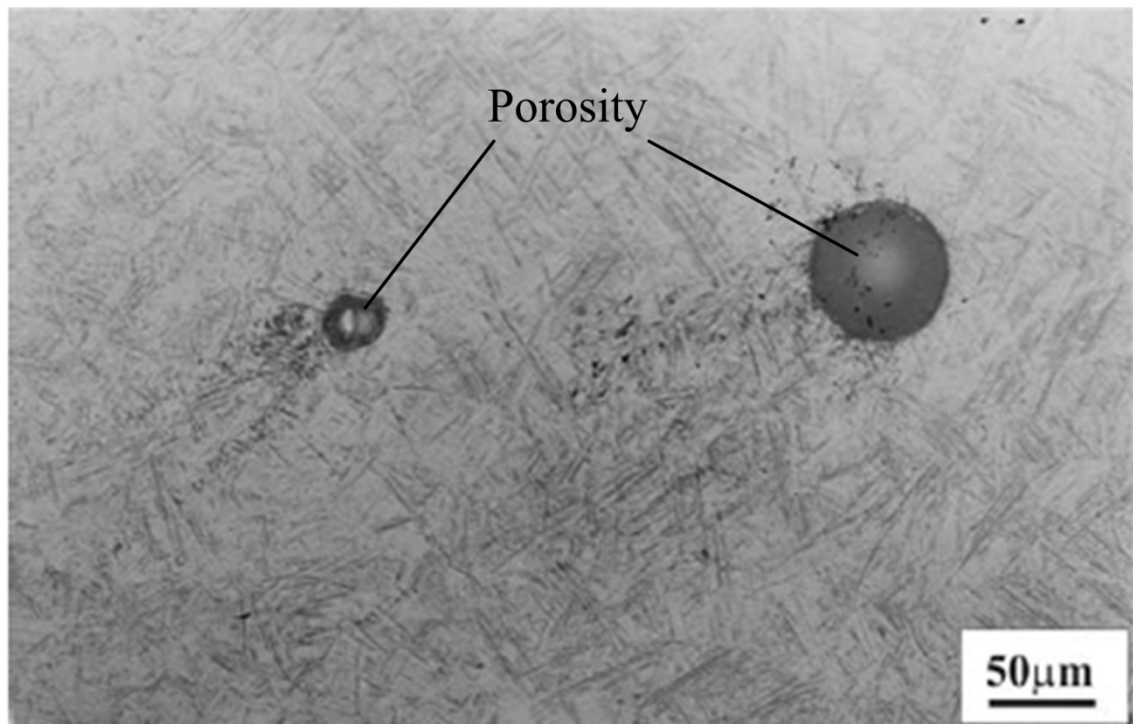
Figure 2-19: Microstructure of electron beam welded joint showing micro-porosity [35].

2.2.3.7 Potential Weld Defects

Like all fusion welding processes there are a range of defects that may form as a result of welding. Common defects that may occur as a result of electron beam welding are shown in Figure 2-20.
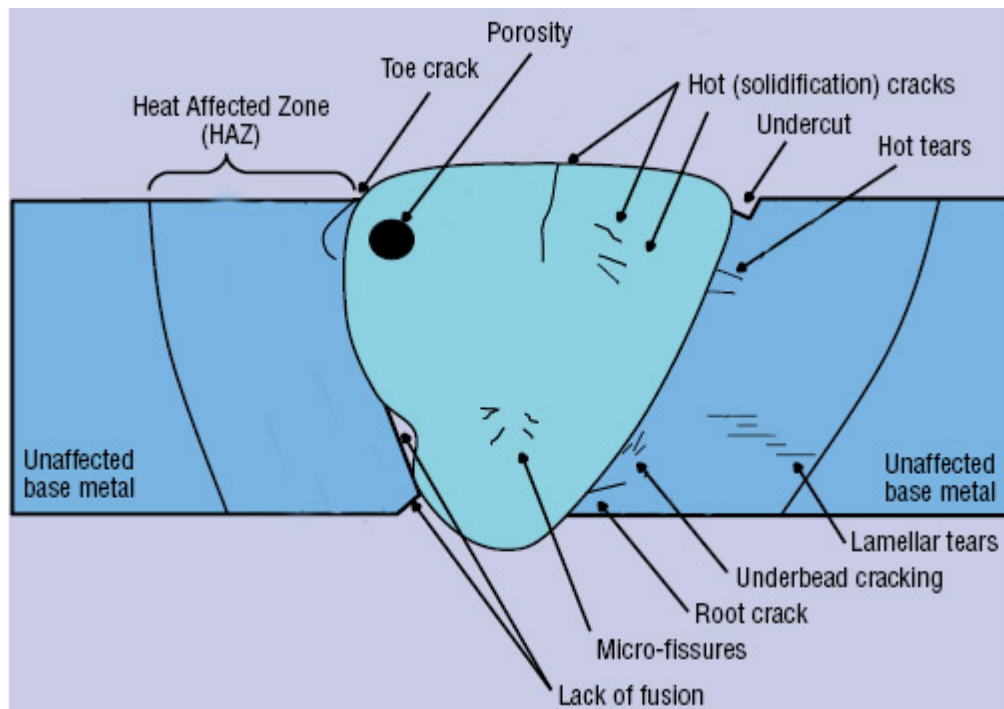
Figure 2-20: Drawing showing possible weld defects [27].

2.2.4 The Current State of Electron Beam Welding

There is a wide range of different types of electron beam welders that are used in industry today. Electron beam welders can be classified in many different ways, but the three main ways to classify EBW machines are by voltage, vacuum level or the mobility of the gun.

2.2.4.1 Vacuum Level

All electron beam guns and columns must be kept at high vacuum, but there are three welding chamber operational vacuum levels that are used for electron beam welding. The traditional vacuum level is a hard vacuum or high vacuum.

High vacuum must have a pressure lower than 1.33×10^{-1} Pa. In high vacuum the electron beam does not have to penetrate atmospheric gases that scatter and decrease the power of the beam. The high vacuum environment produces high purity welds. High vacuum requires long chamber pump down time to achieve the required level of vacuum.

Medium vacuum machines operate between 3.33×10^{-1} Pa and 1.33×10^{-1} Pa. These systems can have more diverse welding chambers that can pump down very quickly. The weld quality from these machines is not as high as that of the high vacuum and some beam power can be lost to the presence of some atmosphere. These machines are not as good for the materials that suffer from atmospheric weld contamination. Medium vacuum systems have huge industrial potential because of their fast turnaround time. Some medium vacuum systems have been adapted to have chambers that parts can pass through allowing for long welds to be performed that could never fit into a conventional chamber.

Non vacuum machines allow for welding to occur at atmospheric pressure. Welding in this mode removes the need to pump down a chamber at all so that weld setup time is limited only by the time it takes to setup the work piece in a jig. Penetration depth can be significantly lower for this method.

2.2.4.2 Gun Mobility

Fixed beam EBW machines as shown in Figure 2-21 have a fixed electron gun assembly and column in the chamber. The work piece is moved around in the chamber while the beam stays stationary. Changes in focal height and minor beam deflections up to 5˚ can be achieved by electrostatic or magnetic lenses and beam deflection coils.
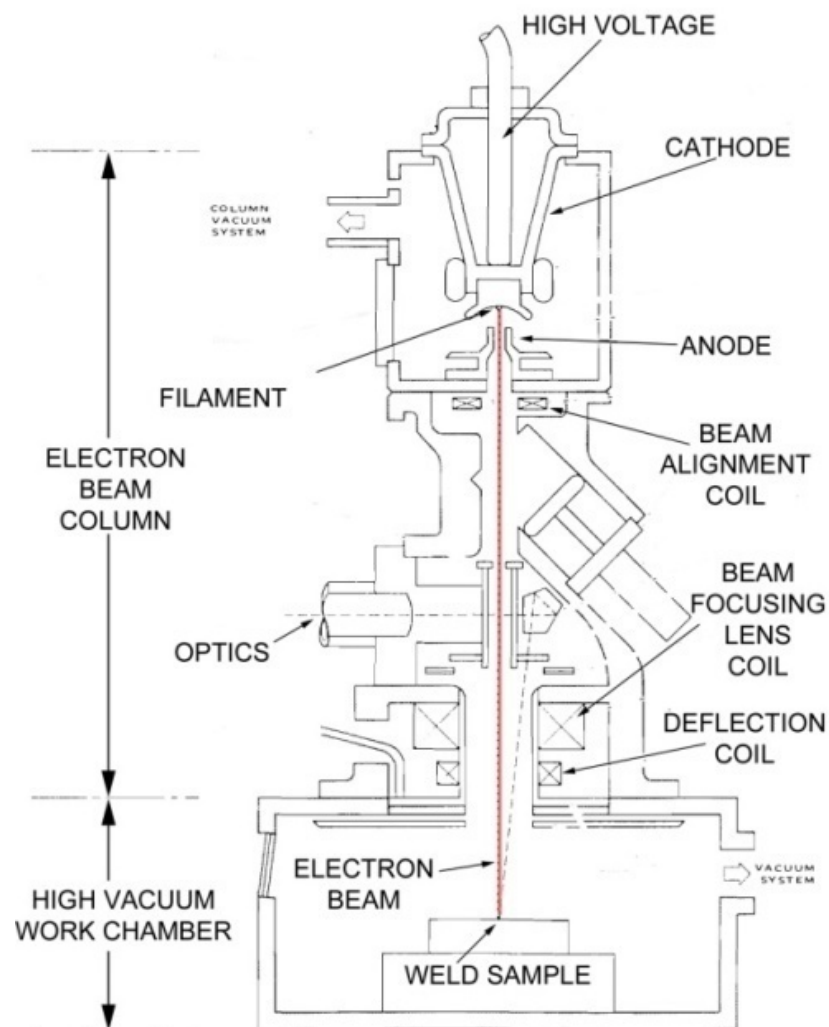
Figure 2-21: Common fixed beam electron beam welder configuration.

Mobile gun EBW machines have a compact gun mounted on a manipulator arm and both the electron gun and the target work piece can be moved. Mobile gun assemblies offer some advantages over the fixed beam assemblies as parts are more easily manipulated for welding and the direction of welding can be varied from the traditional 1G down hand position to generate different effects.

2.2.4.3 Voltage

There are three significantly different voltage classifications for electron beam welding machines, i.e.:

1. Micro electron beam machines.
2. Low voltage machines.
3. High voltage machines.

Micro electron beam machines are usually modified SEM machines that are employed for welding foils. These machines can operate a beam power of up to of 6 Watt at 30 kV [52].

Low voltage machines that operate at 60 kV are often used for simple weld operations on lower value applications and generally have small weld chambers These machines may also be employed for highly automated welding applications [54].

High voltage machines generally operate at 150 kV with large chambers. The quality and depth of penetration of these machines is superior to those of the lower voltages and are used for products with strict quality requirements like the nuclear and aerospace industries.

2.3 Dissimilar Welding

The ability to join dissimilar metals or alloys offers the opportunity to take advantage of different material properties in order to satisfy different requirements for performance [29, 55]. The automotive industry is one area that views joining of dissimilar materials as a gateway for the implementation of lightweight materials into vehicles [55]. The EBW process is particularly well suited for dissimilar joining due to the fact that the high energy density of the process, compared to joining methods like arc welding, allows a greater tolerance for both the differences in thermal conductivity and variation in melting point, between the materials being welded [56].

An example of EBW of dissimilar materials is a composite bandsaw blade, as shown in Figure 2-22, where high speed steel teeth are joined to spring steel to achieve a hard cutting edge on a ductile belt [30].
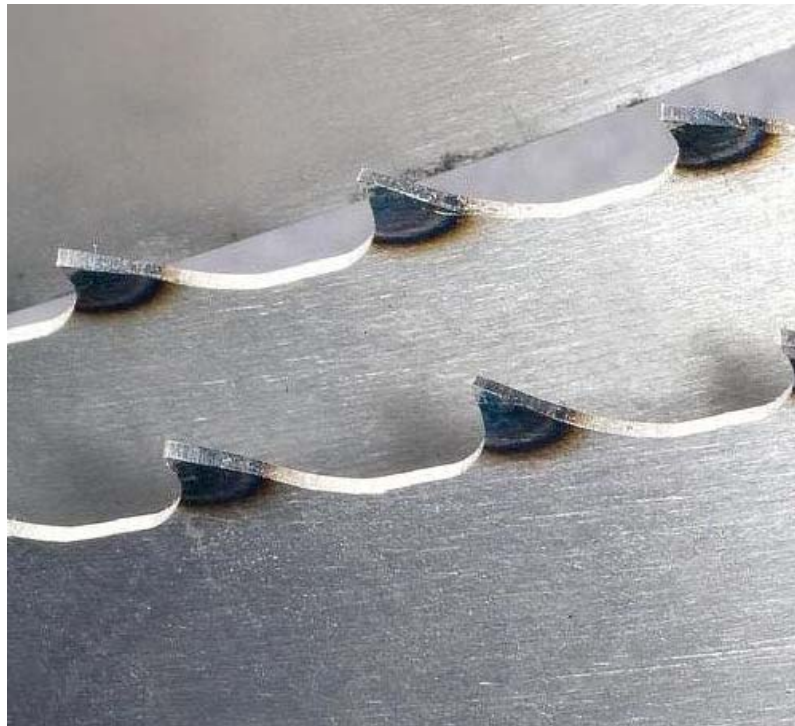
Figure 2-22: Electron beam welded composite steel bandsaw blades.

2.3.1. Dissimilar Weld Properties

When similar metals are welded together the resulting fusion and heat affected zones are symmetrical. When dissimilar metal or alloys are welded the fusion and heat affected zones each side of the centre of the weld are usually unsymmetrical. This unsymmetrical nature is primarily due to the difference in the thermal conductivity of the materials resulting in preferential heat flow though one of the sustrates [56].

Friction stir welding is a process that is currently being researched for applications with dissimilar metal joining. The welding in friction stir welding is performed without having the substrates transitioning into the liquid phase unlike the melting that occurs during the fusion processes [57]. Failures in dissimilar friction stir welds generally occur in the weld interface after the formation of unwanted intermetallic substances

[57]. With titanium being reactive with atmospheric gases there is a high chance of oxygen, hydrogen or nitrogen pickup during the friction stir welding process [57]. Weld generation failures of friction stir welds in high strength materials are often caused by tool failure.

The small weld bead size produced during EBW minimises mixing of dissimilar metals thus limiting the brittle zones arising from any chemical mismatch in the fusion zone, and a low total-heat input per unit length of weld generates less residual stresses than standard welding methods [56].

Dissimilar electron beam welds can suffer distorted fusion and heat affected zones caused by the presence of thermoelectric magnetic fields due to the Seebeck effect. As shown if Figure 2-23, this effect can be a significant problem when performing deep penetration welds as the beam can be deflected and miss the joint in some places [30, 51, 58].
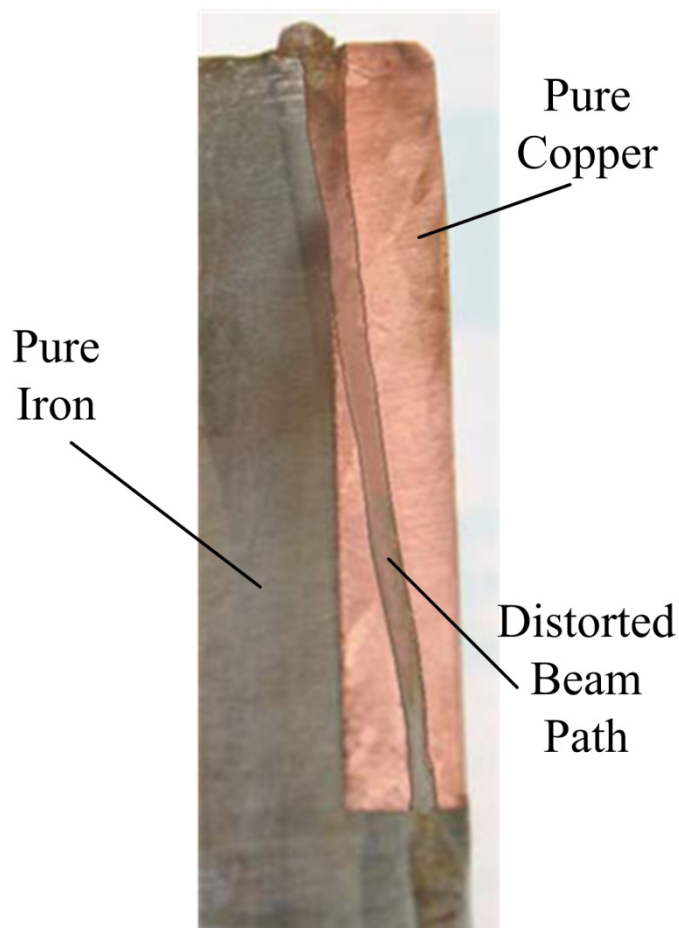
Figure 2-23: Dissimilar electron beam weld deflected by magnetic fields [51].

2.3.2. Predicting Microstructures in Dissimilar Fusion Zones.

If the chemical compositions of two substrates involved in an autogenous weld are known, a rough estimation of fusion zone composition can be made. If it is assumed that 50% of the material in the fusion zone will come from each substrate and that the liquid

metal in the fusion zone will vigorously mix, then the expected composition in the fusion zone can be calculated.

Welding of dissimilar stainless steels is an area that has had a great deal of study for the manufacturing and construction industries. The fusion zone of stainless steel welds can have three main distinctive states, martensitic, ferritic and austenitic, or combinations of the three. Each of the three states has different beneficial and detrimental properties that make them desirable for different applications. The Schaeffler diagram (shown in Figure 2-24), the DeLong diagram (shown in Figure 2-25) and the WRC diagram (shown in Figure 2-26) were developed as a guide for welding stainless steels and predicting the resulting microstructure. Using nickel and chromium equivalents, it is possible to predict the state of the fusion zone after a weld. These diagrams can also be used to predict the fusion zone microstructure for dissimilar stainless steel alloy welds. These diagrams can be used, through the selection of different alloyed filler metals, to create specific final microstructures in the fusion zone, with preferable qualities.
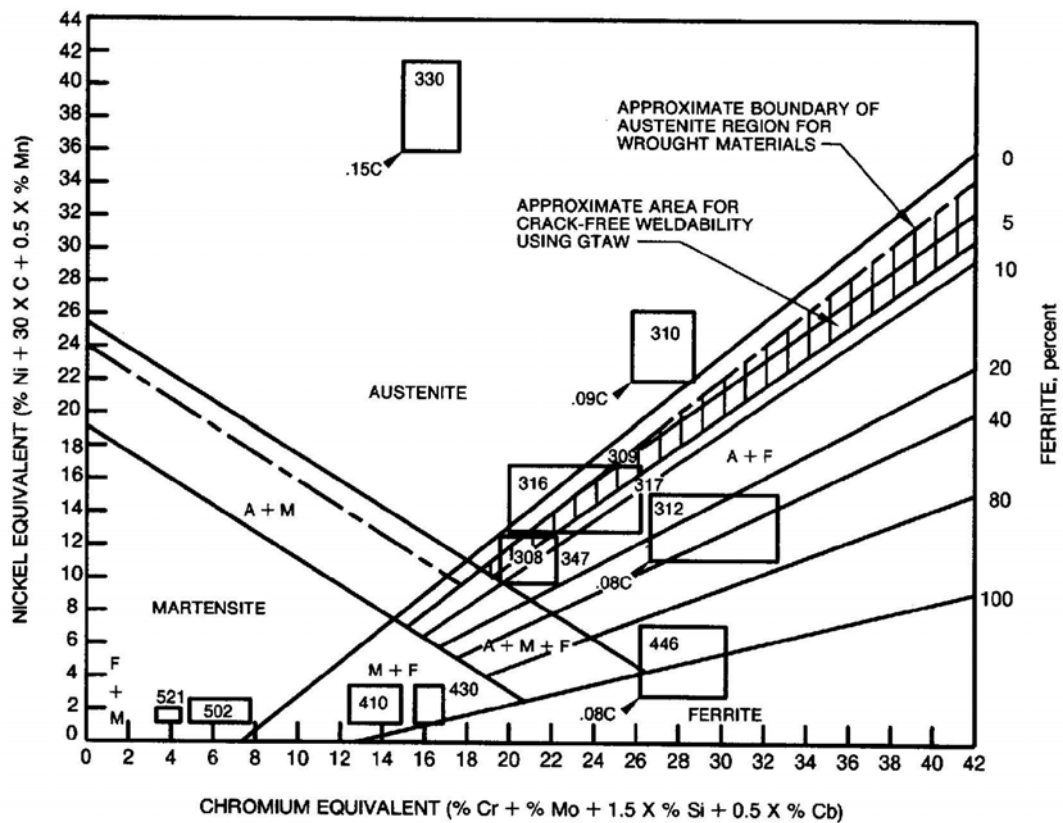
Figure 2-24: Schaeffler diagram showing the effects of dilution on dissimilar steel weldments [25].

The DeLong and WRC diagrams use adjusted nickel and chromium equivalents to more accurately define the structures in specific sections of the original Schaeffler diagram.

38
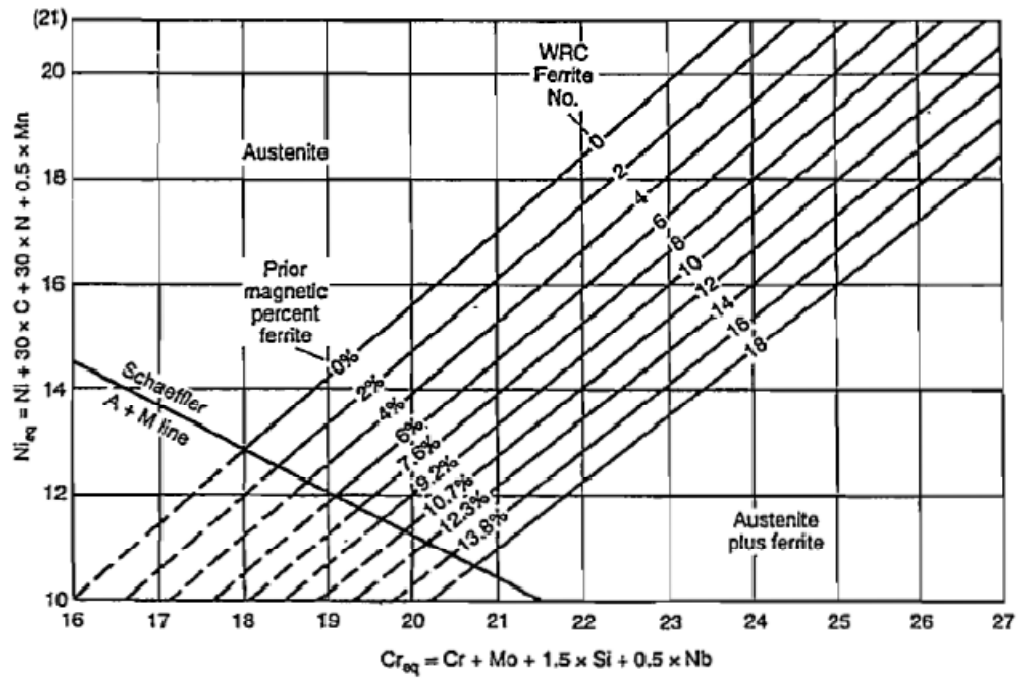
Figure 2-25: DeLong Diagram [59].
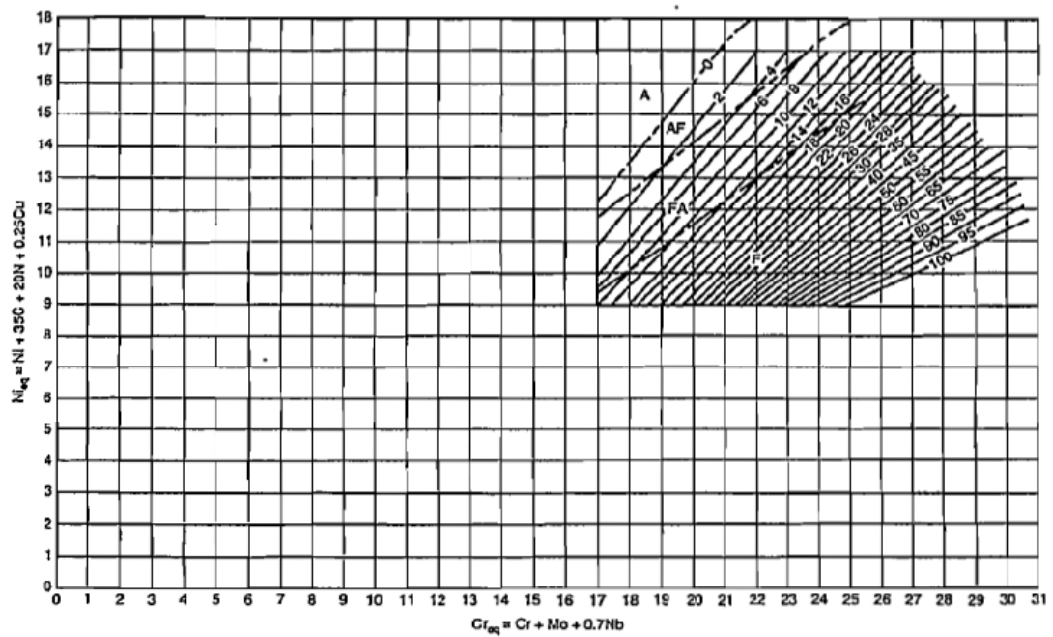
Figure 2-26: WRC 1992 Diagram [59]

39

3.0 Methodology

3.1 Welding

3.1.1 Materials
Three different alloys of titanium were used as welding substrates in this study. They are consisted of a CP Ti, an α+β alloy and a β alloy.

CP Ti – AMS 4901 (0.063)

Thickness of sheet - 1.6mm (0.063 Inches)
Nature of raw material – rolled, annealed condition

α+β alloy Ti-6Al-4V – AMS 4911 (0.063)

Thickness of sheet - 1.6mm (0.063 Inches)
Nature of raw material – rolled, annealed condition

β alloy Ti-5Al-5V-5Mo-3Cr (Ti5553)

Thickness of Plate - 8mm
Nature of raw material – rolled, annealed condition

The chemical composition analysis, shown in Table 3-1, was performed by Spectrometer Services Pty Ltd who are located in Coburg, Victoria, Australia. The methods used for the chemical composition identification employed were ICP scan for the alloying elements plus C, N, O by Leco combustion.

Table 3-1: Chemical Composition (wt %) of the 3 substrates used for welding trials.

	Ti	Al	V	Mo	Cr	Fe	C	O	N	Al_{eq}	Mo_{eq}
CP Ti	Bal	0.16	<0.01	<0.01	<0.01	0.22	0.01	0.28	0.01	2.96	0.55
Ti64	Bal	6.08	3.85	<0.01	0.02	0.17	0.02	0.05	<0.01	6.58	3.03
Ti5553	Bal	5.03	5.10	5.06	2.64	0.38	0.01	0.14	<0.01	6.43	12.80

3.1.2 Electron Beam Welding Machine at ANZGT:

The EBW machine used for all of the trials was a Leybold-Heraeus Vacuum Systems Inc. EBW (Figure 3-1).

Figure 3-1: Leybold-Heraeus Vacuum Systems Inc. EBW chamber (30) 120X60X84.

The machine has a fixed gun with the column (Figure 3-2) located on the top of the chamber. The machine is rated to operate with up to 150kV accelerating voltage and 120mA beam current. The chamber size is 120 inches x 60 inches x 84 inches and accessible through the large front door (Figure 3-1). As the electron gun has a fixed position and direction on the top of the chamber (Figure 3-2) welding from this machine will always occur in a down hand 1G position.

Figure 3-2: Leybold-Heraeus Vacuum Systems Inc. electron beam column.

The maximum vacuum that can be achieved in the chamber is 4×10^{-2} Pa. This means it is classified as operating in high vacuum. The pressure in the chamber and the column are constantly displayed on the vacuum gauges (Figure 3-3) and digitally monitored through the computer control system. The system will not let the beam power up unless the chamber and the column have reached high vacuum.

Figure 3-3: Vacuum gauges for the column and chamber

3.1.3 Sample Preparation and Sample Dimensions

Commercially pure titanium and Ti6Al4V work pieces were cut from the 1.6mm thick sheet using a hydraulic guillotine (Figure 3-4).

Figure 3-4: Hydraulic Guillotine.

The Ti5553 plate was not a comparable thickness to the other titanium substrates so it was electric discharge machined (Figure 3-5) from the 8mm thick plate to sheets of approximately 1.8mm thickness.

Figure 3-5: FST CNC EDM wire cut machine

Ti5553 work pieces for welding trails were then cut from the sheets using electric discharge machine wire cutting (Figure 3-6).
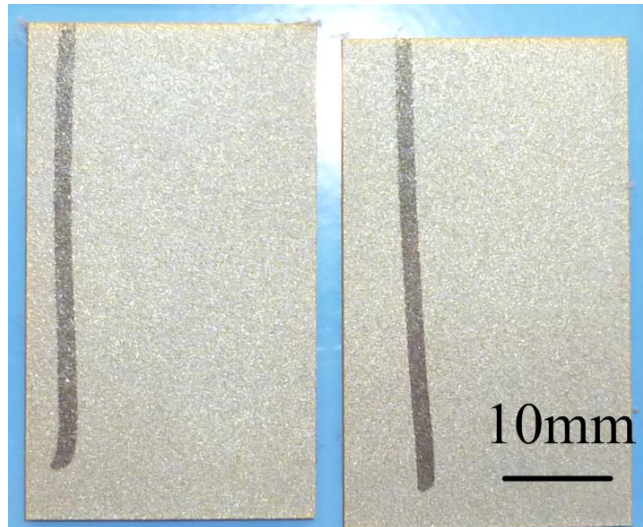
Figure 3-6: Ti5553 sheet cut up into pieces for welding trials.

The surface was linished which reduced the sheet thickness to approximately 1.6mm. Linishing was performed in a manner to minimise the heat build up in the titanium samples that may induce microstructural changes.

Immediately prior to the titanium samples being welded, the butt joint edges were lightly filed and placed together with a light behind to spot any gaps, once the gap gave only a tiny sliver of light all the surfaces of the two work pieces were cleaned with very fine abrasive Scotchbrite pads and acetone. Once the samples were cleaned, they were handled with gloves to prevent any surface contamination.

3.1.4 Welding Setup

Two sample test pieces were secured into the welding jig (Figure 3-7) in the vacuum chamber so the seam was located above the trough.
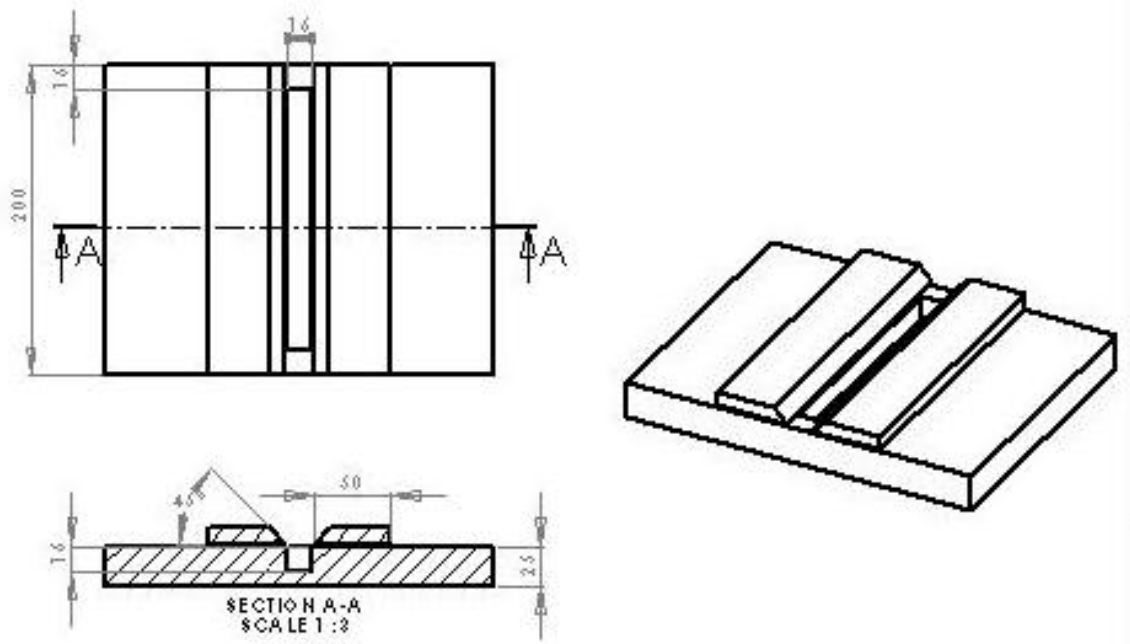
Figure 3-7: Welding jig.

The top surface of the tungsten and copper targeting block was levelled with the work piece surface (Figure 3-8) to ensure that the focal height will be correct. The chamber, work table and weld samples were checked with a Gauss meter (Figure 3-9) to ensure there were no magnetic fields would interfere with the beam operation. The chamber was sealed and the atmosphere pumped down.

Figure 3-8: Target block and welding jig setup in vacuum chamber.

Figure 3-9: Gauss meter.

Once the chamber had reached high vacuum the beam focus height for a minimal beam current was determined on the tungsten and copper targeting block. This was achieved by adjusting the focal height until the electron beam spot became the smallest, most localised, intense spot. Any adjustment above or below this value will widen the spot and decrease its intensity. In general the sequences of EBW are:

- Target start and end weld points and machine power setting parameters are programmed into the EBW computer.
- Manually adjust the power on the 20% power scale to the desired value.
- Run the weld program with predefined parameters and selected power.
- On completion of the welding programme, restore the chamber to atmospheric pressure and remove the weld samples.

3.1.5 Welding Parameters and Welding Combinations

A number of trials were performed to determine the weld parameters to be used for the electron beam welder as the welder had never been used for titanium sheet. Welds were visually inspected by an experienced welding technician [60] and assessed for consistency and penetration.

For all trials the filament current was set to a constant value of 17A before the high voltage was turned on. Welding accelerating voltage was kept constant at 150kV, and all welding occurred with the chamber at high vacuum. The electron beam used a spot focus rather than a deflected beam pattern such as circular.

The two variables that were adjusted to find acceptable weld parameters were beam current and transverse speed, all other variables were set to constant values to make the trails repeatable. It was apparent that a decrease in power density in the weld reduced a scalloping effect in the weld surface. Power settings and speeds for all trials are shown in Appendix B. Final welding parameters for the titanium are given in Table 3-2.

Table 3-2: Welding parameters used in this investigation

Substrate A	Substrate B	Welding current (mA)	Transverse speed	
			(IPM)	mm/s
CP-Ti	CP-Ti	3.2	20	8.5
CP-Ti	Ti-64	3.0	20	8.5
CP-Ti	Ti-5553	3.0	20	8.5
Ti-64	Ti-64	3.0	20	8.5
Ti-64	Ti-5553	3.0	20	8.5
Ti-5553	Ti-5553	3.0	20	8.5

3.2 Metallography and Microscopy

3.2.1 Sample Preparation

Samples to be mounted and polished were cut from the titanium sheet and weld samples using a combination of hydraulic guillotine (Figure 3-4) and cutting wheel (Figure 3-10).

Figure 3-10: Sectioning cutting wheel.

Samples for metallographic study were mounted in bakelite using a Struers LaboPress3 machine (Figure 3-11) with settings: 25kN, 180°C for 7 min, cooling for 4 min.

Figure 3-11: Struers LaboPress 3.

These samples were polished using the standard procedures, given in Table A-6 and Table A-7, using a Struers RotoPol 25 automatic polishing machine (Figure 3-12).

Figure 3-12: Struers RotoPol 25.

Samples were etched via approximately 3 second submersion in a Krolls solution (2mL HF + 10mL HNO3 + 100mL water) and then thoroughly rinsed in purified water, then rinsed with ethanol and blow dried.

Samples of the tensile fracture surfaces were prepared for SEM analysis. A fracture surface sample for each weld combination was prepared using the following steps:
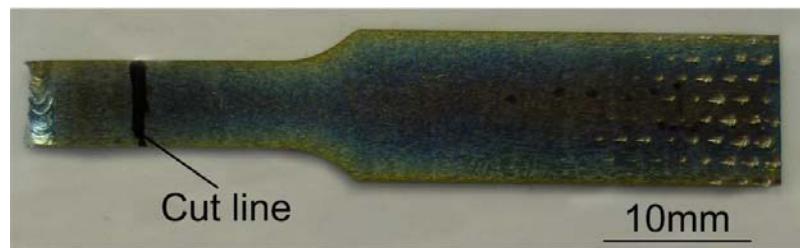
Figure 3-13: Ti5553 to Ti5553 tensile sample marked for cutting before SEM fracture analysis.

The fracture end of the tensile sample was covered with masking tape to protect it from impact damage. A sample shorter than 10mm was cut from the fracture end of the tensile specimen (Figure 3-13) using the sectioning cutting wheel (Figure 3-10). They were cleaned in ethanol for 7 minutes in the ultrasonic cleaner (Figure 3-14) prior to SEM examination.

Figure 3-14: Ultrasonic cleaner.

3.2.2 Optical Microscopy

The examination of metallographic welded joints sections is commonly carried out at two levels of inspection with optical microscopes, macro up to 50x and micro with higher magnifications up to 1000x [27]. The mounted, polished and etched samples, were examined under two different optical microscopes with digital image capture. Macro images were taken with an Olympus SZX9 optical microscope (Figure 3-15a) and Micro images were taken with a Nikon high magnification optical microscope (Figure 3-15b).
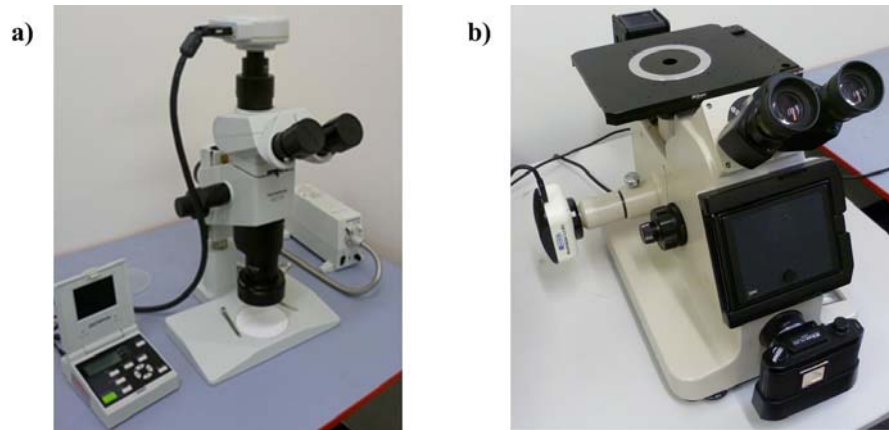
Figure 3-15: a) Olympus SZX9 optical microscope (6.3x to 57x), b) Nikon high magnification optical microscope (50x to 400x).

Images taken from the microscopes were scaled using a 1mm calibrated scale with 10µm divisions (Figure 3-16).
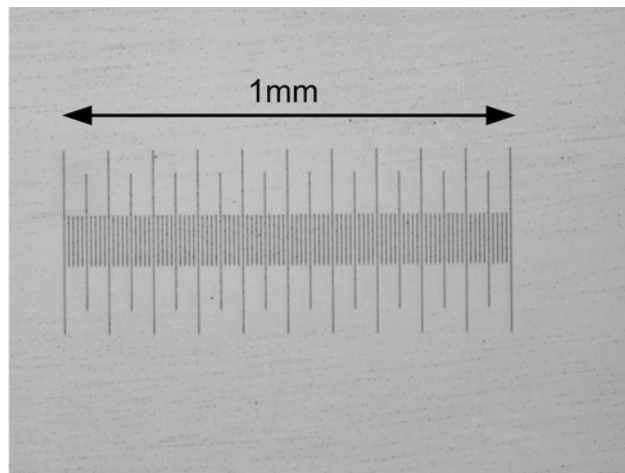
Figure 3-16: Image of the 1mm scale at 50x magnification on the Nikon high magnification optical microscope.

Weld images were examined to identify microstructure and possible defects (shown in Figure 2-20) that may have formed during the welding processes.

3.2.3   Scanning Electron Microscopy (SEM)

SEM fracture images were taken using a Leica Stereoscan 440 scanning electron microscope located at the Defence Technology Agency (DTA) in Devonport. The energy of the microscopes electron beam can range from 300V to 30kV in 10 V increments. The beam current can range from 1 pA to 1μA.

Figure 3-17: Leica Stereoscan 440 SEM.

3.2.4 Electron Probe Microanalysis (EPMA)

Electron Probe Microanalysis (EPMA) is a very powerful tool typically used for quantitative compositional gradients, X-ray mapping to show distribution of elements, and quantitative microstructural analysis. With such capabilities, EPMA has been used significantly in many metallurgical-related areas including welding to understand the chemical composition on a weld cross section. In this project, EPMA was conducted at the Department of Materials Science and Engineering, Lehigh University, Bethlehem – Pennsylvania, USA. The EPMA machine used was a JEOL 733 Superprobe operated at 15kV and 20mA.

Figure 3-18: JEOL 733 Superprobe EPMA machine at Lehigh University.

3.3 Mechanical Testing

3.3.1 Hardness Testing

Hardness tests are a very useful tool for material evaluation and are often used in quality control of manufacturing processes and research and development efforts. Hardness, can be loosely correlated to tensile strength for many metals, and is a good indicator for wear resistance and ductility of the metal. Micro-indentation tests use lower applied forces and leave smaller indentations than standard hardness tests, which allows testing to be performed in areas of materials that are too small for standard indentation tests. Because the area of indentation is so small micro-hardness tests can reveal hardness variations that may exist within a material, as a result a single test value may not be representative of the bulk hardness of a material [61].

All samples tested using either Knoop hardness or Vickers hardness methods were mounted, polished and etched samples.

In both Knoop and Vickers micro-hardness test methods, a hardness number is determined based on the size of a very small surface indentation caused by a diamond tipped pyramid shaped indenter after an application of a force in the range of 0.00981N to 9.81N (1 to 1000 gf).

A Knoop indenter has elongated pyramid geometry as shown in Figure 3-19.
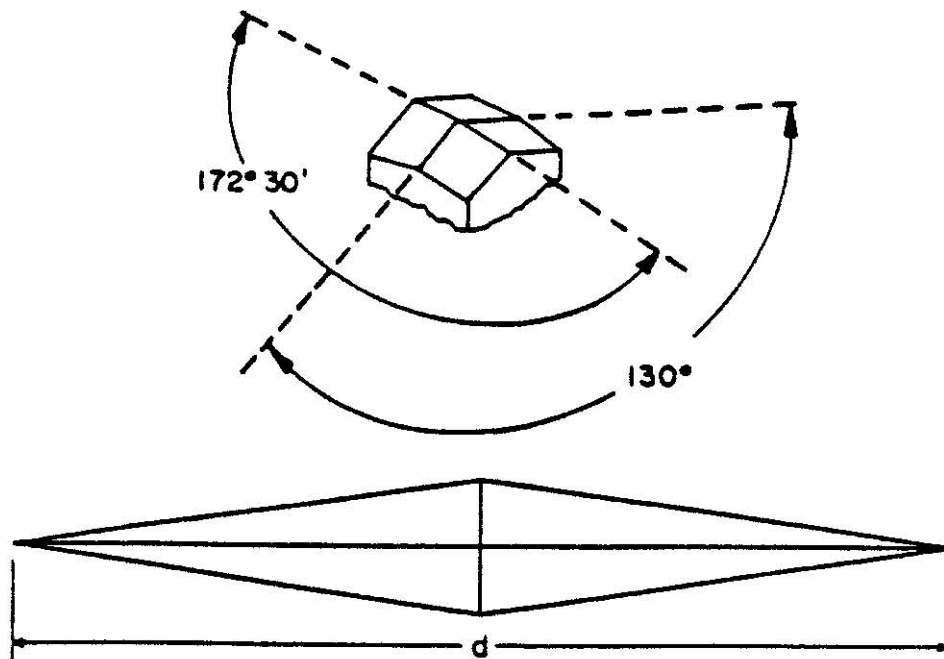
Figure 3-19: Knoop indenter geometry [61].

Knoop tests were performed on the weld transverse cross sections of the CP Ti to CP Ti, Ti64 to Ti64 and Ti64 to CP Ti welds at 0.1mm intervals, well over the minimum required spacing shown in Figure 3-20.

dk = length Knoop diagonal
w = width Knoop diagonal
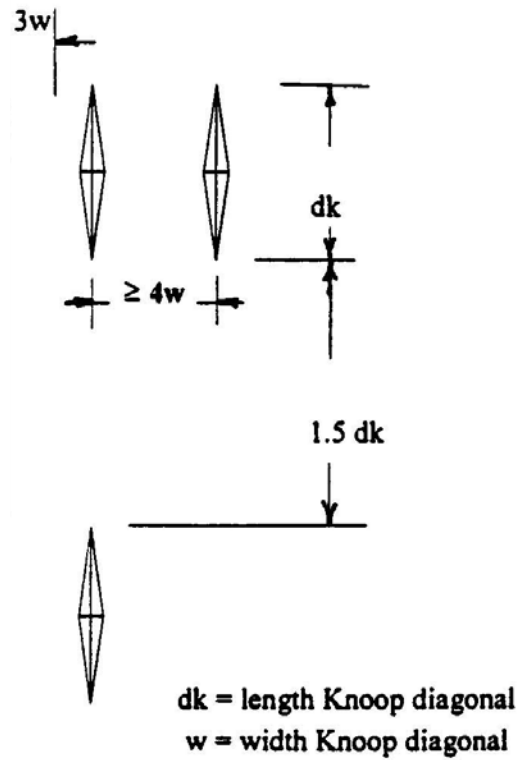
Figure 3-20: Closest permitted spacing for Knoop indentations [61].

A LECO M-400-G1 Knoop hardness tester (Figure 3-21) with settings of 100 gf (0.980665N) for 25 seconds was used. The length of the indentations were measured using a light microscope equipped with a filar type eyepiece connected to a video display.

Figure 3-21: LECO M-400-G1 Knoop hardness tester.

A Vickers indenter has square pyramid geometry as shown in Figure 3-22.
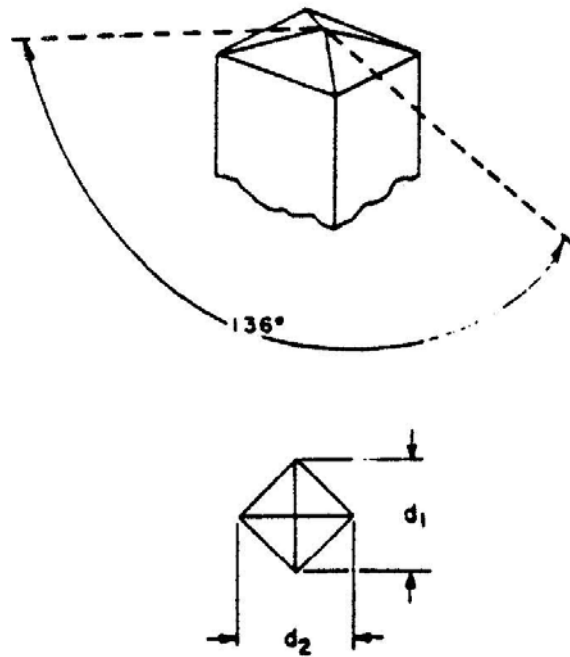
Figure 3-22: Vickers indenter geometry [61].

Vickers tests were performed across the weld transverse cross section of all the weld substrate combinations at centre to centre intervals of 0.2mm, which is compliant with the minimum spacing shown in Figure 3-23.

dv = length Vickers diagonal
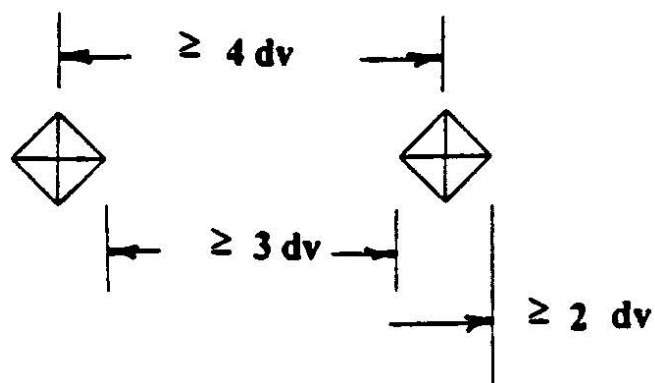
Figure 3-23: Closest permitted spacing for Vickers indentations [61].

A Struers Duramin-1 micro-Vickers hardness tester (Figure 3-24) with settings of 300 gf (2.943N) for 13 seconds was used. The size of the indentations was measured using a light microscope equipped with a filar type eyepiece that was part of the indentation machine.

Figure 3-24: Struers Duramin-1 micro-Vickers hardness tester.

3.3.2 Bend Testing

Bend tests were performed on the top face and root face for CP Ti to CP Ti, CP to Ti64 and Ti64 to Ti64 weld samples. No Ti5553 weld combinations were tested due to insufficient material availability. Bend test specimens were 170mm by 25mm as shown in Figure 3-25.

Figure 3-25: Ti6Al4V to Ti6Al4V bend specimen prior to bending.

The bend test procedure was based on an alternative wrap-around guided bend test bend fixture shown diagrammatically in Figure 3-26 [62].
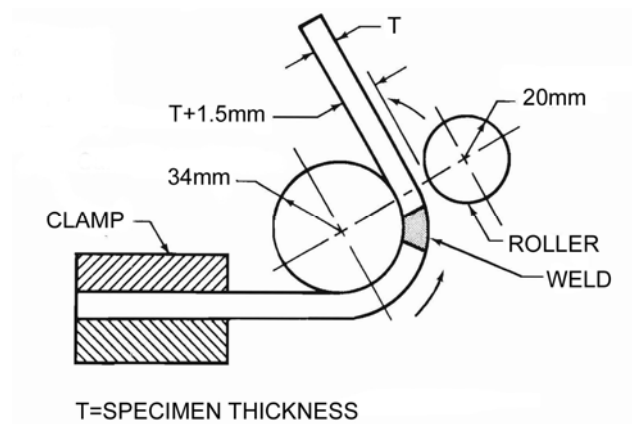
Figure 3-26: Alternative wrap-around guided bend fixture [62].

The bend specimens have one end clamped into the bend fixture so it will not slide during bending (Figure 3-27a). The outer roller is rotated at a consistent rate 180° from its start position (Figure 3-27b). The outer roller is removed and the bend sample is removed from the bending rig and the outer weld surface is visually inspected. The fusion and HAZ of the bend sample must be completely within the bent portion of the sample.
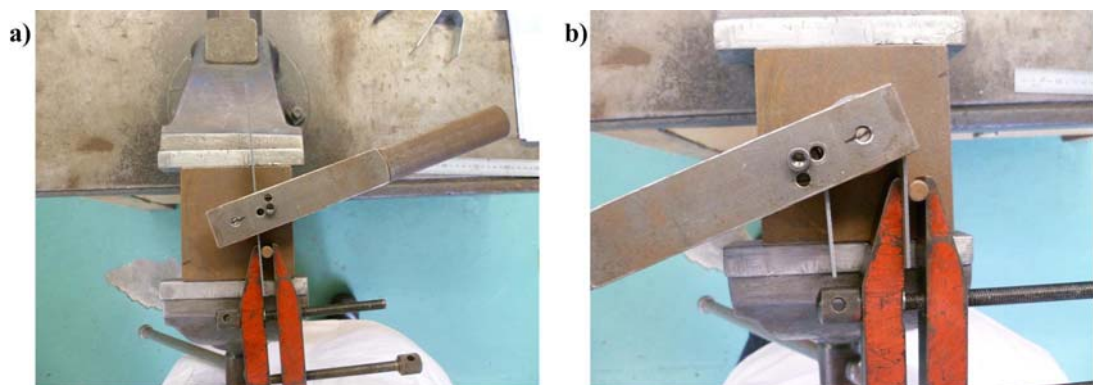
Figure 3-27: a) Bending rig set up ready to bend. b) Bending rig in final position after 180° bend.

Initial visual inspections were performed to identify any large cracks. A two stage dye penetrant was then used to identify if any micro-cracks had occurred during bending. A red penetrating dye was sprayed over the bend surface and left for ten minutes (Figure 3-28a). The dye was removed with the provided cleaning solution. Developer was sprayed on to the cleaned surface and inspected after ten minutes (Figure 3-28b). Any micro-cracks or surface cavities appear as thin pink lines or dots.
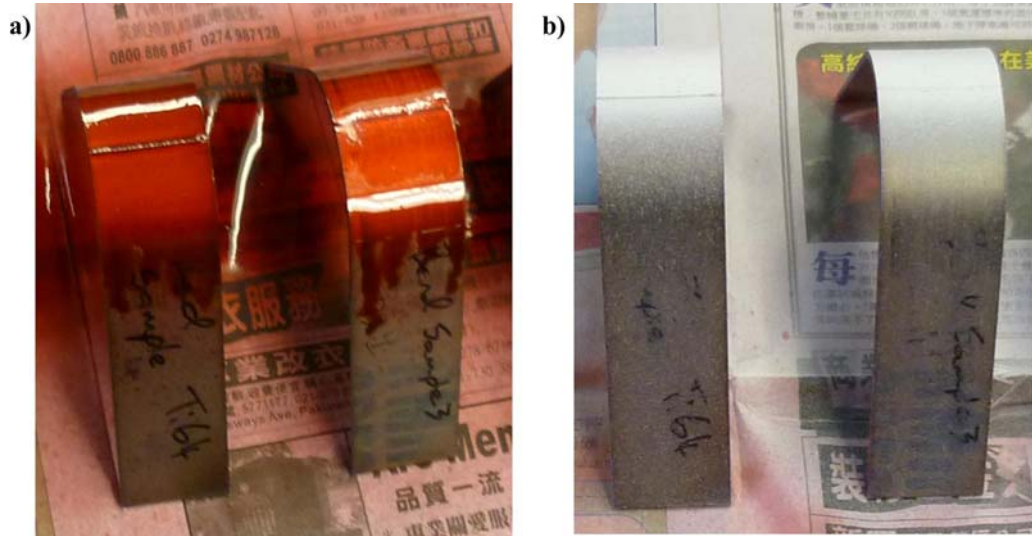
Figure 3-28:a) Bend samples covered in penetrant, b) Bend samples covered in developer.

The elongation that occurs on the outer surface of the bend sample can be calculated using the following equation:

$$\text{Elongation } \% = e_b = \frac{\text{sample thickness}}{2 \times \text{internal radius} + \text{sample thickness}} \times 100$$

$$= \frac{T}{2R + T} \times 100$$

(Equation 3.1)

For the configuration of the bending rig used and the material thickness, the elongation of the bend sample top surfaces should be as calculated below.

$$e_b = \frac{1.6}{2 \times 34 + 1.6} \times 100 = 2.299\%$$

(Equation 3.2)

3.3.3   Tensile Testing

3.3.3.1 Tensile Sample Preparation

A sub-sized dog-bone tensile test specimen as described in ASTM E 8M – 04 [63] was used. An example of a tensile specimen before testing is shown in Figure 3-29. A fully dimensioned drawing of the specimens is shown in Figure A-3.

Figure 3-29: CP Ti base metal tensile specimen.

Tensile samples were cut from the base material sheets and welded sheets as shown in Figure 3-30 using the EDM Wire Cutter (Figure 3-5). EDM wire cut surfaces were linished to remove the EDM machining lines.
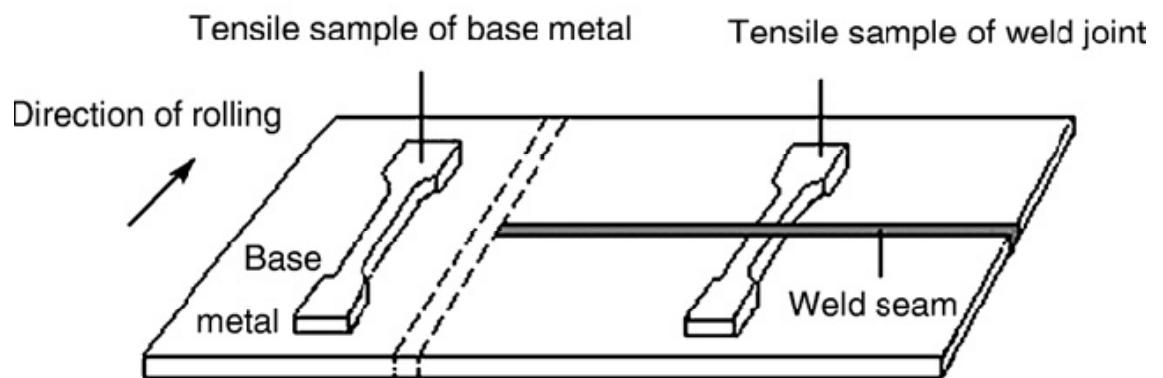
Figure 3-30: Position of tensile samples [64].

3.3.3.2 Tensile Testing Procedure

Tensile testing was performed on two different occasions during the research with different measurement apparatus operating on each occasion.

Figure 3-31: Tinius Olsen H50Ks tensile testing machine.

The first set of tensile testing was performed to find out if undersized tensile specimens of titanium could be tested in the AUT tensile testing machine (Figure 3-31). Only commercially pure titanium and Ti6Al4V base metals and weld combinations were used during this stage of testing. All tensile specimens were tested at a constant jaw separation speed of 3mm/minute. Initial testing measured only the load and separation of the tensile jaws. Minor slipping occurred as the jaws bit into the tensile samples at minor loads. Once the jaws gripped the tests were consistent. The data collected from these tensile tests were good indicators but were not measured accurately enough to give stress strain diagrams. A print out of the force/extension graph for the test was printed.

The second set of tensile testing used all three of the alloy base metals and every similar and dissimilar weld combination. Two tensile specimens were tested for each of the base metal or weld conditions. The cross-section of each tensile sample was measured before it was placed in the tensile machines jaws. Elongation during testing of the tensile specimens was measured with a 25mm gauge length extensometer as shown in Figure 3-32. All tests were performed at a constant 3mm/min jaw separation speed. Tensile data was logged by the Tinius Olsen tensile program Navigator, and output to data files giving extensometer elongation, applied load, and other parameters for later study.
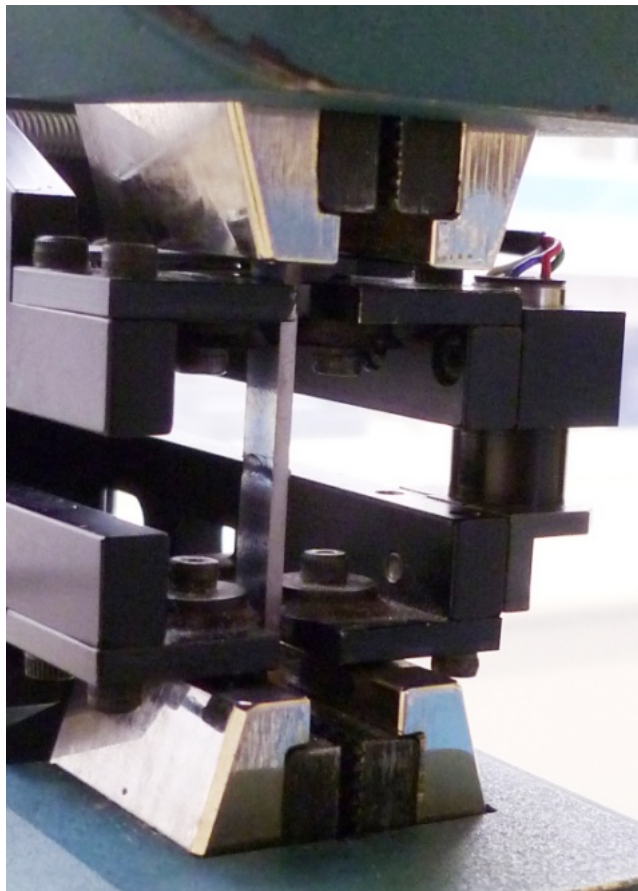
Figure 3-32: Tensile sample loaded into tensile jaws with 25mm extensometer.

3.3.3.3 Aramis System - Strain Measurement

Strain localisation at the weld is difficult to measure because the width of the electron beam welds in this study were typically around 2mm. Therefore the Aramis system was employed (Figure 3-34). Aramis is a system that uses a pair of high speed cameras and a computer/software to perform 3D image correlation photogrammetry to measure the total deformation of complex shapes. The system tracks various positions on an object under load over time to give the displacement, the plain strain and a 3D contour of the object.

Figure 3-33: Typical 3D Aramis equipment [65].

Aramis was used during tensile tests conducted on all of the titanium weld combinations at the Department of Materials Science and Engineering, Lehigh University, Bethlehem – Pennsylvania, USA.
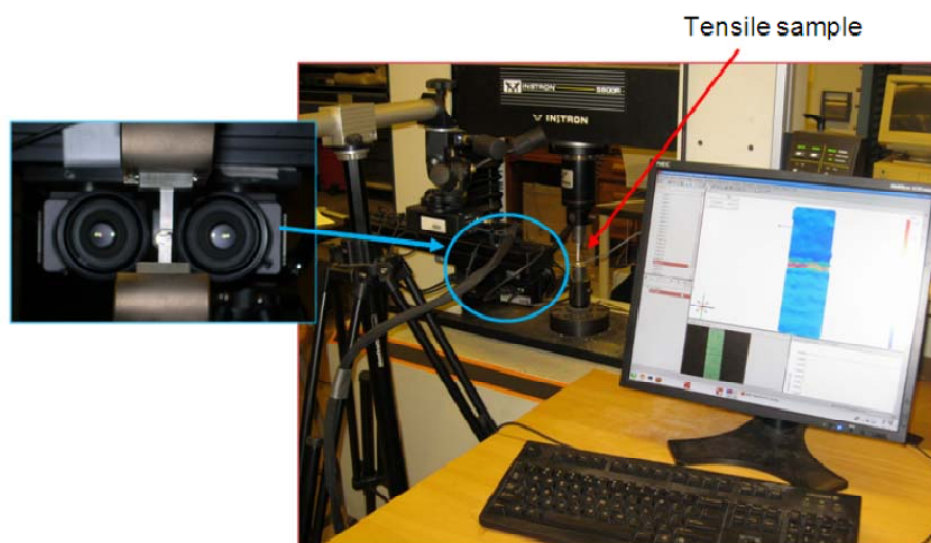
Figure 3-34: Aramis setup at Lehigh University with a titanium tensile sample (Appendix F-2).

4.0 Results

4.1 Weld Dimensions

The weld zone dimensions (Table 4-1) were obtained from an average of optical measurements of the top and bottom surfaces of the weldments shown in Appendix C.

Table 4-1: Weld parameters and fusion zone dimensions

Substrate A	Substrate B	Welding current (mA)	Weld zone top width (mm)	Weld zone bottom width (mm)
CP-Ti	CP-Ti	3.2	2.75 ± 0.05	1.24 ± 0.11
CP-Ti	Ti-64	3.0	2.66 ± 0.06	1.25 ± 0.05
CP-Ti	Ti-5553	3.0	2.61 ± 0.04	0.65 ± 0.44
Ti-64	Ti-64	3.0	2.61 ± 0.06	1.28 ± 0.04
Ti-64	Ti-5553	3.0	2.57 ± 0.05	0.67 ± 0.16
Ti-5553	Ti-5553	3.0	2.25 ± 0.16	1.01 ± 0.12

4.2 Microstructures

4.2.1 Base Metal Microstructure

Photomicrographs were taken of all of the base metals that had been mounted, polished and etched. The CP Ti substrate base metal microstructure shown in Figure 4-1 has uniform equiaxed grains. These grains are 100% α phase.
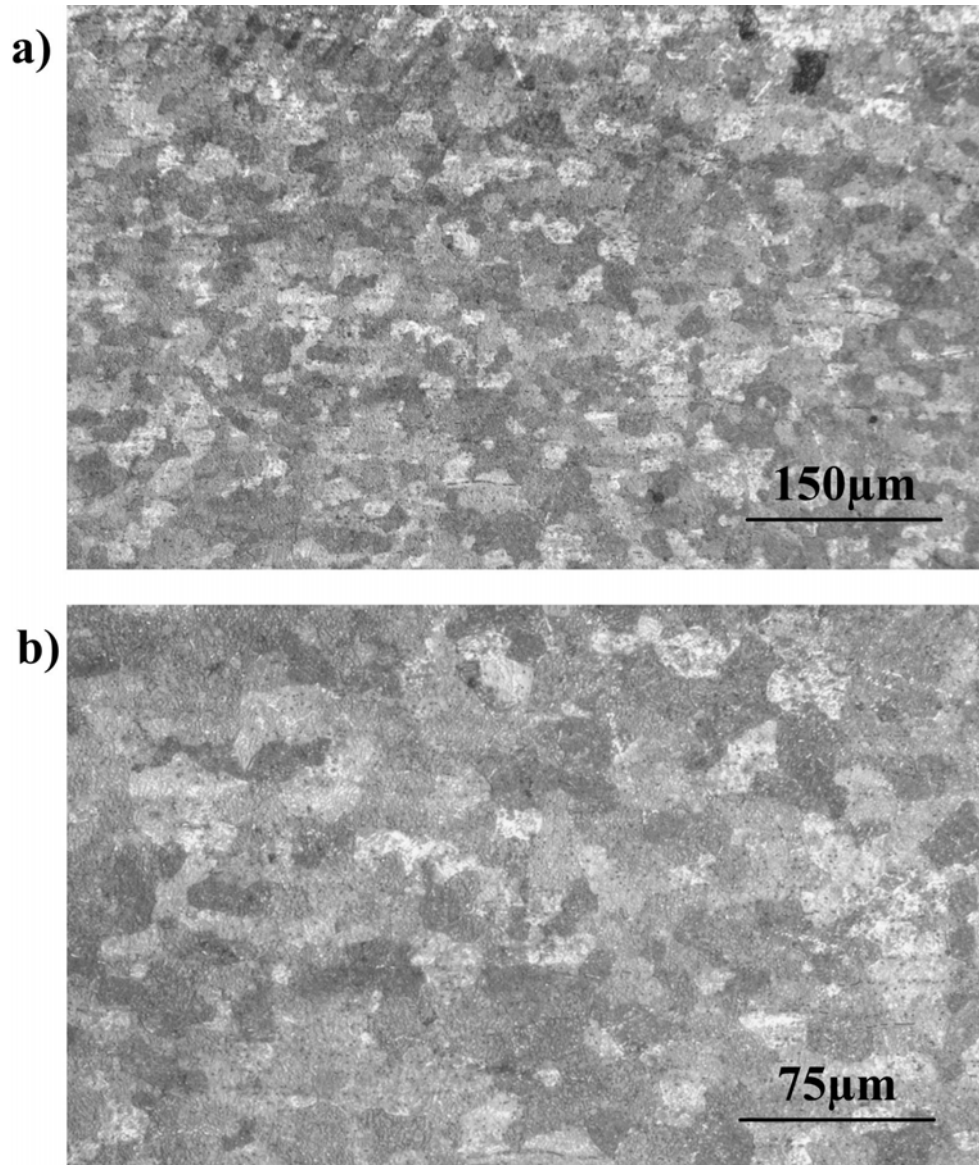
Figure 4-1: CP Ti base metal microstructure a) 100x mag b) 200x mag.

The Ti6Al4V substrate base metal microstructure shown in Figure 4-2 has uniform grains, with a slight horizontal elongation due to the rolled nature of the sheet. These grains are α phase with β phase present on the grain boundaries. The α grains in this Ti6Al4V are smaller than the commercially pure titanium grains shown in Figure 4-1.
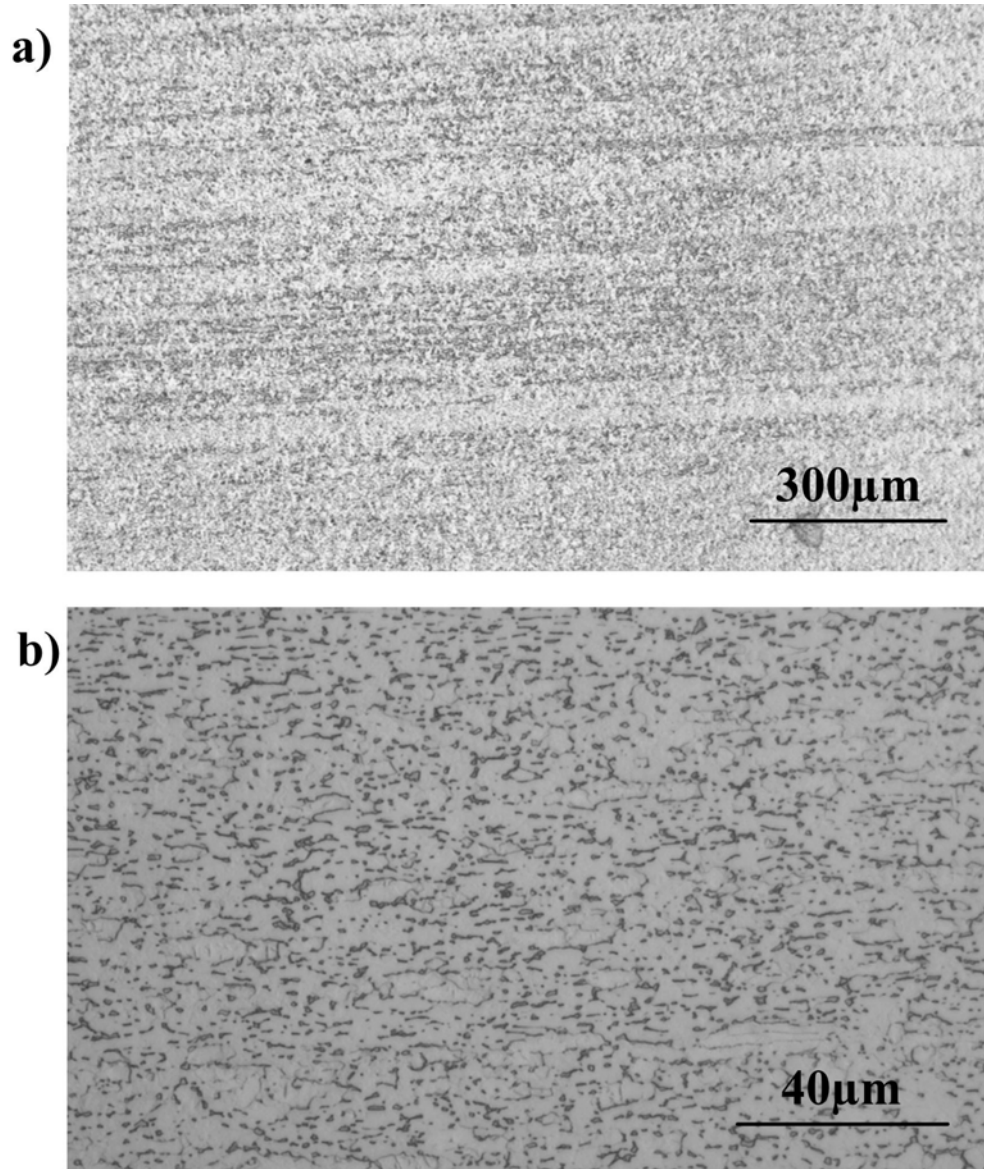
Figure 4-2: Ti6Al4V Base metal microstructure a) 50x mag b) 400x mag.

The Ti5553 substrate base metal shown in Figure 4-3 has very fine grains. Figure 4-3a) shows a horizontal grain pattern following the rolled nature of the plate. The grains in this Ti5553 base metal are mostly β phase with uniformly distributed α phase precipitate.
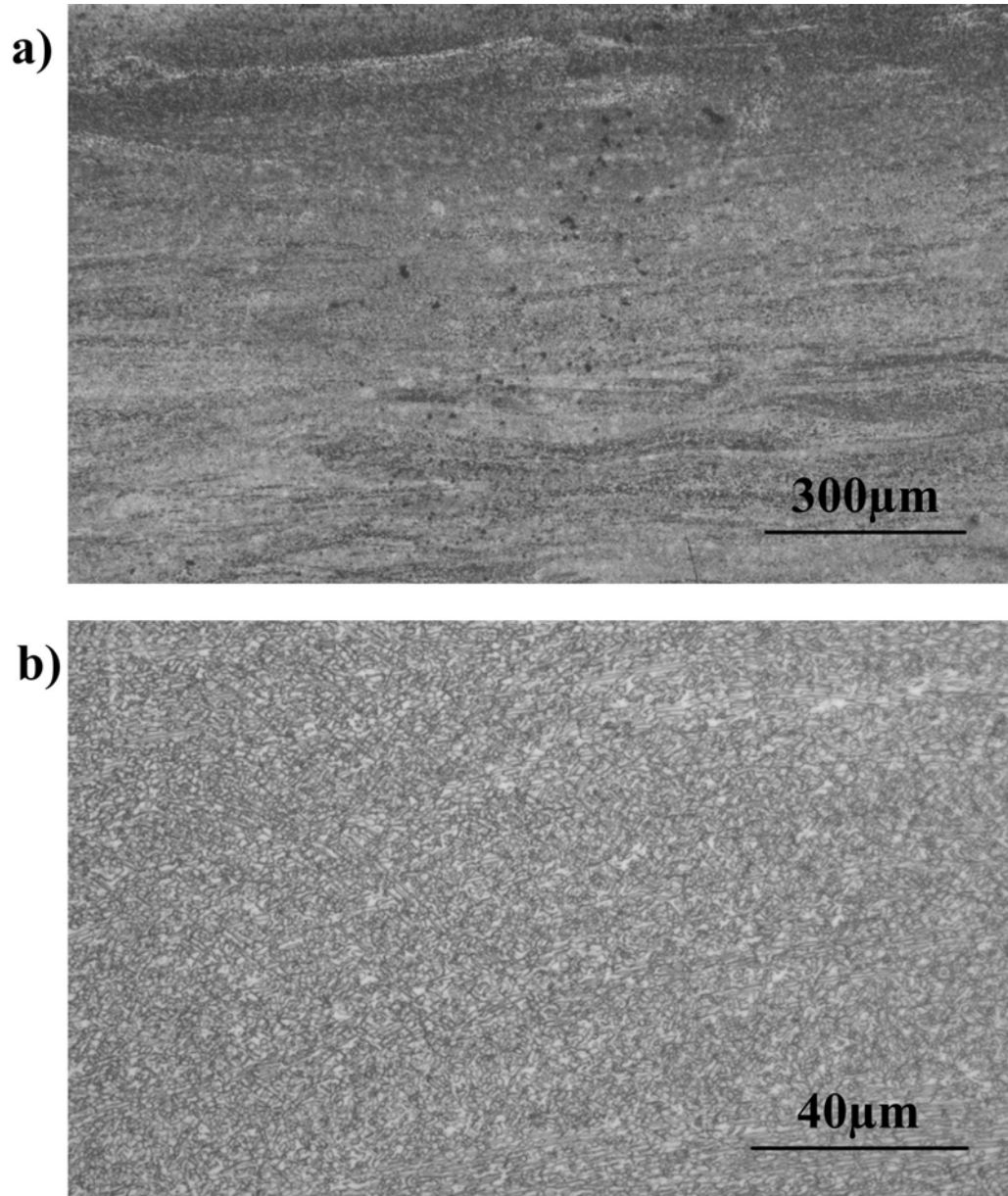
Figure 4-3: Ti5553 Base metal microstructure a) 50x mag b) 400x mag.

4.2.2 Weld Transverse Surfaces
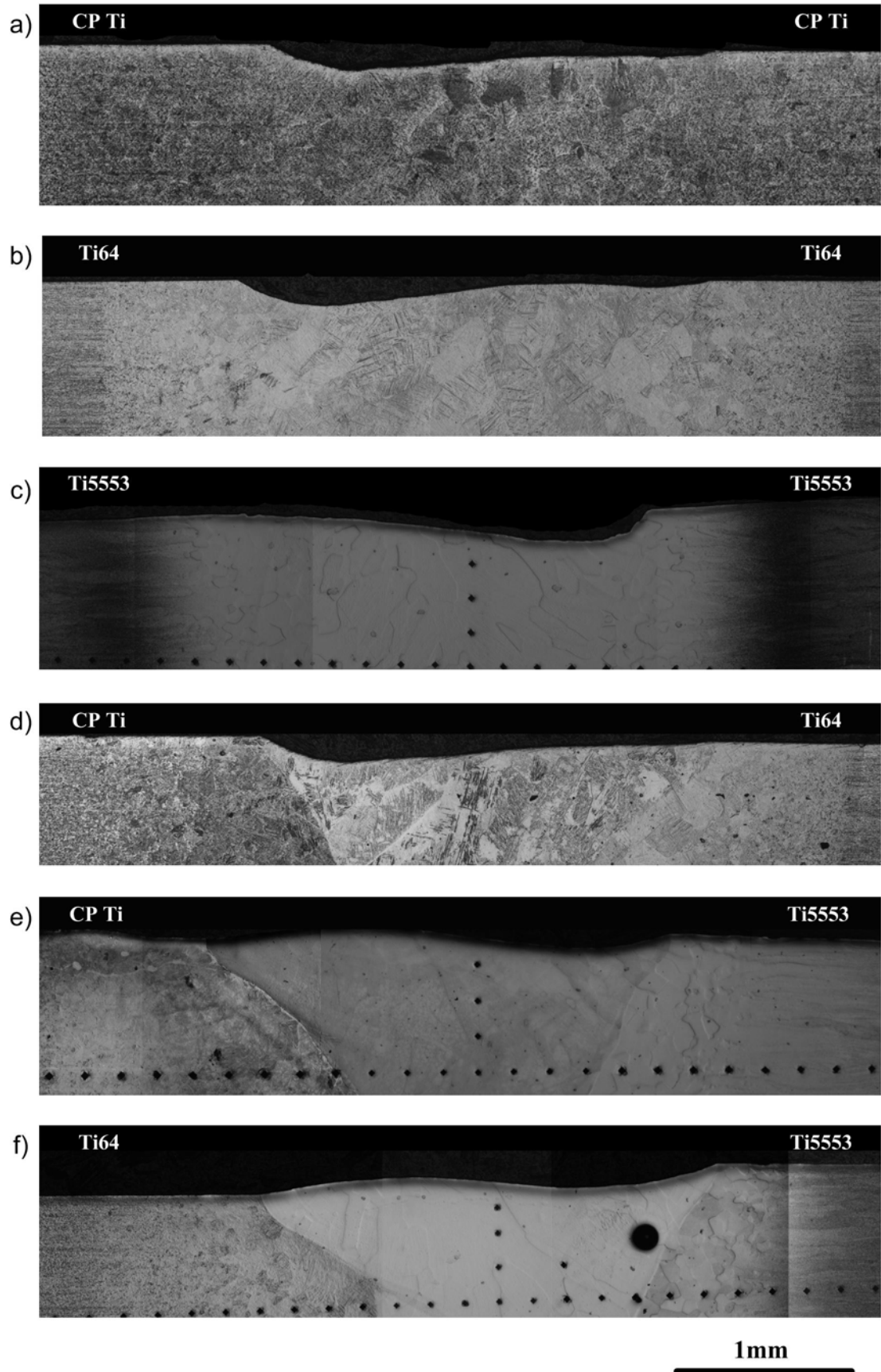
Figure 4-4: Composite images showing the top of the weld transverse cross sections for all weld combinations.

4.2.3 Heat Affected Zone Microstructure

The microstructures in the heat affected zone for each of the different substrates were observed on mounted polished and etched samples.

The HAZ microstructure for the CP Ti, shown in Figure 4-5 and Figure 4-6, consists of acicular transformed β microstructure showing former β grain boundaries.
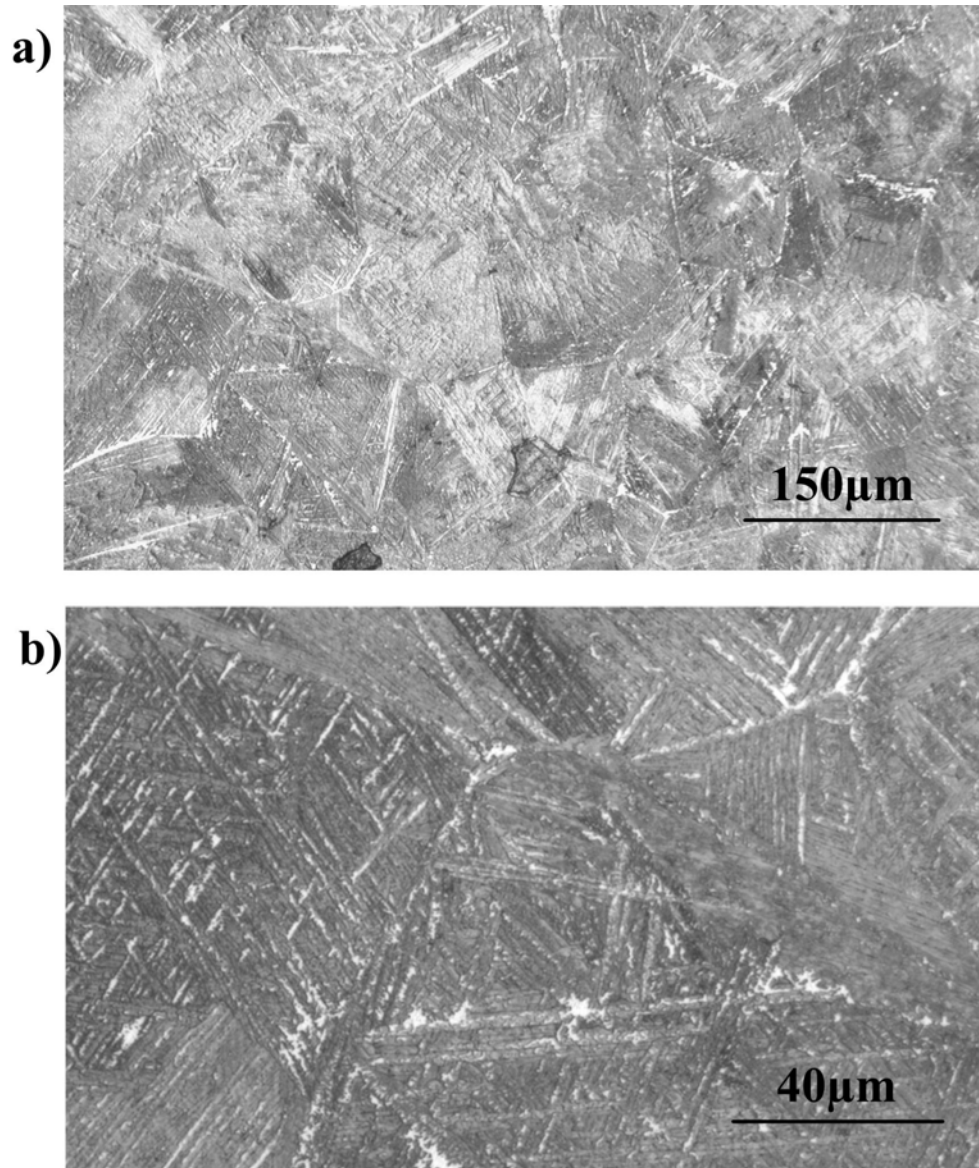
Figure 4-5: CP Ti HAZ microstructure a) 100x mag b) 400x mag.

The cross hatched Widmanstätten pattern shows the transformation of the β to either α phase or a combination of both α phases +α' martensite.
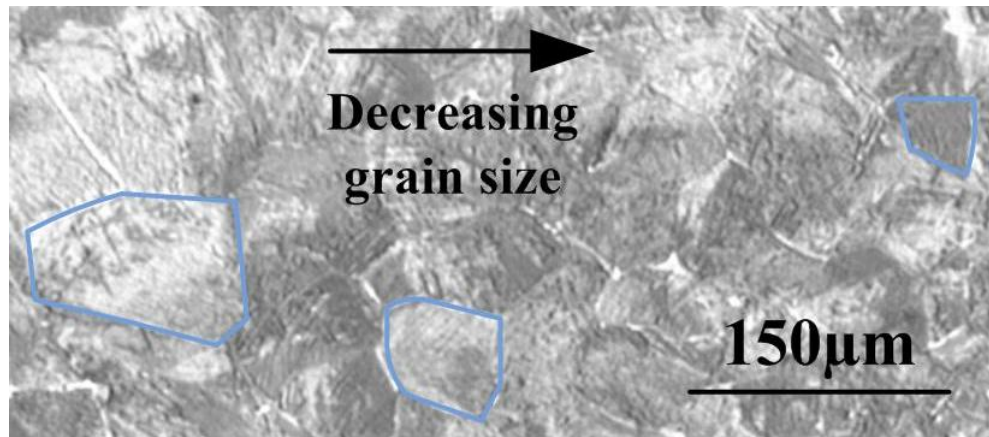
Figure 4-6: CP Ti HAZ showing former β grain size.

Figure 4-6 shows the size of the former β grains increase from the base metal side of the HAZ (right) to the fusion zone side of the HAZ (left). The cross hatched microstructure is comparable to the CP Ti microstructure shown in Figure 2-6b.

The HAZ for the Ti6Al4V in Figure 4-7 shows acicular transformed β microstructure with showing former β grain boundaries. The cross hatched Widmanstätten pattern shows the transformation of the β phase to either just α phase or α+α' phases on cooling.
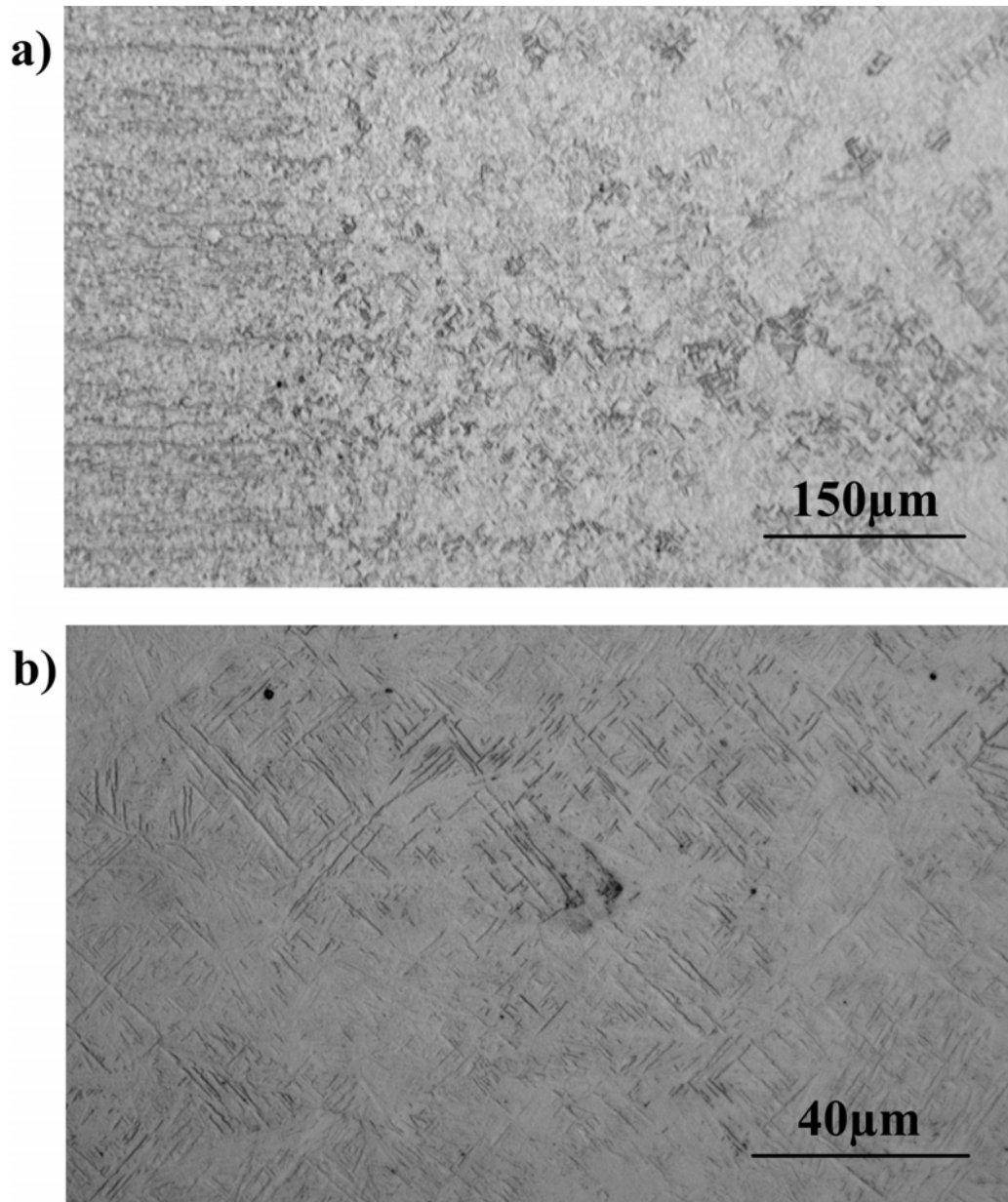
Figure 4-7: Ti6Al4V HAZ microstructure a) 100x mag b) 400x mag.
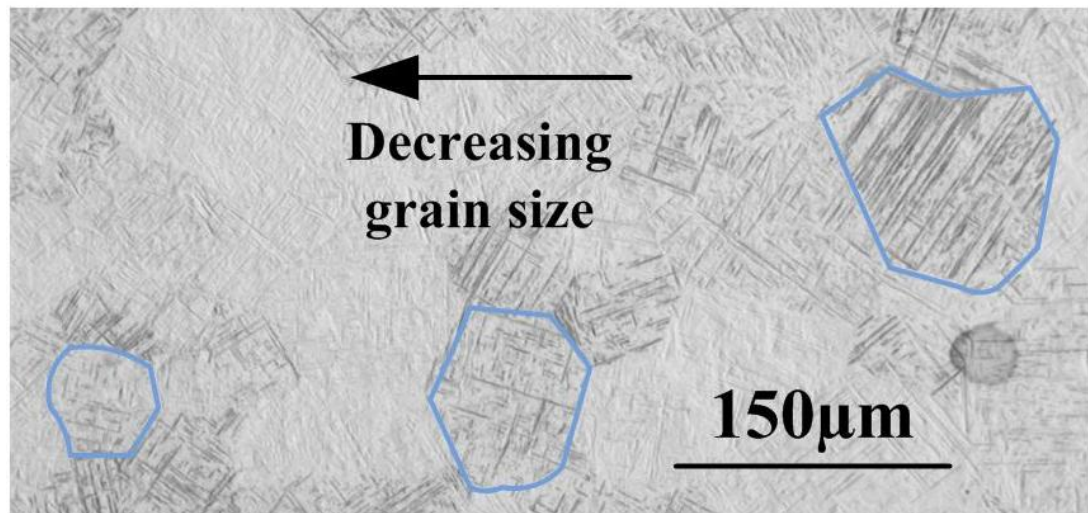
Figure 4-8: Ti64 HAZ showing former β grain size.

Figure 4-8 shows the size of the former β grains increase from the base metal side of the HAZ (on the left) to the fusion zone side of the HAZ (on the right).

Figure 4-9a and Figure 4-10 shows the HAZ for the Ti5553 had growth of β grains. The size of the β grains increases from the base metal side of the HAZ (right side) to the fusion zone side of the HAZ (left side). The higher magnification in Figure 4-9b shows the β grains did not transform into α phase on cooling like they had with Ti6Al4V or the commercially pure titanium so there is no cross hatched pattern on the grains.
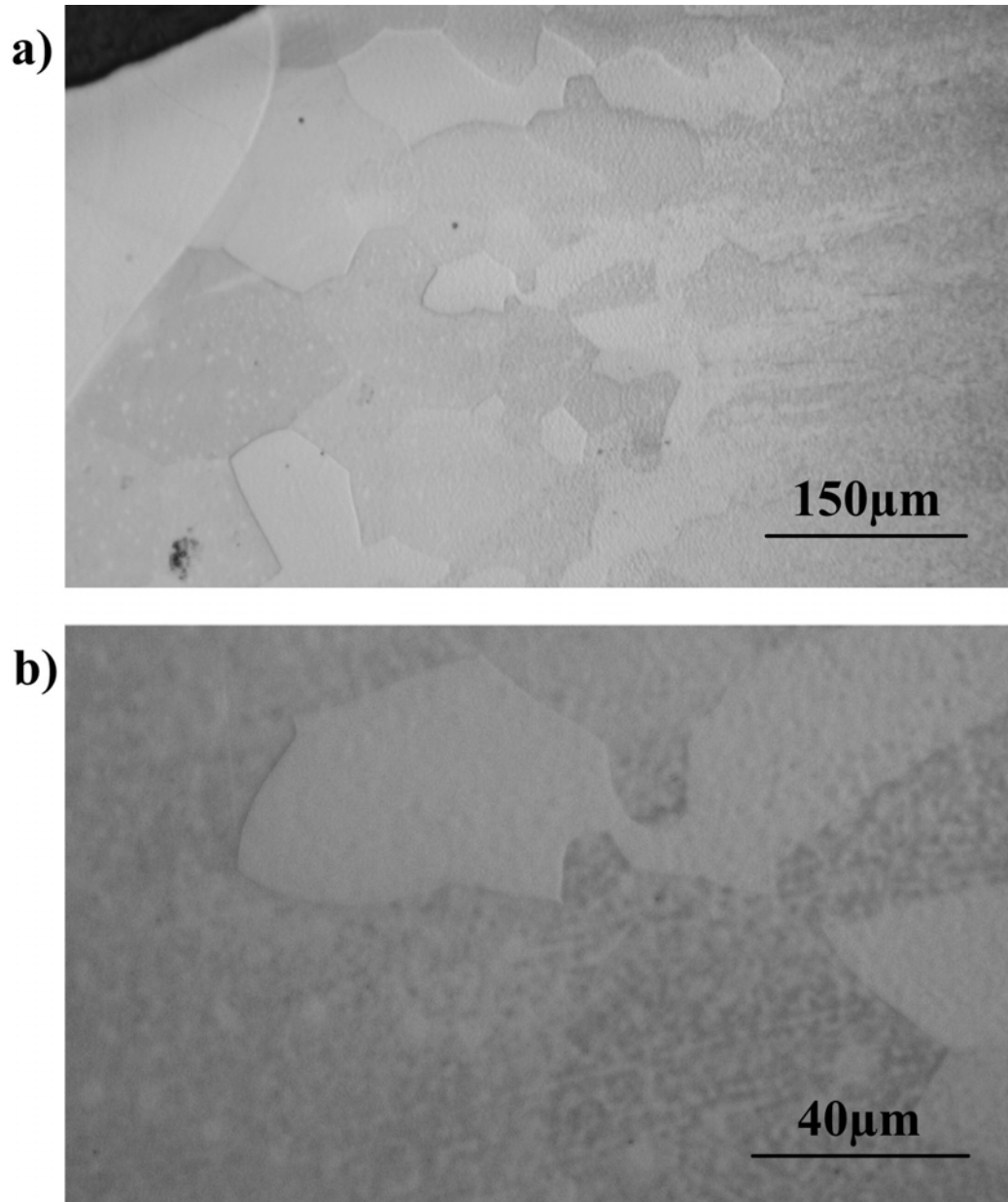
Figure 4-9: Ti5553 HAZ microstructure a) 100x mag b) 400x mag.
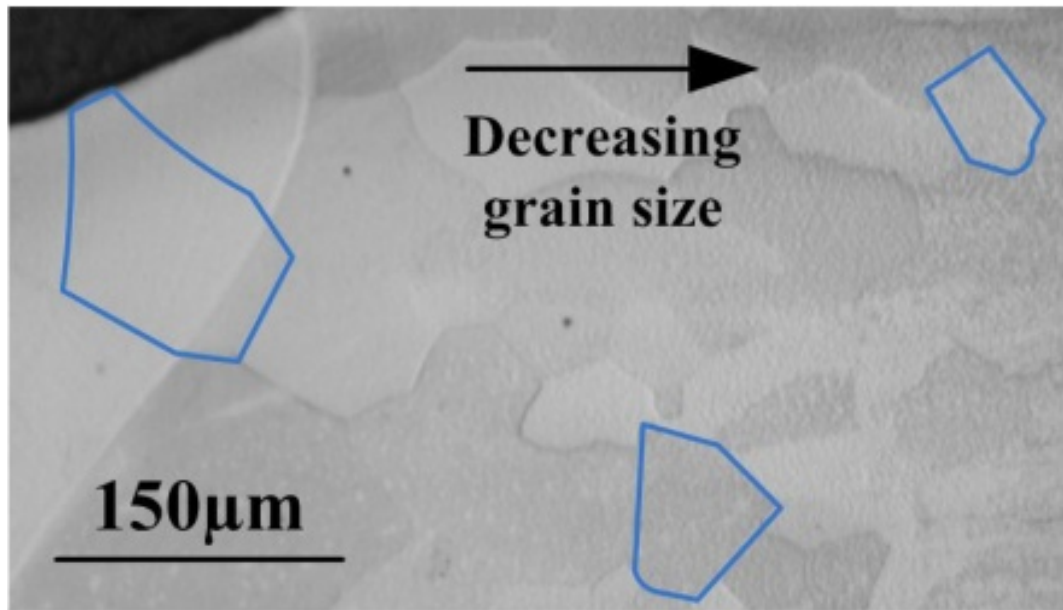
Figure 4-10: Ti5553 HAZ showing former β grain size.

4.2.4 Fusion Zone Microstructure

4.2.4.1 Similar fusion zones
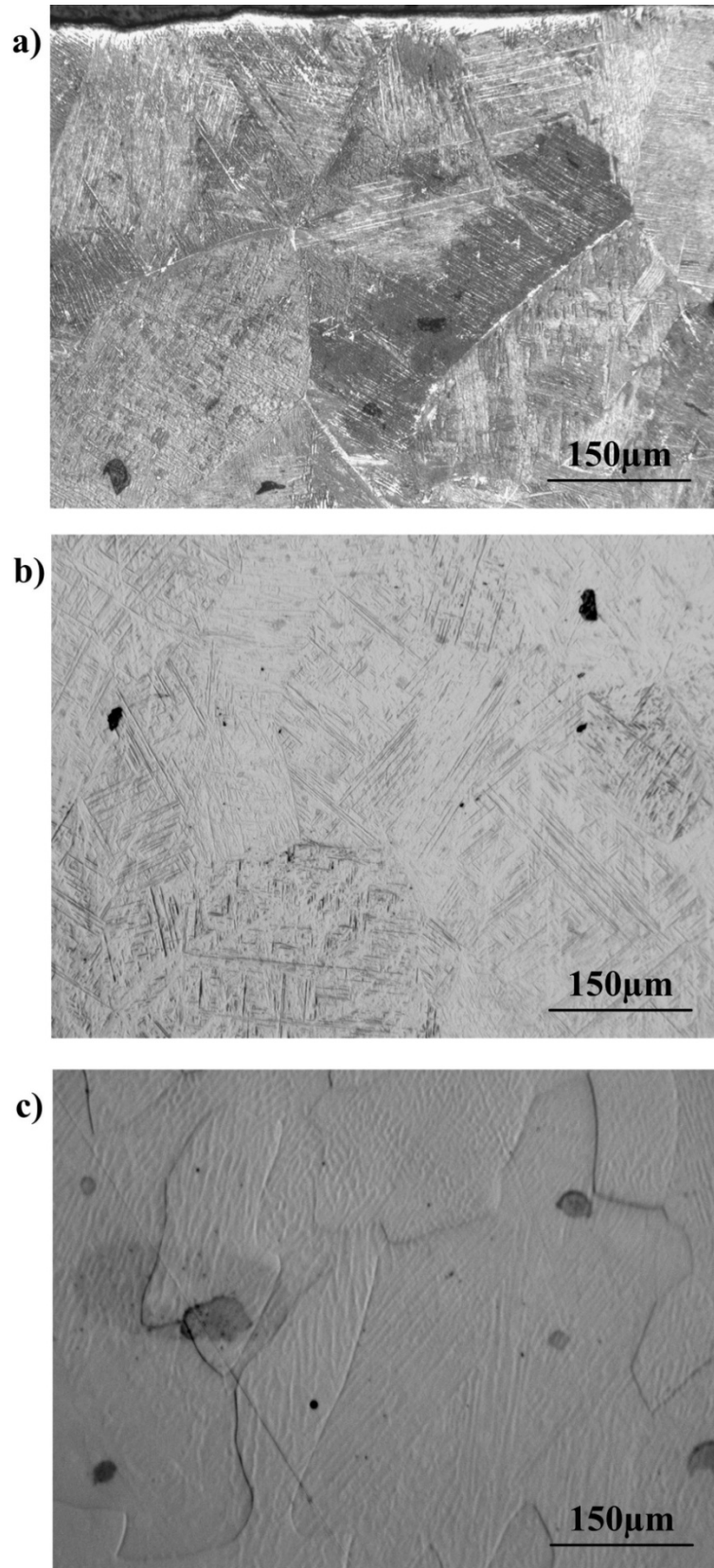
Figure 4-11: Fusion zones of all similar weld combinations at 100x mag, a) CP Ti to CP Ti, b) Ti64 to Ti64, c) Ti5553 to Ti5553

Figure 4-11a) CP Ti to CP Ti – Large acicular transformed β microstructure with retained β grain boundaries. No distinct boundary between the fusion zone and the HAZ.

Figure 4-11b) Ti64 to Ti64 – Large acicular transformed β microstructure with retained β grain boundaries. No distinct boundary between the fusion zone and the HAZ.

Figure 4-11c) Ti5553 to Ti5553 – large columnar β grains that have grown from the grains on the edge of the HAZ. Grains in the Fusion zone have grown off the grains on the boundary of the fusion zone and the HAZ. The surface of the β grains have parallel acicular patterns.

4.2.4.2   Dissimilar fusion zones.

Figure 4-13a) CP Ti to Ti64 – large columnar β grains with transformed β microstructure on the CP Ti side and smaller transformed β microstructure on the Ti64 side. A distinct boundary between the fusion zone and the HAZ. α' phase is evident in the fusion zone on the Ti64 side.

Figure 4-13b) CP Ti to Ti5553 – large columnar β grains, the surface of the β grains have parallel acicular patterns. Possible phase segregation inside the grains, especially on the CP Ti side of the fusion zone. A distinct boundary between the fusion zone and the HAZ.

Figure 4-13c) Ti64 to Ti5553 – large columnar β grains that have grown from the grains on the edge of the HAZ particularly on the Ti5553 side of the fusion zone. A distinct boundary between the fusion zone and the HAZ. The surface of the β grains have parallel acicular patterns. Figure 4-12 shows a large porosity near the fusion zone boundary on the Ti5553 side.
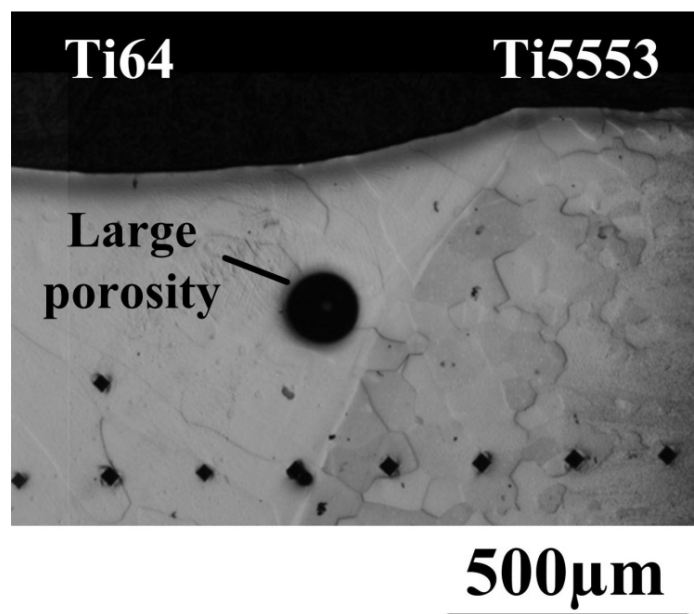
Figure 4-12: Porosity near the Ti64 and Ti5553 Fusion Zone boundary
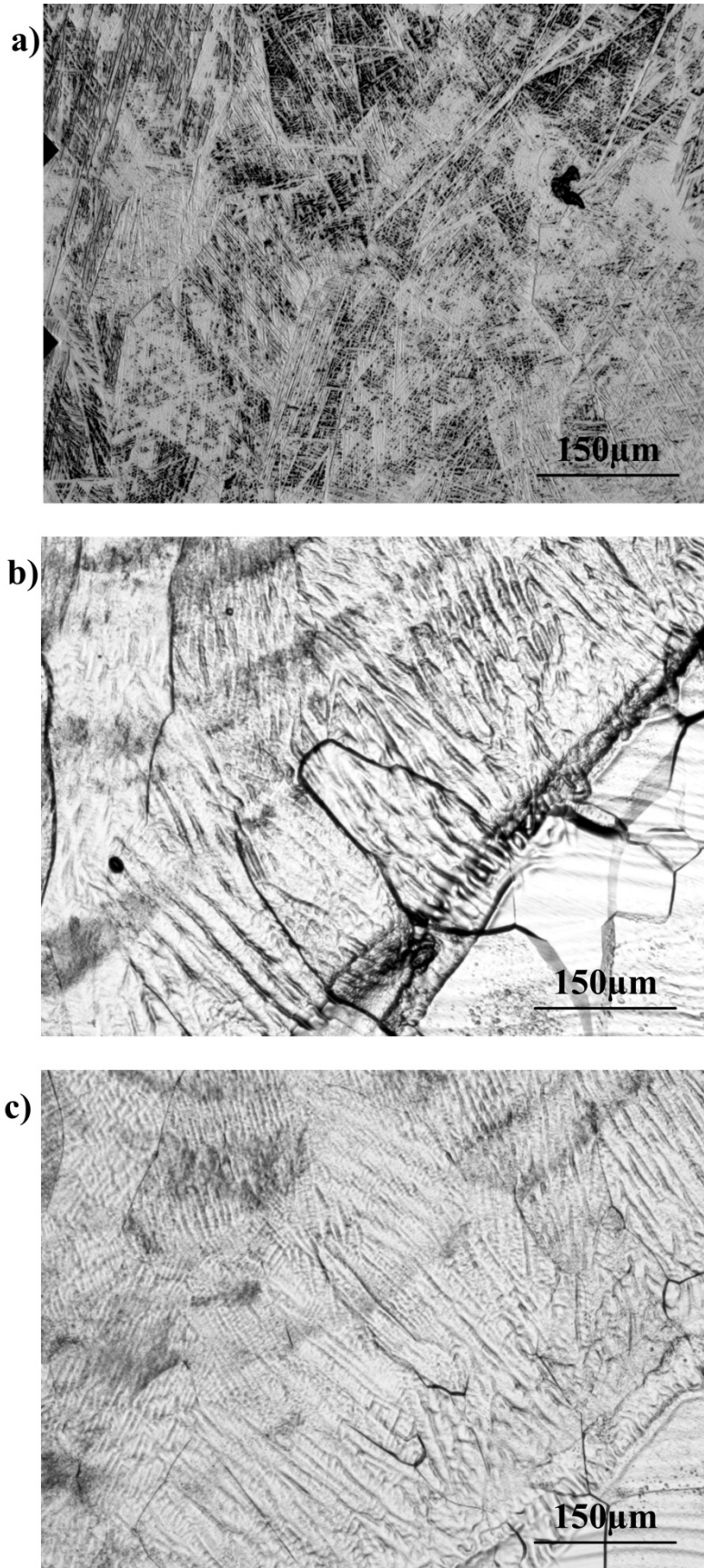
Figure 4-13: Fusion zones of all dissimilar weld combinations at 100x mag, a) CP Ti to Ti64, b) CP Ti to Ti5553, c) Ti64 to Ti5553.

4.3   Hardness Results

4.3.1   Knoop Microhardness

The transverse Knoop microhardness profiles for CP Ti to CP Ti, Ti64 to Ti64 and Ti64 to CP Ti weld combinations are shown in Figure 4-14. The hardness profiles were measured using the method outlined in section 3.3.1. No literature was available to compare to the Knoop microhardness values for any of the weld combinations. Significant variation of the micro-Knoop value was observed in measurement taken in the base materials and the transverse weld profiles.
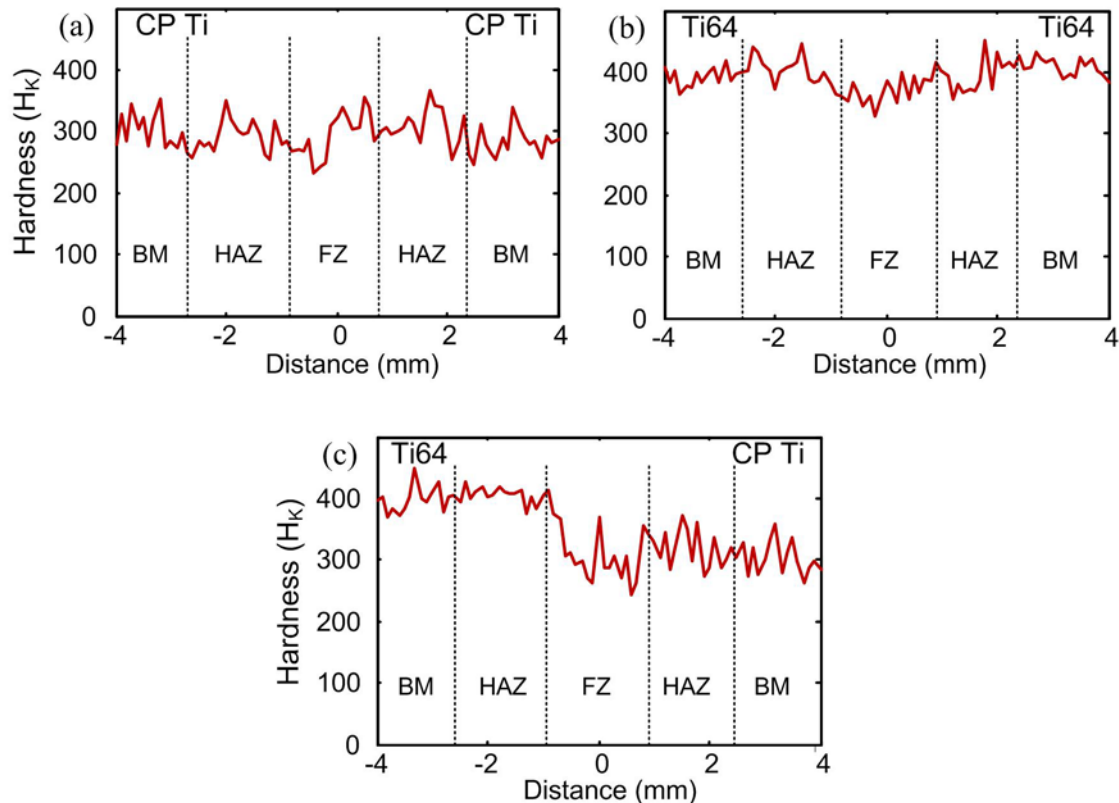
Figure 4-14: Knoop micro-hardness weld profiles, a) CP Ti to CP Ti, b) Ti64 to Ti64 and c) Ti64 to CP Ti.

The CP Ti to CP Ti weld profile (Figure 4-14a) shows the hardness variation of $\pm 70H_K$ in the base metal stays consistent through the base metal, the heat affected and the fusion zones. The general trend of the profile stays consistent around 300 H_K through the base metal, the heat affected and the fusion zones.

The Ti64 to Ti64 weld profile (Figure 4-14b) shows the hardness variation of $\pm 50H_K$ in the base metal stays consistent through the base metal, the heat affected and the fusion zones. The general trend of the profile shows hardness around 400 H_K in the base metal reaching maximums of 450 H_K in the heat affected zones and dropping to 350 H_K closer to the centre of the fusion zone.

The Ti64 to CP Ti weld profile (Figure 4-14b) shows hardness around 400 H_K in the base metal and the heat affected zones of the Ti64. The hardness dropped rapidly on the

Ti64 side of the fusion zone from 400 H_K to around 300 H_K. The hardness profile stays around 300 $H_K \pm 70H_K$ through the CP Ti side of the fusion zone, and the CP Ti heat affected zone and the base metal.

4.3.2 Vickers Microhardness

The transverse Vickers microhardness profiles for all weld combinations are shown in Figure 4-15. The hardness profiles were measured using the method outlined in section 3.3.1. The hardness for similar weld combinations were comparable to those in literature (CP Ti to CP Ti [66], Ti64 to Ti64 [23, 66-68], Ti5553 to Ti5553 [23]). No literature was available to compare to the dissimilar weld combinations.

The Vickers indentations for these profiles have a larger area than the Knoop indentations for the profiles shown in Figure 4-14. These Vickers microhardness profiles demonstrated less variation from point to point and smoother profiles compared to the Knoop profiles. General hardness trends caused by the welding process are easier to see in the Vickers profiles as a result of the smoother profiles.

The mean hardness values measured for the base metals and from a vertical plane through the centre of the fusion zone for each of the weld combinations are given in Table 4-2.

Table 4-2: Mean hardness in the base metal or the centre of the fusion zone

Substrate A	Substrate B	Mean Hardness in the centre of the Fusion Zone ($H_{V\,0.3}$)
CP-Ti	-	250 ± 17
Ti-64	-	332 ± 9
Ti5553	-	333 ± 10
CP-Ti	CP-Ti	255 ± 18
CP-Ti	Ti-64	272 ± 8
CP-Ti	Ti-5553	396 ± 8
Ti-64	Ti-64	332 ± 4
Ti-64	Ti-5553	405 ± 11
Ti-5553	Ti-5553	289 ± 3
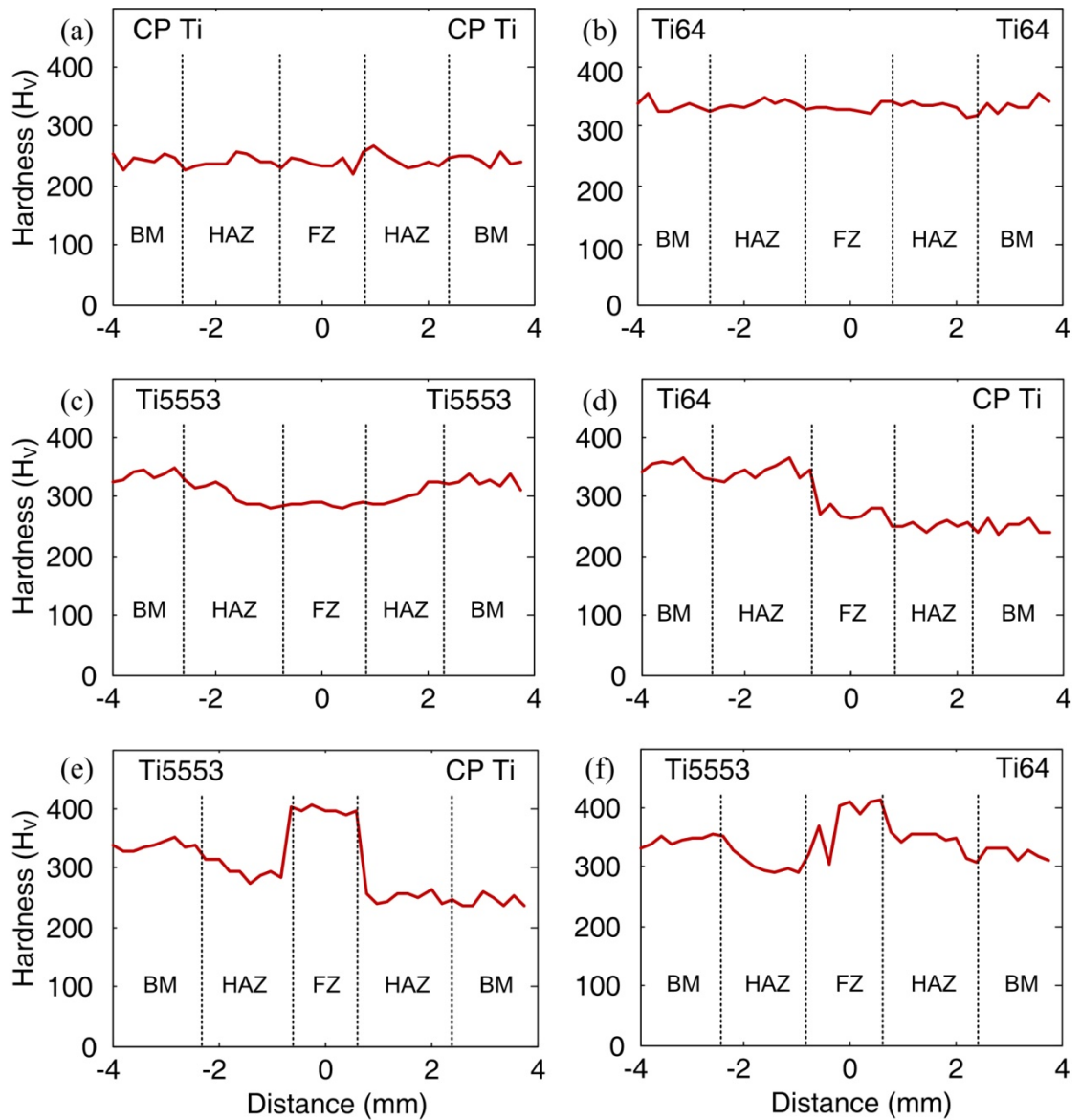
Figure 4-15: Vickers weld hardness profiles, a) CP Ti to CP Ti, b) Ti64 to Ti64 and c) Ti5553 to Ti5553, d) Ti64 ti CP Ti, e) Ti5553 to CP Ti and f) Ti5553 to Ti64.

The CP Ti to CP Ti weld profile (Figure 4-15a) has consistent hardness values around 250 $H_{V\,0.3}$ across the base metal, the heat affected and the fusion zones.

The Ti64 to Ti64 weld profile (Figure 4-15b) has consistent hardness values around 340 $H_{V\,0.3}$ across the whole cross-section. The Vickers hardness profile for this weld combination does not show the increases of hardness in the HAZ or the decrease in the FZ that the Knoop hardness profile demonstrated in Figure 4-14b).

The Ti5553 to Ti5553 weld profile (Figure 4-15c) demonstrated a decrease from the base metal around 335 $H_{V0.3}$, across the HAZ, down to 280 $H_{V0.3}$ in the fusion zone. The fusion zone is the area with the lowest hardness values.

The dissimilar weld profile of Ti64 to CP Ti (Figure 4-15d) has fairly consistent hardness values of around 340 $H_{V\,0.3}$ across both the Ti64 base metal and the HAZ. The hardness drops rapidly on the Ti64 side of the fusion zone to around 260 $H_{V\,0.3}$.

Hardness values around 250 $H_{V\,0.3}$ are consistent across the CP Ti HAZ and the base metal.

The Ti5553 to CP Ti weld (Figure 4-15e) shows a drop in hardness across the Ti5553 HAZ similar to that seen in Figure 4-15c. The fusion zone is significantly harder than both of the base materials with hardness values of around 390 $H_{V\,0.3}$. The CP Ti HAZ and base metal have consistent hardness values around 250 $H_{V\,0.3}$.

The dissimilar weld of Ti5553 to Ti64 (Figure 4-15f) shows a drop in hardness across the Ti5553 HAZ similar to that seen in Figure 4-15c. The fusion zone is significantly harder than both of the base materials with hardness values of around 400 $H_{V\,0.3}$. Consistent hardness values across the Ti64 base metal and HAZ were around 340 $H_{V\,0.3}$.

4.4 Bend Test Results

Bend tests were performed on the top face and root face for CP Ti to CP Ti, CP to Ti64 and Ti64 to Ti64 weld samples. No Ti5553 weld combinations were tested due to insufficient material availability.

All six of the bend samples tested achieved a 180˚ bend without suffered from a catastrophic failure. All welds were located in the centre of the deformed area of the samples. As an elastic spring back effect occurs during the bend deformation of test samples. The final shape of the bent sample is dependent on yield strength of the alloys. The CP Ti substrates showed less spring back than the Ti64 substrates.
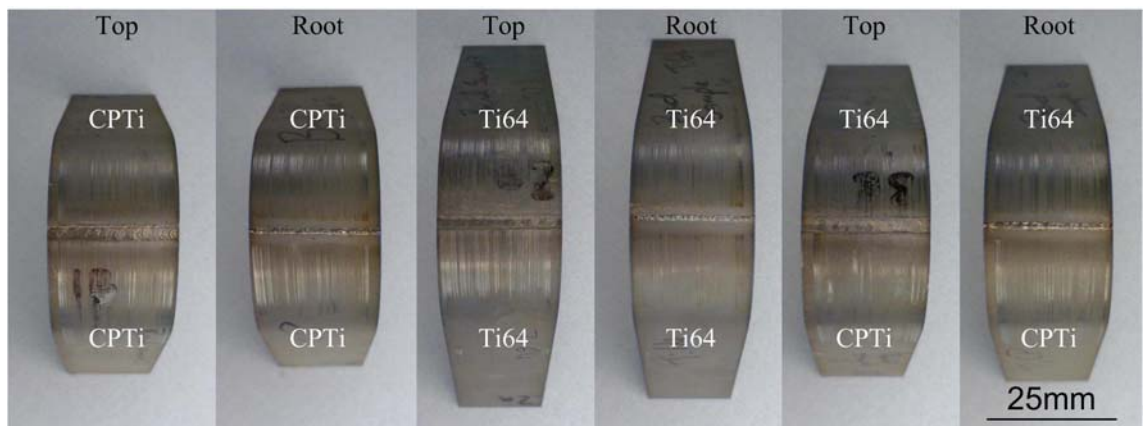
Figure 4-16: 6 Bend samples after bend test .

Initial visual inspection of the 6 deformed samples showed only scratches that came as a result of the moving roller, with no distinct cracks visible.
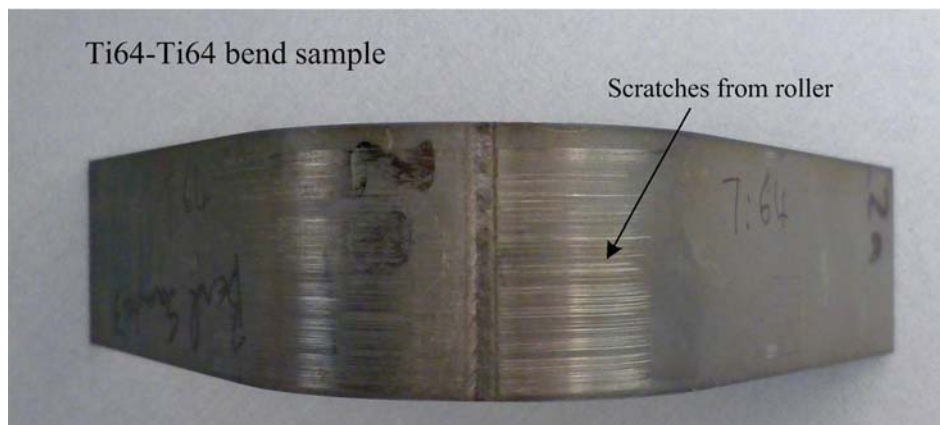
Figure 4-17: Ti64 to Ti64 top surface bend sample showing scratches on the surface from the roller.

Dye penetrant only gave pink spots on the top surface of the Ti6Al4V to Ti6Al4V welded bend sample. The pink spots indicate presence of micro-cracks or surface porosity. All other samples had no pink marks after the dye penetrant process.

Figure 4-18: Dye Penetrant showing the presence of micro-cracks or porosity on the top surface of Ti64 - Ti64 weld bend sample.

4.5   Tensile Results

Stress/strain curves as a result of the extensometer measured tensile samples are shown in Figure 4-19, Figure 4-20 and Figure 4-21. The mechanical properties for all tensile testing for all weld combinations and the base materials are shown in Table 4-3.

4.5.1   Base Metals

All three of the titanium alloy base metals shown in Figure 4-19 have standard ductile fracture tensile curves. Ti5553 and Ti64 base metals both had greater than 12% elongation while CP Ti achieved close to 28%. The tensile properties for the base metal are generally comparable with that found in the literature (CP-Ti [20, 66], Ti-64 [20, 66, 67], Ti-5553 [39, 69]).
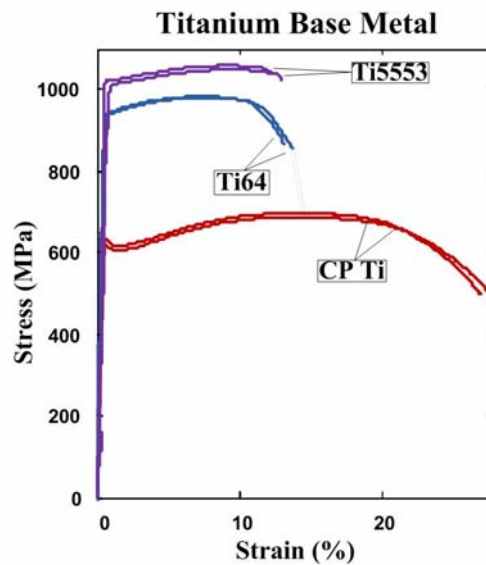
Figure 4-19: Stress/strain curves for three titanium base metals.

4.5.2   Welded Samples

The stress/strain curves of all of the weld substrate combinations are shown in Figure 4-20. The tensile properties for the similar weldments, shown in Figure 4-20a, are generally comparable with that found in the literature(CP-Ti to CP-Ti [66] and Ti-64 to Ti-64 [14, 66-68]), but no publications were available for the tensile strengths of Ti5553 to Ti5553 welds or any of the dissimilar weld combinations shown in Figure 4-20b.
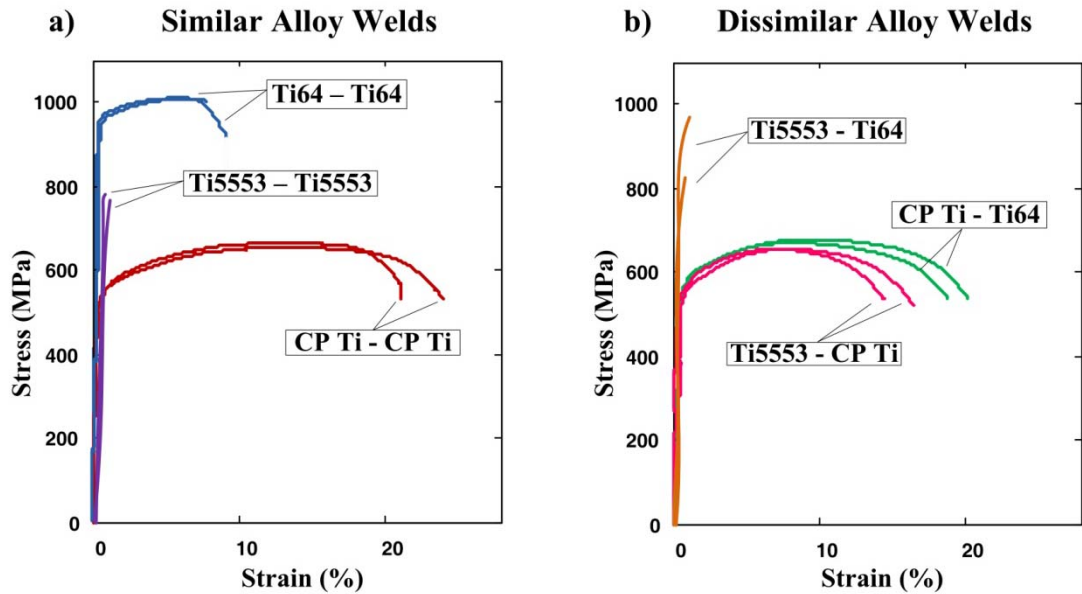
Figure 4-20: Stress/strain curves for a) similar titanium alloy welds and b) dissimilar titanium alloy welds.

All weld combinations with commercially pure titanium as one of the substrates, both similar and dissimilar, failed in the commercially pure titanium base material well away from the fusion and the heat affected zones of the welds. These commercially pure titanium weld combinations all showed similar yield and ultimate tensile strengths with elongation decreasing as the tensile strength of the other substrate increased.

Figure 4-21: Stress/strain curves for low strain Ti5553 weld failures.

The Ti5553 to Ti64 and Ti5553 to Ti5553 weldments, shown in both Figure 4-20 and Figure 4-21, fractured in the fusion zone, after very little elongation and before the yield strength of either base material was achieved. This premature failure indicates an embrittled fusion zone. As Ti5553 to Ti64 and Ti5553 to Ti5553 weldments show such a limited elongation compared to the base metals and other weld combinations, Figure

4-21 shows the stress/strain curves with a reduced elongation scale. The diverging curves for Ti5553 to Ti5553 in Figure 4-21 may be as a result of inaccuracies at low strain in the equipment used. The low strain failure of the Ti5553 to Ti5553 welds specimens was unexpected and the extensometer used was intended for larger strain readings when it was selected as it had large stepped increments.

Ultimate tensile strength, 0.2% yield strength and elongation were calculated for all of the weld combinations and are shown in Table 4-3.

Table 4-3: Tensile properties, and fracture location of base metal and weldments.

Substrate A	Substrate B	$\sigma_{y,0.2}$ (MPa)	σ_{UTS} (MPa)	Elongation % at Fracture	Location of Fracture
CP-Ti	-	630 ± 4	693 ± 7	27.4 ± 0.6	-
Ti-64	-	941 ± 1	983 ± 1	13.1 ± 0.5	-
Ti5553	-	1028 ± 8	1053 ± 7	12.7 ± 0.7	-
CP-Ti	CP-Ti	528 ± 5	660 ± 8	22.5 ± 2.1	CP-Ti BM
CP-Ti	Ti-64	547 ± 11	673 ± 6	19.3 ± 0.9	CP-Ti BM
CP-Ti	Ti-5553	566 ± 32	655 ± 1	15.5 ± 1.5	CP-Ti BM
Ti-64	Ti-64	959 ± 3	1010 ± 2	8.5 ± 0.9	Fusion Zone
Ti-64	Ti-5553	-	899 ± 103	0.9 ± 0.4	Fusion Zone
Ti-5553	Ti-5553	-	778 ± 16	0.8 ± 0.4	Fusion Zone

4.5.3 Aramis System - Strain Measurements

The Aramis strain capture system was used at the Department of Materials Science and Engineering, Lehigh University, Bethlehem – Pennsylvania, USA. An example of the strain capture results for a Ti64 – Ti5553 tensile sample is shown in Figure 4-22.
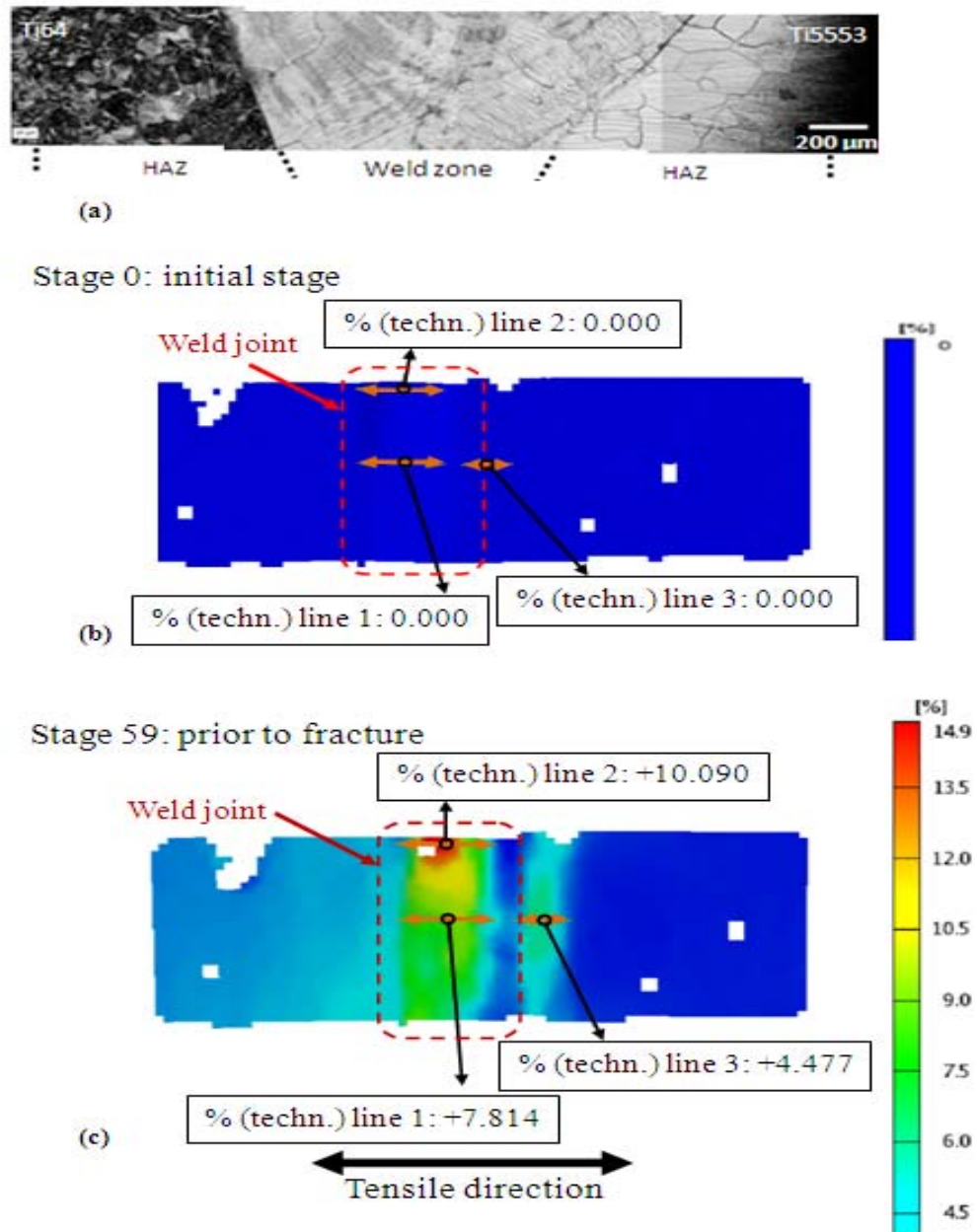
Figure 4-22: (a) Ti64 to Ti5553 weld profile, (b) Aramis sample image prior to being pulled, (c) Aramis sample image prior to fracture indicating local strain of 10% in the weld zone. (0)

Figure 4-22a) shows the weld cross section for the Ti64 to Ti5553 weld. Figure 4-22b) is the digital image of the strain in the tensile sample before pulling commenced. Figure 4-22c) shows the digital image of the strain in the tensile sample before fracture occurred. Highly localised strain upwards of 10% is visible on the edge of the tensile sample in the fusion zone.

4.6   SEM of Fracture Surfaces

The location of fracture and the type of fracture is given in Table 4-4 for all of the weld combinations and the base metals.

Table 4-4: Tensile failure location and failure mode

Substrate A	Substrate B	Location of Fracture	Fracture Mode
CP-Ti	-	-	Ductile
Ti-64	-	-	Ductile
Ti5553	-	-	Ductile
CP-Ti	CP-Ti	CP-Ti Base Metal	Ductile
CP-Ti	Ti-64	CP-Ti Base Metal	Ductile
CP-Ti	Ti-5553	CP-Ti Base Metal	Ductile
Ti-64	Ti-64	Fusion Zone	Ductile + Brittle
Ti-64	Ti-5553	Fusion Zone	Ductile + Brittle
Ti-5553	Ti-5553	Fusion Zone	Ductile + Brittle

4.6.1 Base Metal Fracture Surfaces

Figure 4-23 shows a typical fracture surface for the CP Ti base metal. It has equiaxed dimples over the fracture surface that is consistent with a ductile failure.
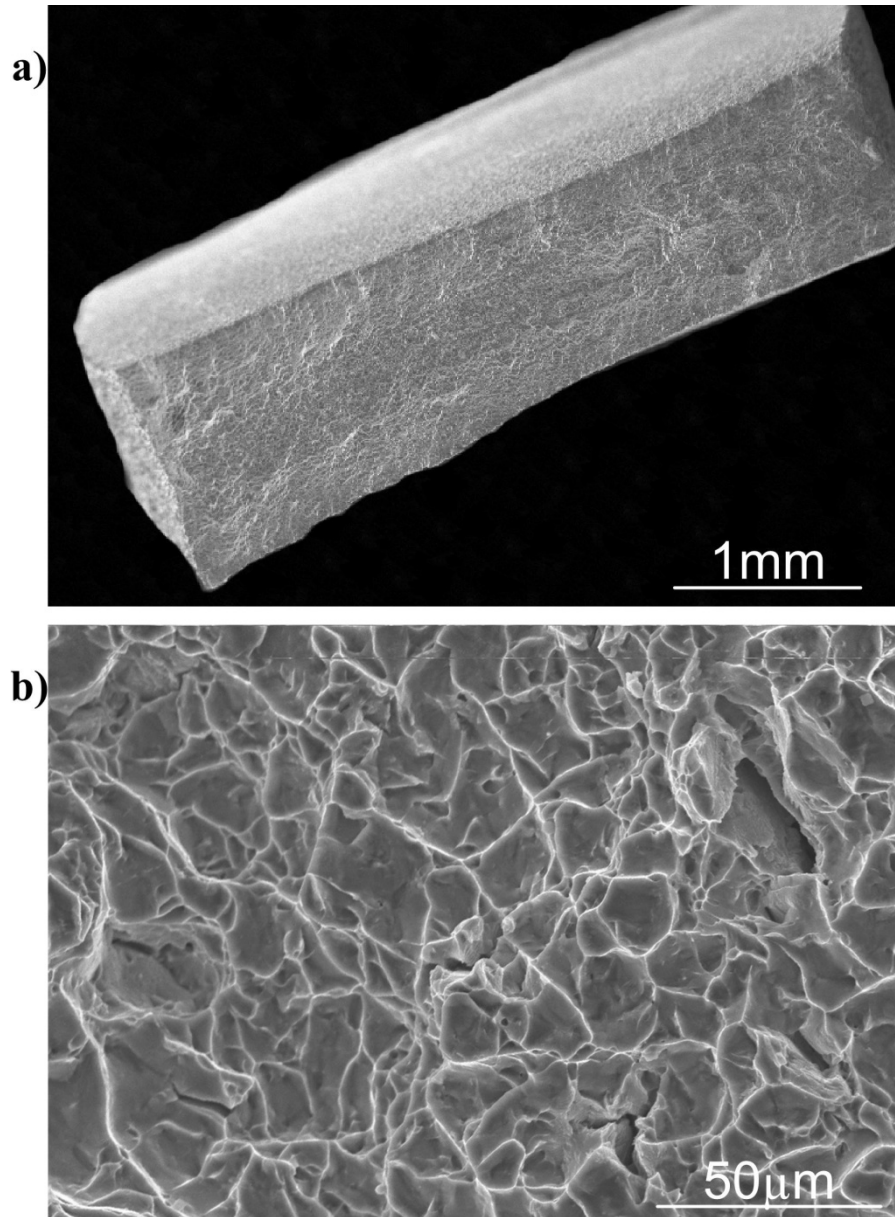
Figure 4-23: SEM image of CP Ti base metal fracture surface a) overview, b) high magnification.

Figure 4-24 shows a typical fracture surface for Ti64. The surface has equiaxed dimples over the fracture surface consistent with a ductile failure. The dimples were smaller than those observed on the CP Ti.
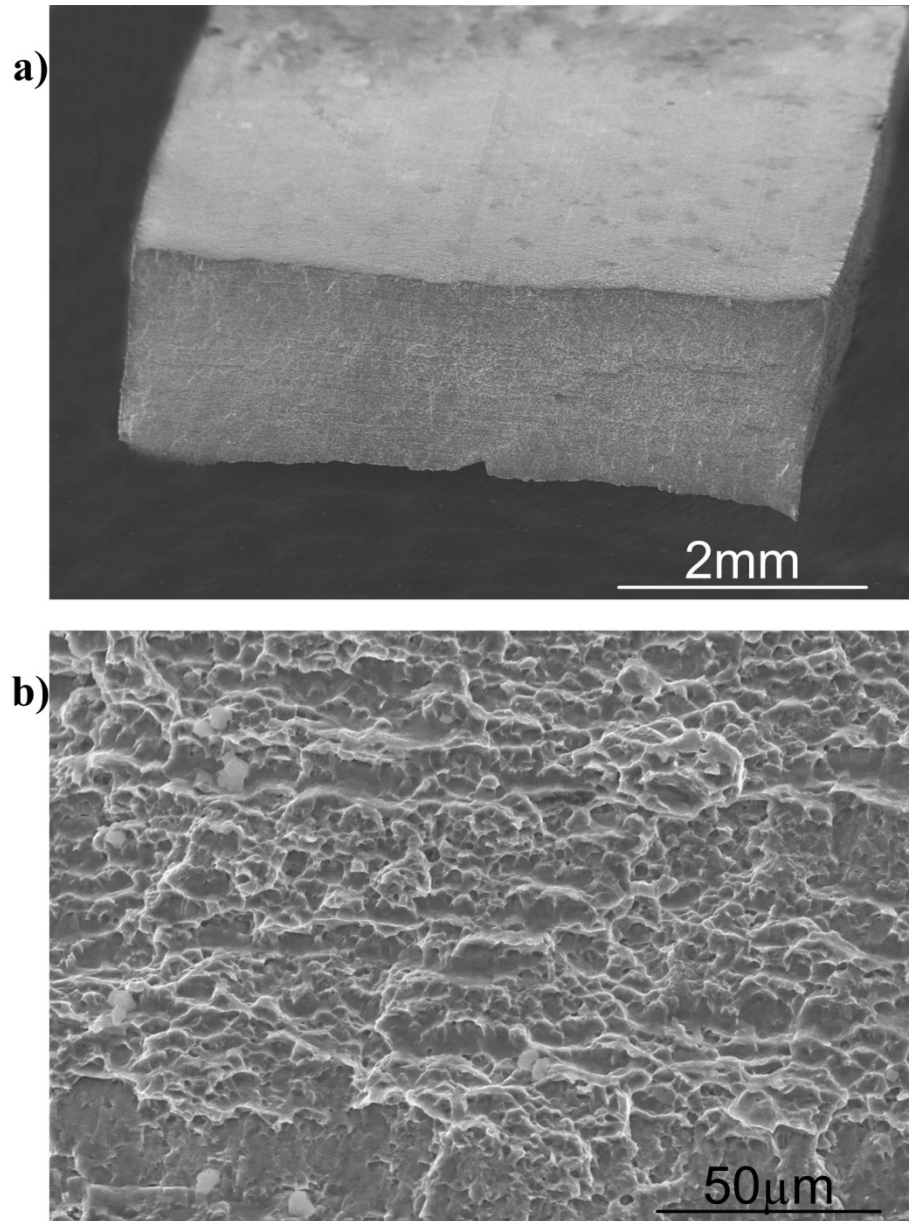
Figure 4-24: SEM image of Ti64 base metal fracture surface a) overview, b) high magnification.

Ti5553 base metal showed small equiaxed dimples on the fracture surfaces. Small ridges on the fracture surface also have dimple patterns on them. The dimples were smaller than those found in both commercially pure titanium and Ti64 fracture surfaces.
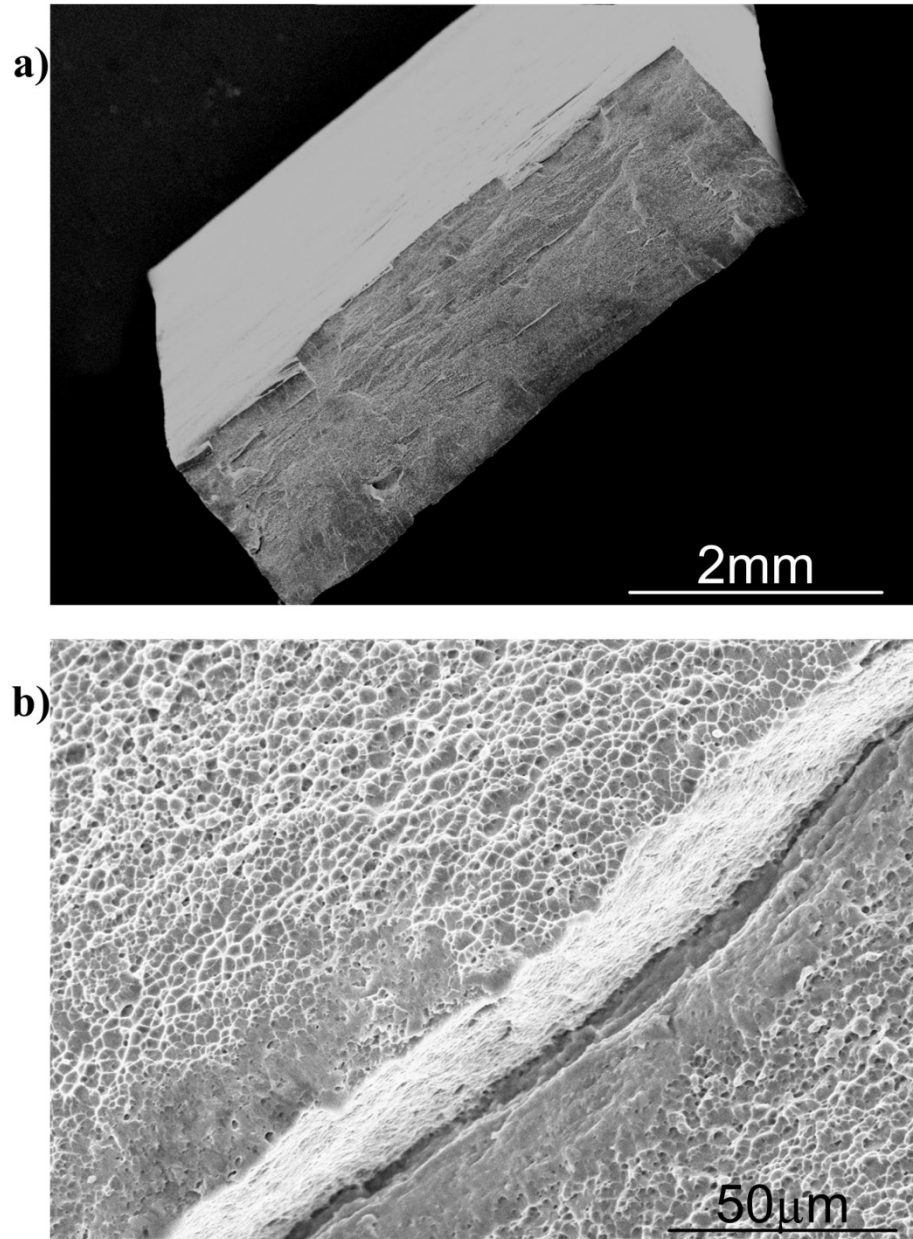
Figure 4-25: SEM image of Ti5553 base metal fracture surface a) overview, b) high magnification.

4.6.2 Welded Fracture Surfaces

All weld samples that had CP Ti failed in the CP Ti base metal. Figure 4-26 shows a characteristic fracture surface from a welded sample. All of these fracture surfaces showed similar equiaxed dimples over the whole fracture surface.
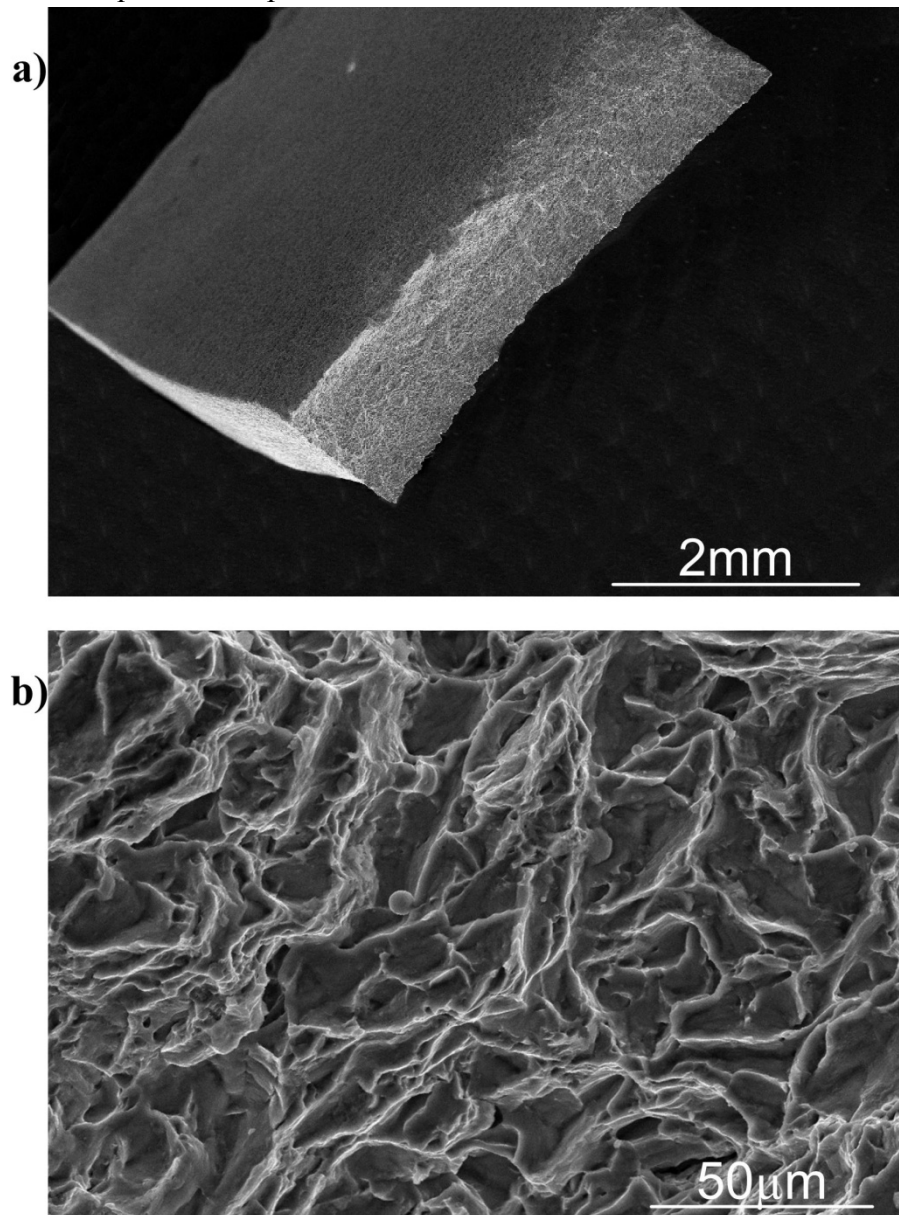
Figure 4-26: SEM image of characteristic CP Ti base metal fracture from welded sample a) overview, b) high magnification.

The fracture surface for the Ti64 to Ti64 weld combination is shown in Figure 4-27. Different areas of the fracture surface showed different types of failure. Figure 4-27b is close to the centre of the fracture surface shows transgranular failure usually associated with brittle fracture. The cross hatched pattern of a transformed β grain can be seen in the fracture pattern. Figure 4-27c is from an area near the bottom of fracture surface. This area has equiaxed dimples indicating ductile fracture in this area.
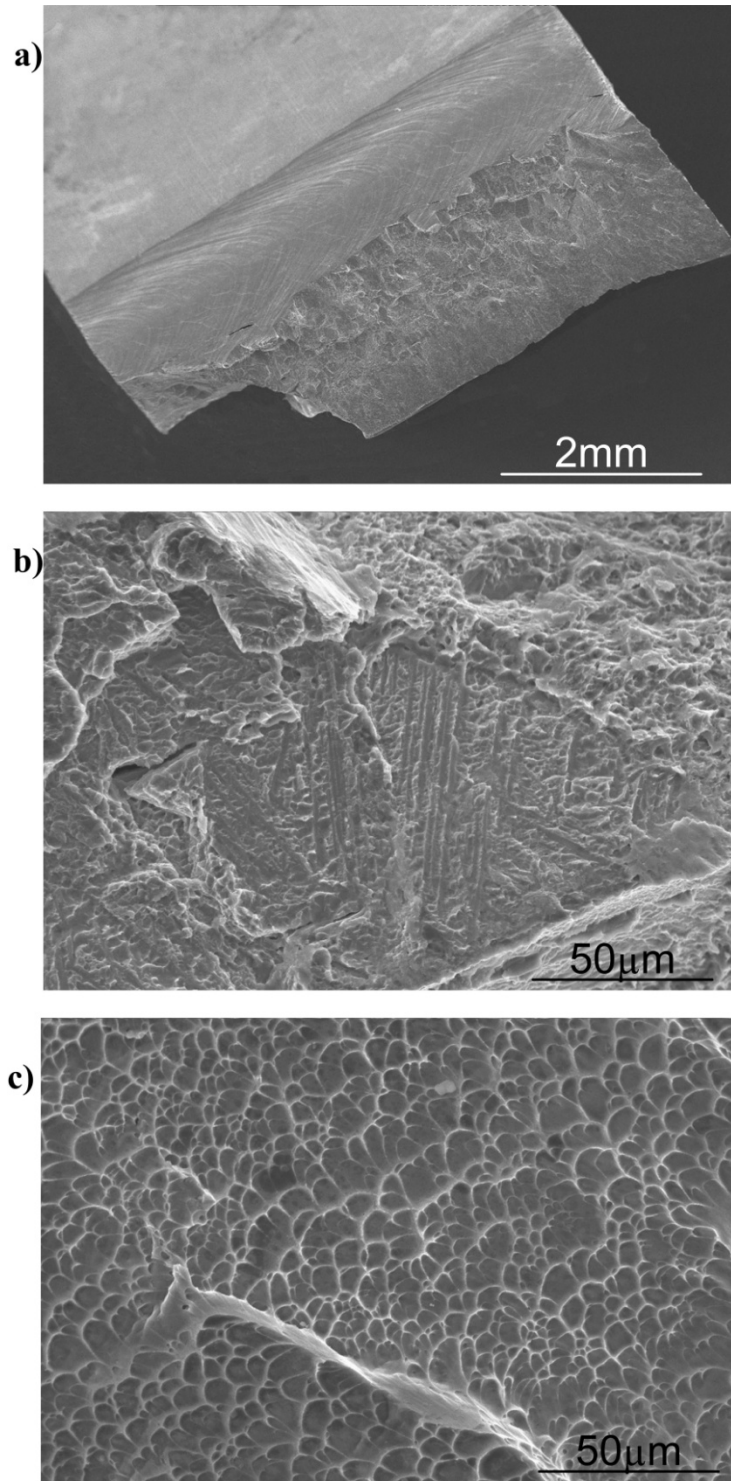
Figure 4-27: SEM image of Ti64 –Ti64 weld sample fracture surface a) overview, b) intergranular failure, c) equiaxed dimples.

The fracture surface for the Ti5553 to Ti5553 weld combination is shown in Figure 4-28. Different areas of the fracture surface showed different types of failure. Figure 4-28b is close to the top of the fracture surface and shows transgranular failure usually associated with brittle fracture. The large smooth surface of the β grains can be seen in the fracture pattern. Figure 4-28c is from an area in between some of the large β grains. This area has equiaxed dimples indicating ductile fracture in this area.
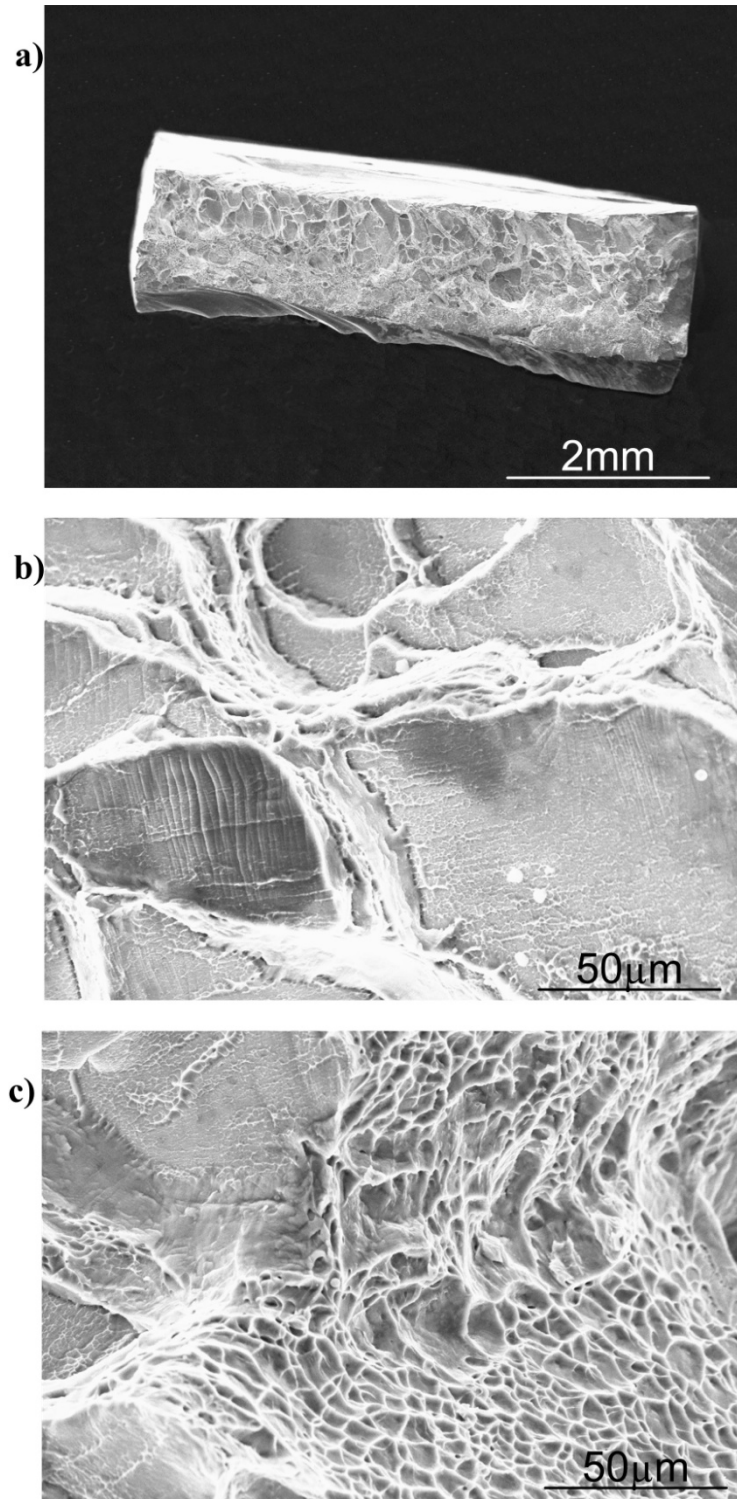
Figure 4-28: SEM image of Ti5553 – Ti5553 weld sample fracture surface a) overview, b) intergranular failure, c) equiaxed Dimples.

The fracture surface for the Ti64 to Ti5553 weld combination is shown in Figure 4-29. Most of the fracture surface shows transgranular failure usually associated with brittle fracture. Figure 4-29c shows large smooth surface of the β grains and small areas of equiaxed dimples in between them.
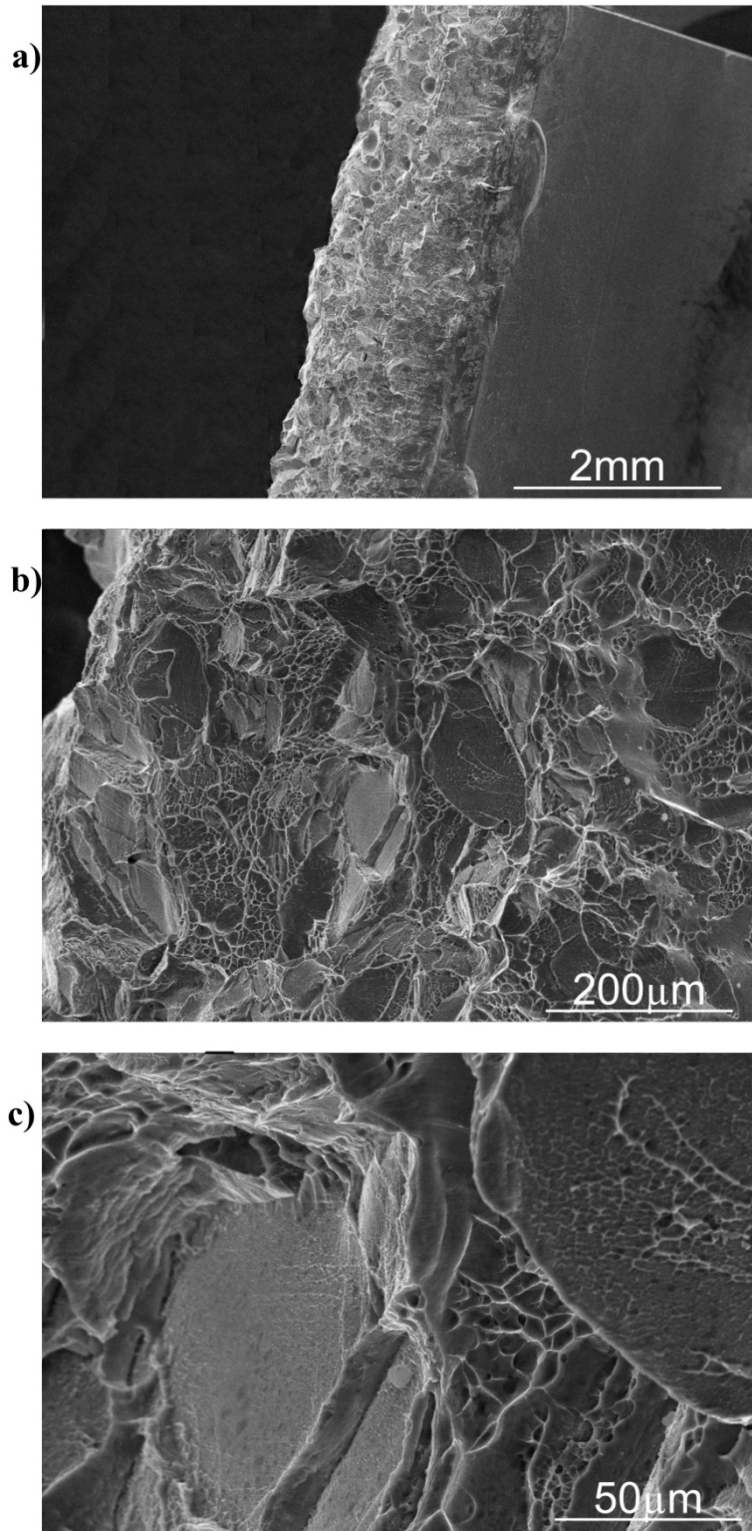
Figure 4-29: SEM image of Ti64 –Ti5553 weld sample fracture surface a) overview, b) medium magnification, c) high magnification

4.7   EPMA

The composition gradients across the welds were measured using electron microprobe microanalysis (EPMA). These were performed using a line scan on weld cross sections from base metal to fusion zone to base metal. An example of similar composition is given for Ti5553 to Ti5553 (Figure 4-30) and Ti64 to Ti5553 (Figure 4-32). The Mo_{eq} for the EPMA line scans were plotted and are shown for Ti5553 to Ti5553 in Figure 4-31 and for Ti64 to Ti5553 in Figure 4-33.
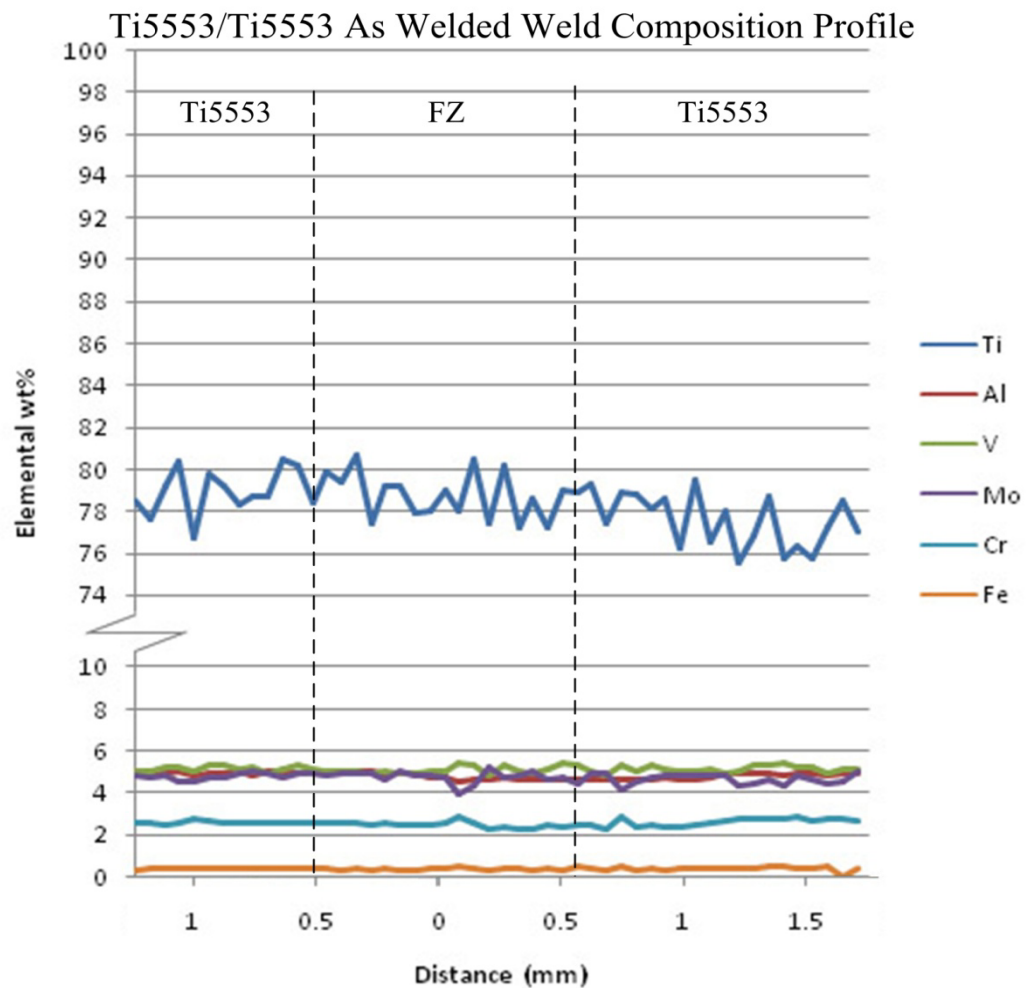
Figure 4-30: EPMA compositional profile of similar Ti5553 to Ti5553 weld.
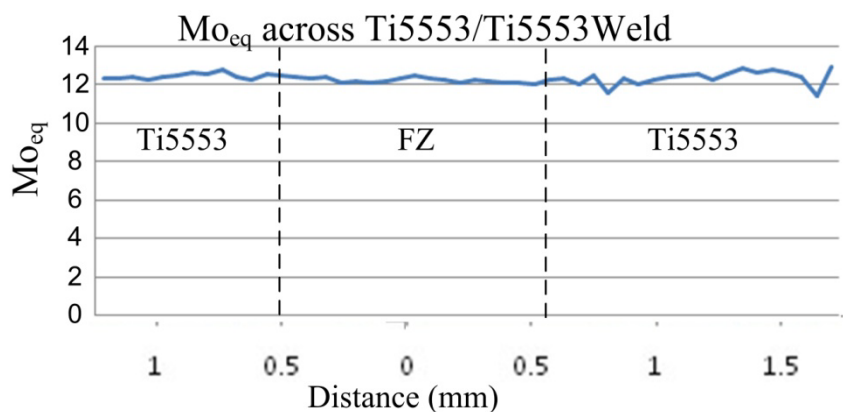
Figure 4-31: Mo_{eq} across similar Ti5553/Ti5553 weld.
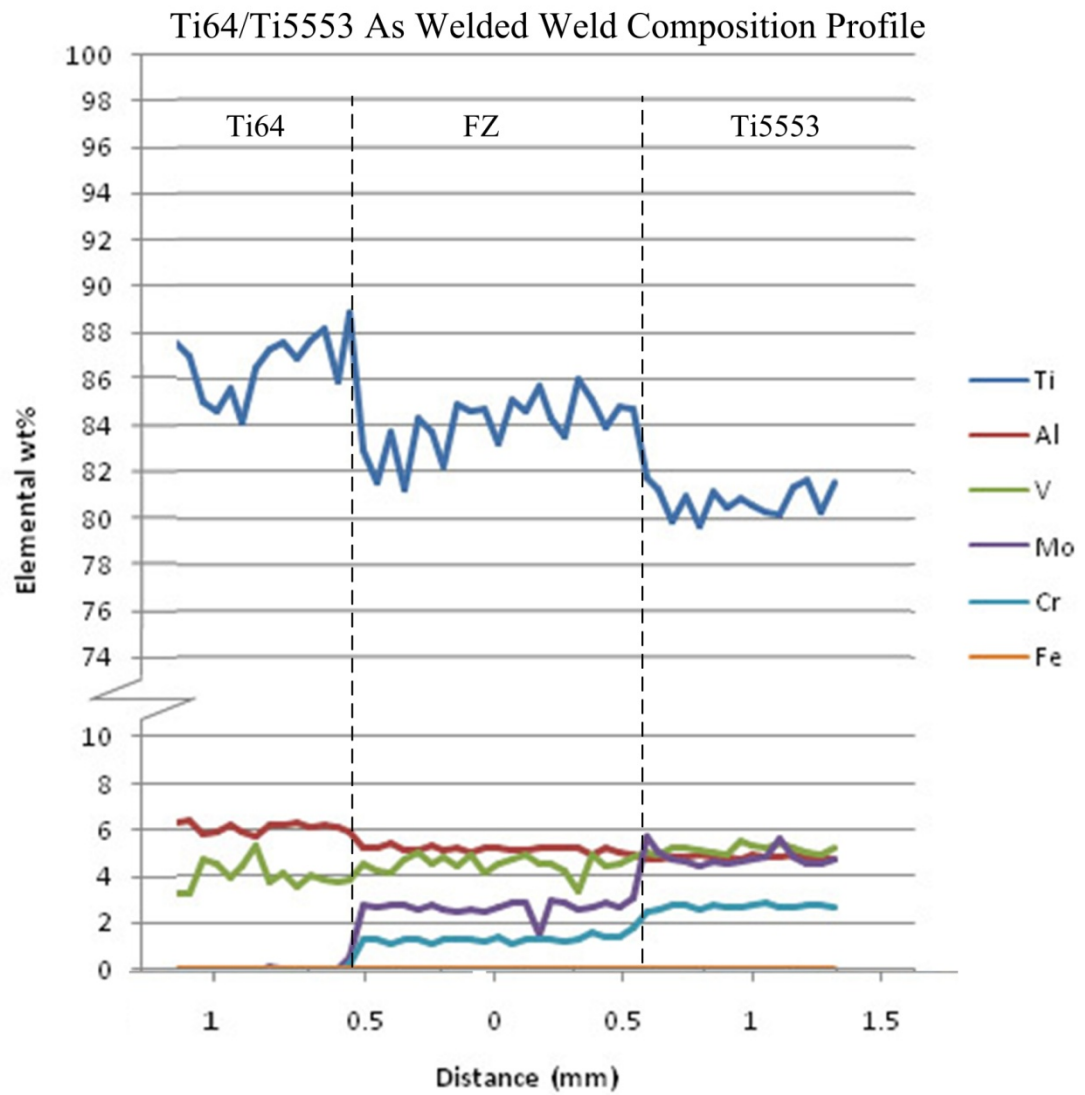
Figure 4-32: EPMA compositional profile of dissimilar Ti64 to Ti5553 weld.
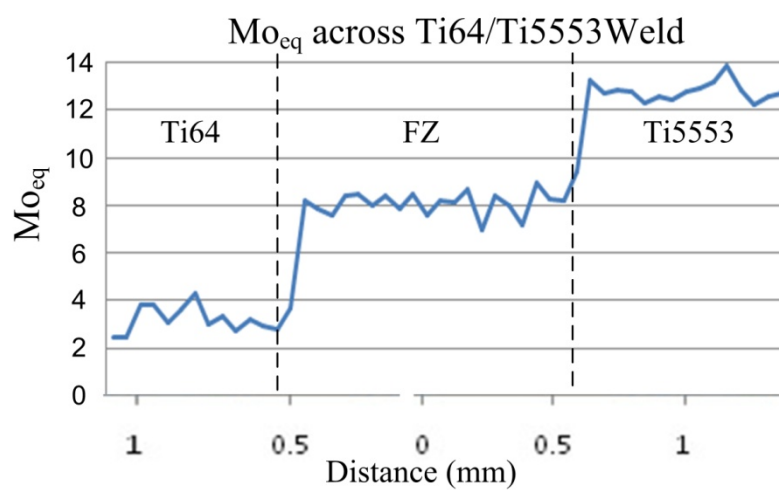
Figure 4-33: *Moeq* across dissimilar Ti64/Ti5553 weld.

5.0 Discussion

5.1 Microstructures

5.1.1. Titanium Base Alloys

All base alloys used in these welding trials had initial microstructures that were consistent with the microstructures expected from literature.

The commercially pure titanium (Figure 4-1) had equiaxed 100% α phase grains. This microstructure is consistent with an annealed α phase commercially pure titanium.

The Ti6Al4V alloy (Figure 4-2) showed slightly elongated equal sized α grains with β phase collected at the grain boundaries. This structure is consistent with an annealed and rolled α+β alloy.

The condition of Ti5553 base metal (Figure 4-3a) used in these trials looks similar to the Ti5553 (Figure 5-1a) use in the paper by Jones [47]. Jones's Ti5553 had been subjected to a large number of prior processing steps which including hot forging in both the β and α+β zones. These steps resulted in a fully homogenous material (Figure 5-1a). A back scattered electron image (BSEI) of the microstructure (Figure 5-1b) showed an even distribution of small globular α particles within a retained β matrix. The α volume fraction was 10±1% [47].
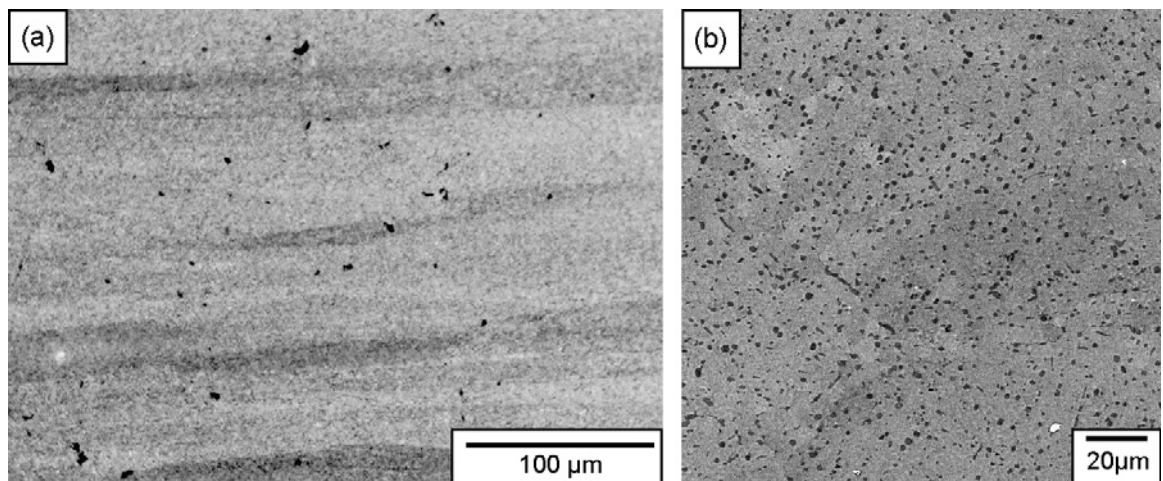
Figure 5-1: a) Light micrograph of Ti5553 as received macrostructure and b) BSEI image of Ti5553 as received microstructure [47].

The α volume fraction for the Ti5553 used in this study can only be determined through future BSEI, as the phases are not distinguishable under standard visible light microscopy and any aging variations from the Jones study will result in a different α volume fraction.

5.1.2. Similar Titanium Alloy Welds

5.1.2.1. CP Ti to CP Ti Welds

The similar electron beam welds of commercially pure titanium produced transformed β grains with cross hatched acicular Widmanstätten structure in both the HAZ and fusion zones.

The cross hatched acicular Widmanstätten structure microstructure is typical for α phase alloys that have been rapidly cooled from above the β transus. This structure could either be completely α phase or α phase + α' martensite as the microstructure for the two look the same.

Hardness profiles show no significant increases in the fusion or HAZ which indicates that the presence of martensite is unlikely and the microstructure is likely to be completely α phase.

5.1.2.2. Ti64 to Ti64 Welds

The electron beam welding of similar Ti6Al4V produced transformed β grains with cross hatched acicular Widmanstätten structure. This microstructure is typical for α+β alloys that have been rapidly cooled from above the β transus. This structure could either be acicular α+β phase or α'+β phase as the microstructures look very similar. The cooling rate will be the controlling factor as to which phases are present.

Vickers hardness profiles show no significant increases in the fusion or HAZ which indicates that martensites are unlikely to be present.

The transformed β microstructure occurred in both the fusion zone and the HAZ with the initial β grain size larger the closer to the centre of the weld. The variation in initial β grain size can be seen in the Ti64 to Ti64 weld profile in Figure 4-4b.

5.1.2.3. Ti5553 to Ti5553 Welds

When the similar Ti5553 was electron beam welded together the microstructure produced was large columnar β grains.

This is a typical microstructure for a rapidly cooled metastable β phase alloy from above the β transus. The large columnar β grains microstructure will be almost 100% β phase but could also have the presence of ω phase which is undetectable with light microscopes.

The β phase large grain microstructure occurred in both the fusion zone and the HAZ with the fusion zone β grains growing from the HAZ β located next to the weld pool. The new large β grains have a parallel acicular pattern on the surface and can be seen in the Ti5553 to Ti5553 weld profile in Figure 4-4c.

Hardness in the fusion zone was clearly lower than in the base metal. The cause of this was unclear, but one explaintion may be that the dissolution of the α phase could be

responsible. Martensite (α' phase) could not form due to the high solute of this alloy i.e. beyond what is required for martensitic transformation.

5.1.3. Dissimilar Titanium Alloy Welds

5.1.3.1. CP Ti to Ti64 Welds

The dissimilar weld between Ti64 and CP Ti (Figure 4-4d) produced transformed β microstructures in the two different HAZ zones and the fusion zone.

The HAZ of the two substrates have produced similar transformed β microstructure to the HAZ microstructures in their respective similar welds.

The fusion zone demonstrates similar cross hatched acicular Widmanstätten structure microstructure which makes sense as the fusion zone composition should be half way between the two alloys, and both similar welds for these substrates had transformed β microstructure. The structures in the fusion zone could include acicular α phase, acicular α+β phase or α'+β phase, all of which have similar looking microstructures.

Vickers hardness profiles show no significant increases in the fusion zone or HAZ. Any significant increase would indicate that martensite is present as part of the post weld microstructure.

The grains in the fusion zone seem to be larger on the CP Ti side of the fusion zone. The larger grain growth on the CP Ti could be as a result of preferential melting or freezing of one of the substrates. This may occur as the result of a beam misalignment. Variation in the composition from incomplete mixing of the weld pool may contribute to the microstructural variation though the EPMA results suggest consistent mixing in the fusion zones of the welds.

The transformed β microstructure occurred in both the fusion zone and the HAZ with the initial β grain size larger the closer to the centre of the weld it is located. The variation in initial β grain size can be seen in the CP Ti to Ti64 weld profile in Figure 4-4d.

5.1.3.2. CP Ti to Ti5553 Welds

The dissimilar weld between CP Ti and Ti5553 (Figure 4-4e) produced columnar β phase microstructures in the fusion zone. This was unexpected as the Mo_{eq} for the estimated fusion zone composition was well under 10 and the transformed β structure had been expected.

The columnar β phase fusion zone is shown in the Vickers hardness profiles to be harder than both the base metal substrates. This may be associated with the formation of martensite (α' phase) as a result of combination of the rich solutes from Ti5553 with lean solutes in the CP Ti.

The surface of the β grains have parallel acicular patterns in the fusion zone. These patterns may indicate the formation of finely dispersed ω phase, α' martensite or α phase.

HAZ of the two substrates have produced similar microstructure to the HAZ microstructures in their respective similar welds. The transformed β microstructure only occurred in the CP Ti HAZ with the initial β grain size largest on the fusion zone boundary. The columnar β grains of the fusion zone seems to grow out of the Ti5553 HAZ. The size of the β grains decreases further from the fusion zone.

5.1.3.3. Ti64 to Ti5553 Welds

The weld between the dissimilar Ti64 and Ti5553 (Figure 4-4f) produced large columnar β grain microstructures. The surface of the β grains have parallel acicular patterns in the fusion zone. This was unexpected as the Mo_{eq} for the estimated fusion zone composition was under 10 and the transformed β structure had been expected.

The columnar β phase fusion zone is shown in the Vickers hardness profiles to be harder than both the base metal substrates. Martensite (α' phase) might have formed in the fusion zone.

HAZ of the two substrates have produced similar microstructure to the HAZ microstructures in their respective similar welds. The transformed β microstructure only occurred in the Ti64 HAZ with the initial β grain size largest on the fusion zone boundary. The columnar β grains of the fusion zone seems to grow out of the Ti5553 HAZ. The size of the β grains decreases further from the fusion zone

A large porosity defect is visible on the Ti5553 side of the fusion zone. The fusion zone may consist of finely dispersed ω phase, α' martensite or α phase.

.

5.2   Mechanical Properties

5.2.1. Hardness

The Vickers transverse hardness profiles of the similarly welded Ti64 (Figure 4-15b) and CP Ti (Figure 4-15a) had no significant changes in the hardness for the fusion and the heat affected zones compared to the original base metal. This means any α' martensite or other precipitates that may have formed, as a result of rapid cooling from above the β transus during the welding process, did not increase the hardness of the material.

The Ti5553 similar weld (Figure 4-15c) shows that the Vickers hardness decreased in the HAZ, and further still in the fusion zone. This can be explained through the removal of the α phase precipitates that had been strengthening the base metal microstructure. When the Ti5553 was heated above the β transus, any α phase, that had previously precipitated out through heat treatment, was transformed into β phase. Upon cooling back below the β transus the β phase is retained and the strengthening the α phase had provided the β matrix is removed, and the hardness is decreased.

The Ti64 to CP Ti Vickers hardness profile (Figure 4-15d) shows a simple transition from the harder Ti64 alloy, to the softer weld pool and CP Ti alloy. The drop in hardness happens very sharply on the Ti64 HAZ / fusion zone boundary. The fusion zone hardness was comparable to the softer CP Ti HAZ and CP Ti base metal.

The Vickers hardness profiles of the dissimilar welds between Ti5553 and CP Ti (Figure 4-15e) and Ti5553 and Ti64 (Figure 4-15f) are the most interesting and surprising results. Like in the Ti5553 similar weld (Figure 4-15c) the hardness in the Ti5553 HAZ decreases, but in the dissimilar fusion zone the hardness increases to above that of any of the base materials. This hardening may be as a result of the formation of ω phase in the β grains, or the micro-separation of alloying elements, or the precipitation of fine α grains. The β grain structure seems to stay intact, so identification of the cause of the hardening will require further study with TEM or BSEI to identify what phases and elements are present and in what quantities.

5.2.2. Bending

Though the bend elongation at 2.3% is significantly lower than the expected tensile elongation, it does offer the opportunity to ensure that the fusion zone specifically does undergo elongation. All of the samples were able to perform this mild bend without any catastrophic failure. Once dye penetrant was used on the bend samples, only the Ti64 to Ti64 top face bend sample showed pink dots indicating micro cracks or surface porosities. This indicates that this particular weld might require post weld heat treatment if it is going to be subjected to bending. A potential reason for this failure is the large grains that have formed on the top part of the fusion zone in the weld. Longer elongation achieved in tensile samples may be as a result of elongation happening in base materials or the HAZ rather than the fusion zone where the final failure occurs.

5.2.3. Tensile

5.2.3.1 Similar Titanium Alloy Welds

The CP Ti to CP Ti tensile samples achieved over 20% elongation before ultimate failure. The similar welded commercially pure UTS was over 95% of the original base metal UTS. The failure occurred in the base metal well away from the fusion or heat affected zones.

The Ti64 to Ti64 weld combination had comparable yield and UTS to the base material with a small loss in ductility. All of the Ti64 to Ti64 samples failed in the fusion zone, probably as a result of the large grains that had formed at the top of the fusion zone.

The Ti5553 to Ti5553 weldment fractured in the fusion zone significantly before the yield strength of the base material was reached indicating an embrittled fusion zone. The presence of porosity may have contributed to the premature failure.

Other than the Ti5553 to Ti5553, the tensile samples of the similar weld combinations performed close to the properties of the base materials. The welded samples suffered a small loss of ductility but retained over 90% of the original base metal strength.

5.2.3.2 Dissimilar Titanium Alloy Welds

Both CP Ti to Ti5553 and CP Ti to Ti64 welds failed during tensile testing in the CP Ti well away from the fusion or heat affected zones. Ti64 and Ti5553 both have tensile strength much higher than the CP Ti, so if the weld zone is not the location for failure, the weaker alloy will be the failure location. This failure location in the base metal rather than in the HAZ of the CP Ti may be as a result of the change in microstructure from equiaxed microstructure to cross-hatched acicular microstructure in the areas affected by the welding process. This microstructure is stronger than the original base material microstructure. The fusion zone in the dissimilar welds will also have alloying occurring that will strengthen the fusion zone compared to original CP Ti.

The Ti64 to Ti5553 weldments fractured in the fusion zone significantly before the yield strength of either material was reached indicating an embrittled fusion zone. The presence of porosity may have contributed to the premature failure. The yield for the embrittled fusion zone was higher than the UTS for the CP Ti, and this may be a reason that the fusion zone in the CP Ti to Ti5553 did not also fail from embrittlement.

Other than the Ti5553 to Ti5553 (Figure 4-19f) and the Ti64 to Ti5553 (Figure 4-19i) all of the tensile samples performed predictably. The welded samples suffered a small loss of ductility but retained over 90% of the original base metal strength.

5.3   Fracture Analysis

All tensile samples that had one of the substrates as CP Ti failed in the base material of the CP Ti well away from the fusion and HAZ zones. This may be as a result of strengthening occurring during the welding process as a result of the changing microstructure. All of the CP Ti failures were very ductile with equiaxed dimples being formed on the fracture surface.

The remaining weld combinations Ti64 to Ti64, Ti5553 to Ti5553 and Ti5553 to Ti64 all suffered from a combination of ductile and brittle fracture modes. Intergranular and/or transgranular fractures were present on the fracture surfaces. Intergranular fracture is generally associated with brittle fractures as whole grains pull away from each other very rapidly along the grain boundaries. In between the intergranular fractures all of these weld combinations had evidence of some ductile equiaxed dimples. With dimpled fracture surfaces it is expected that there would be a certain percentage of elongation before fracture. This also suggests that the fusion zone had some ductility even though it could be far less than the base metal.

The Aramis strain capture work that has been performed by the Department of Materials Science and Engineering, Lehigh University shows the highly localised strain that is occurring in the fusion zone of the dissimilar welds.

5.4 Fusion Zone Composition

The fusion zone of the dissimilar weld combination results in a different alloy composition to that of the two base alloys being welded. An approximation of the fusion composition can be made before welding by assuming a 50/50 mix of the two base alloys. Approximate fusion zone compositions have been calculated and are shown in Table 5-1 with their Al_{eq} and Mo_{eq}.

Table 5-1: Approximate Fusion Zone Compositions % and Al_{eq} and Mo_{eq}

	Ti	Al	V	Mo	Cr	Fe	C	O	N	Al_{eq}	Mo_{eq}
CP Ti to Ti64	94.57	3.12	1.93	0.00	0.01	0.20	0.02	0.17	0.01	4.77	1.79
CP Ti to Ti5553	90.48	2.6	2.55	2.53	1.32	0.30	0.01	0.21	0.01	4.70	6.64
Ti5553 to Ti64	85.56	5.56	4.48	2.53	1.33	0.28	0.02	0.10	0.00	6.51	7.88

For the Ti5553 to Ti5553 weld (Figure 4-30), the distribution of solutes after solidification was relatively uniform and this is shown futher in Figure 4-31 where the Mo_{eq} also stays consistent.

For the Ti64/Ti5553 weld (Figure 4-32), it is clear that due to the vigoruous mixing that has occurred in the weld pool, the solutes from both substrates have been evenly distributed throughout the weld zone. Figure 4-33 shows the Mo_{eq} in the fusion zone also stays consistent and has a value around 8 which is close to the predicted 7.88 from Table 5-1. According to literature a Mo_{eq} of less than 10 should result in the formation of martensite on quenching [32]. The cooling rate from electron beam welding is considerably faster than most other common welding methods e.g. TIG welding [14].

Initial assumptions before welding commenced, were that the Ti5553 dissimilar welds would have enough mixing with the other alloys to reduce the Mo_{eq} sufficiently to cause the formation of visible α phase, α' or α'' martensite in the fusion zone post weld.

The estimated values for the Mo_{eq} shown in Table 5-1 and the values of Mo_{eq} using EPMA in the fusion zone shown in Figure 4-33, having values less than 10, support that the dissimilar Ti5553 fusion zones microstructure should have α phase, α' or α'' martensite present.

The fusion zones of both the CP Ti to Ti5553 and Ti64 to Ti5553 weld combinations produced large β grains with acicular lathes which would indicate α phase or α' martensite phase. The presence of martensite (α' phase) in the fusion zone of both the CP Ti to Ti5553 and Ti64 to Ti5553 weld combinations exhibited a significant hardness increase in the fusion zone over the hardness of either base metals.

6.0   Conclusion and Recommendations

6.1   Similar Titanium Alloy Welds

- Visually acceptable electron beam weldments are achievable through the welding of 1.6mm thick sheets of similar titanium. The alloys that were successfully welded were, commercially pure titanium (α alloy), Ti6Al4V (α+β alloy) and Ti5Al5V5Mo3Cr (β alloy)

- The hardness of the weldments of commercially pure titanium and Ti6Al4V were consistent with the base material. The weldment of the Ti5553 showed a drop in hardness in the HAZ and further reduction in the melt zone.

- The tensile results for commercially pure titanium and Ti6Al4V showed comparable tensile strengths with the base material with a small decrease in elongation. Ti5553 failed below the base metal tensile strength showing very little elongation. Fracture surfaces of the Ti5553 samples showed areas of both brittle and ductile failures.

- Bend tests of commercially pure titanium showed no signs of cracking. Ti6Al4V showed evidence of porosity from welding or micro-cracks forming on the top surface of the weld during the bend test.

6.2   Dissimilar Titanium Alloy Welds

- Visually acceptable electron beam weldments are achievable through the welding of 1.6mm thick sheets of dissimilar titanium alloys. The alloys that were successfully welded were, CP Ti (α alloy) to Ti64 (α+β alloy), CP Ti (α alloy) to Ti5553 (β alloy) and Ti5553 (β alloy) toTi64 (α+β alloy).

- All alloy weld combinations resulted with a weldment with a higher tensile strength than the commercially pure titanium base metal.

- EPMA scans showed that the dissimilar welds were well mixed with consistent composition across their fusion zones.

- Ti5553 to Ti6Al4V welds failed well below the tensile strength of both materials and had very little elongation. Fracture surfaces of these samples showed areas of both brittle and ductile failures.

- Microhardness of the weldment between commercially pure titanium and Ti6Al4V showed a sharp transition on the Ti6Al4V side of the fusion zone between the microhardness of the two base materials. Dissimilar weldments with Ti5553 showed a significant increase in microhardness in the fusion zone.

- Bend tests for commercially pure titanium to Ti6Al4V showed no evidence of cracking.

- Evidence of porosity in the weld was shown in the micrographs of Ti6Al4V to Ti5553.

6.3 Aramis Strain Measurement

Although the Aramis system was employed at a very late stage of this investigation, the results showed some confidence that elongation in the fusion zones could be significant.

6.4 Recommendations for Future Work

Areas of ongoing and future work in this line of research include:

- Looking into post weld heat treatment through the use of either bulk furnace heating or multi-pass electron beam heating to achieve more desirable mechanical properties particularly to the Ti5553 weld combinations.
- Looking into the use of filler metal to change weldment composition and structure.
- Further inspection of the current weldment composition and phase characteristics using SEM, EBSD, TEM and EPMA
- Further analysis using the Aramis System.

7.0 References

1. Bakish, R.W., S. S., *Handbook of Electron Beam Welding* 1964, New York Wiley.
2. Meleka, A.H., *Electron-beam Welding: Principles and Practice*. 1971: McGraw-Hill,.
3. *Operation and Maintenance Instructions - Electron Beam Welder (M8152)*. 1983: Leybold-Haraeus Vacuum Systems Ltd.
4. Serre, I. and J.-B. Vogt, *Mechanical properties of a 316L/T91 weld joint tested in lead-bismuth liquid*. Materials & Design, 2009. **30**(9): p. 3776-3783.
5. Wanjara, P. and M. Brochu, *Characterization of electron beam welded AA2024*. Vacuum, 2010. **85**(2): p. 268-282.
6. Lütjering, G. and J. C.Williams, *Titanium*. 2nd ed, 2007: Springer Berlin Heidelberg.
7. *Titanium and Titanium Alloys - Fundamentals and Applications*, ed. C.L.a.M. Peters. 2003, Weinheim: WILEY-VCH Verlag GmbH & Co. KGaA.
8. Wang, S., Q. Ma, and Y. Li, *Characterization of microstructure, mechanical properties and corrosion resistance of dissimilar welded joint between 2205 duplex stainless steel and 16MnR*. Materials & Design, 2010. **32**(2): p. 831-837.
9. Saresh, N., M.G. Pillai, and J. Mathew, *Investigations into the effects of electron beam welding on thick Ti-6Al-4V titanium alloy*. Journal of Materials Processing Technology, 2007. **192-193**: p. 83-88.
10. Kuruvilla, M., et al., *An investigation of microstructure, hardness, tensile behaviour of a titanium alloy: Role of orientation*. Sadhana, 2008. **33**(3): p. 235-250.
11. Irisarri, A.M., J.L. Barreda, and X. Azpiroz, *Influence of the filler metal on the properties of Ti-6Al-4V electron beam weldments. Part I: Welding procedures and microstructural characterization*. Vacuum, 2009. **84**(3): p. 393-399.
12. Nag, S., et al., *Probing Elemental Partitioning between Alpha and Beta Phases in Titanium Alloys Using 3D Atom Probe Tomography*. Microsc Microanal, 2007. **13**(Suppl 2).
13. Murr, L.E., et al., *Microstructures and mechanical properties of electron beam-rapid manufactured Ti-6Al-4V biomedical prototypes compared to wrought Ti-6Al-4V*. Materials Characterization, 2009. **60**(2): p. 96-105.
14. Short, A.B., *Gas tungsten arc welding of alpha + beta titanium alloys: a review*. Material Science and Technology, 2009. **25**(3): p. 309.
15. Moiseyev, V.N., *Titanium Alloys - Russian Aircraft and Aerospace Applications*. 2005, CRC Press.
16. Arrazola, P.J., et al., *Machinability of titanium alloys (Ti6Al4V and Ti555.3)*. Journal of Materials Processing Technology, 2009. **209**(5): p. 2223-2230.
17. Joshi, V.A., *Titanium Alloys - An Atlas of Structures and Fracture Features*. 2006, Boca Raton: CRC Press.
18. *Titanium and Titanium Alloys*, in *Encyclopedia of Chemical Technology*. 2000.
19. Taylor, B., *Application Note - Metallographic preparation of titanium*. 2008: Struers Ltd.
20. Donachie, M.J., *Titanium - A Technical Guide*. Second ed. 2000: ASM International.

21.   Wang, T., et al., *Influence of processing parameters on microstructure and tensile properties of TG6 titanium alloy.* Materials Science and Engineering: A, 2010. **528**(2): p. 736-744.

22.   Boyer, R., *Attributes, characteristics, and applications of titanium and its alloys.* JOM Journal of the Minerals, Metals and Materials Society, 2010. **62**(5): p. 21-24.

23.   Mueller, S., et al. *Laser beam welding of titanium - A comparison of CO2 and fiber laser for potential aerospace applications.* 2008. Temecula, CA, United states: Laser Institute of America.

24.   Maruyama, T., *Arc welding technology for dissimilar joints.* Welding International, 2003. **17**(4): p. 276-281.

25.   Karimzadeh, F., M. Heidarbeigy, and A. Saatchi, *Effect of heat treatment on corrosion behavior of Ti-6Al-4V alloy weldments.* Journal of Materials Processing Technology, 2008. **206**(1-3): p. 388-394.

26.   Barreda, J.L., X. Azpiroz, and A.M. Irisarri, *Influence of the filler metal on the mechanical properties of Ti-6Al-4V electron beam weldments.* Vacuum, 2010. **85**(1): p. 10-15.

27.   Taylor, B., *Application Note - Metallography of Welds.* 2008: Struers Ltd.

28.   Bosch, J.V.d. and A. Almazouzi, *Compatibility of martensitic/austenitic steel welds with liquid lead bismuth eutectic environment.* Journal of Nuclear Materials, 2009. **385**(3): p. 504-509.

29.   Wei, P.S., Y.K. Kuo, and J.S. Ku, *Fusion zone shapes in electron-beam welding dissimilar metals.* Journal of Heat Transfer, 2000. **122**(3): p. 626-631.

30.   Cottrell, C.L.M., *Electron beam welding -- a critical review.* Materials & Design, 1985. **6**(6): p. 285-291.

31.   Kutz, M., ed. *Mechanical Engineers' Handbook - Materials and Mechanical Design.* 2006, John Wiley & Sons, Inc: Hoboken, New Jersey.

32.   Panza-Giosa, R., *The Effect of Heat Treatment on the Microstructure Evolution and Mechanical Properties of Ti-5Al-5V-5Mo-3Cr, and its Potential Applications in Landing Gears.*, in *Materials Science and Engineering.* 2009, McMaster University: Hamilton, Ontario.

33.   Collings, E.W., *Materials properties handbook: Titanium alloys.* 1994: ASM International.

34.   *Titanium-Aluminum (Ti-Al) Phase Diagram.* 2008 [cited; Available from: http://www.calphad.com/titanium-aluminum.html.

35.   Meshram, S.D. and T. Mohandas, *A comparative evaluation of friction and electron beam welds of near-α titanium alloy.* Materials & Design, 2009. **31**(4): p. 2245-2252.

36.   Cheng, D., et al., *Microstructure and superplasticity of laser welded Ti-6Al-4V alloy.* Materials & Design, 2009. **31**(1): p. 620-623.

37.   Dehghan-Manshadi, A. and R.J. Dippenaar, *Development of [alpha]-phase morphologies during low temperature isothermal heat treatment of a Ti-5Al-5Mo-5V-3Cr alloy.* Materials Science and Engineering: A, 2010. **In Press, Corrected Proof**.

38.   Wain, N., et al., *The influence of carbon on precipitation of [alpha] in Ti-5Al-5Mo-5V-3Cr.* Materials Science and Engineering: A, 2010. **527**(29-30): p. 7673-7683.

39.   Fanning, J.C., *Properties of TIMETAL 555 (Ti-5Al-5Mo-5V-3Cr-0.6Fe).* Journal of Materials Engineering and Performance, 2005. **14**(6): p. 788-791.

40.   Jones, N.G., et al., *Development of chevron-shaped α precipitates in Ti-5Al-5Mo-5V-3Cr.* Scripta Materialia, 2009. **60**(7): p. 571-573.

41.   Jones, N.G., et al., *β Phase decomposition in Ti-5Al-5Mo-5V-3Cr.* Acta Materialia, 2009. **57**(13): p. 3830-3839.

42.   Ng, H.P., et al., *Age-hardening behaviour of two metastable beta-titanium alloys.* Materials Science and Engineering: A, 2010. **527**(26): p. 7017-7026.

43.   Nag, S., et al., *ω-Assisted nucleation and growth of α precipitates in the Ti-5Al-5Mo-5V-3Cr-0.5Fe β titanium alloy.* Acta Materialia, 2009. **57**(7): p. 2136-2147.

44.   Boyer, R., *Processing Properties Relationships of Ti-10V-2Fe-3Al.* Metallurgical Transactions A, 1987. **18A**: p. 2095.

45.   Tetyukhin, V.V. *Current State of the Russian Titanium Industry and VSMPO; Development of New High Strength Alloys for Aircraft and Civil Engineering.* in *13th Annual Titanium Conference; ITA.* 1997.

46.   Gerday, A.F., et al., *Interests and limitations of nanoindentation for bulk multiphase material identification: Application to the [beta] phase of Ti-5553.* Acta Materialia, 2009. **57**(17): p. 5186-5195.

47.   Jones, N.G., et al., *Thermomechanical processing of Ti-5Al-5Mo-5V-3Cr.* Materials Science and Engineering: A, 2008. **490**(1-2): p. 369-377.

48.   Nathan, S., *Dream ticket.* Engineer, 2005. **293**(7687): p. 35-35.

49.   Nag, S., et al., *Elemental partitioning between alpha and beta phases in the Ti-5Al-5Mo-5V-3Cr-0.5Fe (Ti-5553) alloy.* Philosophical Magazine, 2009. **89**(6): p. 535-552.

50.   Clement, N., A. Lenain, and P.J. Jacques, *Mechanical property optimization via microstructural control of new metastable beta titanium alloys.* JOM, 2007. **59**(1): p. 50-3.

51.   Ziolkowski, M., *Modelling of Seebeck effect in electron beam deep welding of dissimilar metals.* COMPEL: The International Journal for Computation and Mathematics in Electrical and Electronic Engineering, 2009. **28**(1): p. 140-153.

52.   Reisgen, U. and T. Dorfmuller, *Developments in micro-electron beam welding.* Microsystem Technology, 2008. **14**(12): p. 1871–1877.

53.   *Recommended Practices for Electron Beam Welding.* ANSI/AWS C7.1-92. 1999: American Welding Society.

54.   Löwer, P.T. *Current Development of the Electron Beam Technology in Europe.* in *International Electron Beam Welding Conference.* 2009. McCormick Place, Chicago: AWS.

55.   Taban, E., J.E. Gould, and J.C. Lippold, *Dissimilar friction welding of 6061-T6 aluminum and AISI 1018 steel: Properties and microstructural characterization.* Materials & Design, 2009. **31**(5): p. 2305-2311.

56.   Venkata Ramana, P., et al., *Microstructure and residual stress distribution of similar and dissimilar electron beam welds - Maraging steel to medium alloy medium carbon steel.* Materials & Design, 2009. **31**(2): p. 749-760.

57.   Fazel-Najafabadi, M., S.F. Kashani-Bozorg, and A. Zarei-Hanzaki, *Joining of CP-Ti to 304 stainless steel using friction stir welding technique.* Materials & Design, 2010. **31**(10): p. 4800-4807.

58.   Wei, P.S. and F.K. Chung, *Three-Dimensional Electron-Beam Deflection and Missed Joint in Welding Dissimilar Metals.* Journal of Heat Transfer, 1997. **119**(4): p. 832-839.

59.   Davis, J.R., ed. *ASM Specialty Handbook on Stainless Steels.* 1994, ASM International.

60. *Guide for the Visual Inspection of Welds*. ANSI/AWS B1.11-88. 1988: American Welding Society.

61. *Standard Test Method for Microindentation Hardness of Materials*. ASTM E384 – 99e1. 1999: ASTM International.

62. *Standard Methods for Mechanical Testing of Welds*. ANSI/AWS B4.0-92. 1992: American Welding Society.

63. *Standard Test Methods for Tension Testing of Metallic Materials [Metric]*. ASTM E8M – 04. 2004: ASTM International.

64. Quan, Y., et al., *CO2 laser beam welding of dissimilar magnesium-based alloys*. Materials Science and Engineering: A, 2008. **496**(1-2): p. 45-51.

65. Lee, M., et al., *Application of 3D Measurement System with CCD camera in Microelectronics*. Advanced Packaging, 2003.

66. Wanjara, P., M. Brochu, and M. Jahazi, *Thin Gauge Titanium Manufacturing Using Multiple-Pass Electron Beam Welding*. Materials and Manufacturing Processes, 2006. **21**(5): p. 439-451.

67. Murthy, K.K. and S. Sundaresan, *Fracture toughness of Ti-6Al-4V after welding and postweld heat treatment*. Welding Journal, 1997. **76**(2): p. p. s81-s91.

68. Wanjara, P., M. Brochu, and M. Jahazi, *Ti-6Al-4V electron beam weld qualification using laser scanning confocal microscopy*. Materials Characterization, 2005. **54**(3): p. 254-262.

69. Nyakana, S.L., J.C. Fanning, and R.R. Boyer, *Quick reference guide for β titanium alloys in the 00s*. Journal of Materials Engineering and Performance, 2005. **14**(6): p. 799-811.

Appendices

Appendix A   Certificate of Chemical Composition

AUT UNIVERSITY
SCHOOL OF ENGINEERING
PRIVATE BAG 92006
AUCKLAND NZ 1010
ATTENTION : Ryan Mitchell

Certificate Of Analysis

Samples	Ti	N	C	O	Fe	Al	V	Sn	Ru	Pd	Co	Mo	Cr	Ni	Nb	Zr
	%	%	%	%	%	%	%	%	%	%	%	%	%	%	%	%
Ti5553 Billet	~Bal	<.01	.01	.12	.37	5.03	4.97	<.01	<.01	<.01	<.01	4.90	2.65	<.01	<.01	.07
Ti CP	~Bal	.01	.01	.28	.22	.16	<.01	<.01	<.01	<.01	<.01	<.01	<.01	<.01	<.01	<.01
Ti5553 Plate	~Bal	<.01	.01	.14	.38	5.03	5.10	<.01	<.01	<.01	<.01	5.06	2.64	<.01	<.01	<.01
Ti6Al4V	~Bal	<.01	.02	.05	.17	6.08	3.85	<.01	<.01	<.01	<.01	<.01	.02	<.01	<.01	<.01

Methods Used :
ICP-AES

Bernard Hedger

Page 1 of 1

Figure A-1: Certificate of chemical composition for the titanium alloys.

Appendix B   Power Settings while Finding EBW Parameters

Table A-1: Ti64 EBW power settings

Transverse speed		Beam Current	Visual Description
IPM	mm/s	mA	
30	12.7	5.0	Full penetration with a scalloped pulsed pattern
30	12.7	4.5	Full penetration with a scalloped pulsed pattern, some areas showing consistent seam.
20	8.5	3.5	Generally clean full penetration weld with one inconsistency defect in the weld.
20	8.5	3.5	Generally clean full penetration weld with more inconsistency defects than the previous trial.
20	8.5	3.0	Clean weld without inconsistencies. Full even penetration.

Table A-2: CP Ti EBW power settings

Transverse speed		Beam Current	Visual Description
IPM	mm/s	mA	
20	8.5	3.0	Clean weld without inconsistencies. Less penetration than Ti64.
20	8.5	3.2	Clean weld without inconsistencies. Full even penetration.
20	8.5	3.2	Clean weld without inconsistencies. Full even penetration.

Table A-3: CP Ti to Ti64 EBW power settings

Transverse speed		Beam Current	Visual Description
IPM	mm/s	mA	
20	8.5	3.2	Full penetration with some inconsistencies on the weld surface.
20	8.5	3.0	Clean weld without inconsistencies. Full even penetration.

Table A-4: Ti5553 combination EBW power settings

Transverse speed		Beam Current	Visual Description
IPM	mm/s	mA	
20	8.5	3.0	Full penetration with some inconsistencies on the weld surface.
20	8.5	3.0	Full penetration with some inconsistencies on the weld surface.
20	8.5	3.0	Clean weld without inconsistencies. Full even penetration.

Appendix C   Weld Width Measurements

Table A-5: Weld width measurements
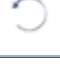
	Measurement location	CP-64	Measurement location	CP-CP
Top	1	2.668	1	2.694
	2	2.619	2	2.737
	3	2.571	3	2.694
	4	2.651	4	2.824
	5	2.732	5	2.759
	6	2.715	6	2.769
	7	2.635	7	2.791
	stdev	0.06	stdev	0.05
	average	2.66	average	2.75
Bottom	1	1.308	1	1.329
	2	1.215	2	1.268
	3	1.272	3	1.316
	4	1.252	4	1.256
	5	1.243	5	1.065
	6	1.301	6	1.09
	7	1.178	7	1.34
	stdev	0.05	stdev	0.11
	average	1.25	average	1.24

	Measurement location	5553-5553	Measurement location	5553-CP
Top	1	2.416	1	2.671
	2	2.261	2	2.628
	3	2.368	3	2.573
	4	2.248	4	2.559
	5	1.928	5	2.643
	6	2.189	6	2.607
	7	2.344	7	2.595
	stdev	0.16	stdev	0.04
	average	2.25	average	2.61
Bottom	1	0.957	1	1.103
	2	1.005	2	0.675
	3	0.993	3	0.971
	4	0.993	4	0.099
	5	1.053	5	0.076
	6	0.837	6	0.54
	7	1.232	7	1.105
	stdev	0.12	stdev	0.44
	average	1.01	average	0.65
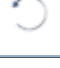
	Measurement location	64-64	Measurement location	5553-64
Top	1	2.57	1	2.622
	2	2.619	2	2.589
	3	2.522	3	2.57
	4	2.587	4	2.522
	5	2.667	5	2.62
	6	2.7	6	2.59
	7	2.619	7	2.489
	stdev	0.06	stdev	0.05
	mean	2.61	average	2.57
Bottom	1	1.315	1	0.776
	2	1.308	2	0.598
	3	1.286	3	0.921
	4	1.293	4	0.679
	5	1.207	5	0.437
	6	1.279	6	0.711
	7		7	0.55
	stdev	0.04	stdev	0.16
	mean	1.28	average	0.67

Appendix D Struers Metallographic Preparation of Titanium Procedure

Table A-6: Struers Machine Settings – Titanium Grinding [19].

Step	PG	FG 1
Surface	SiC-Paper #320	MD-Largo
Abrasive Type		DiaPro Allegro/Largo
Lubricant Type	Water	
Speed [RPM]	300	150
Force [N]	150	180
Holder direction	>>	>>
Time [min]	1	4

Table A-7: Struers Machine settings – Titanium Polishing [19].

Step	OP
Surface	MD-Chem
Abrasive Type	OP-S, 0.04 μm
Lubricant Type	
Speed [RPM]	150
Force [N]	210
Holder direction	><
Time [min]	5

Comments	PG Time: As needed. FG: For cp Titanium can MD-Largo / DiaPro Allegro/Largo can be replaced by MD-Plan/DiaPro Plan. OP: Mix 90 ml OP-S + 10 ml hydrogen peroxide (30%). OP Time: 5-10 min. See Application Note: "Metallographic preparation of titanium".

Appendix E   Solidworks Drawings
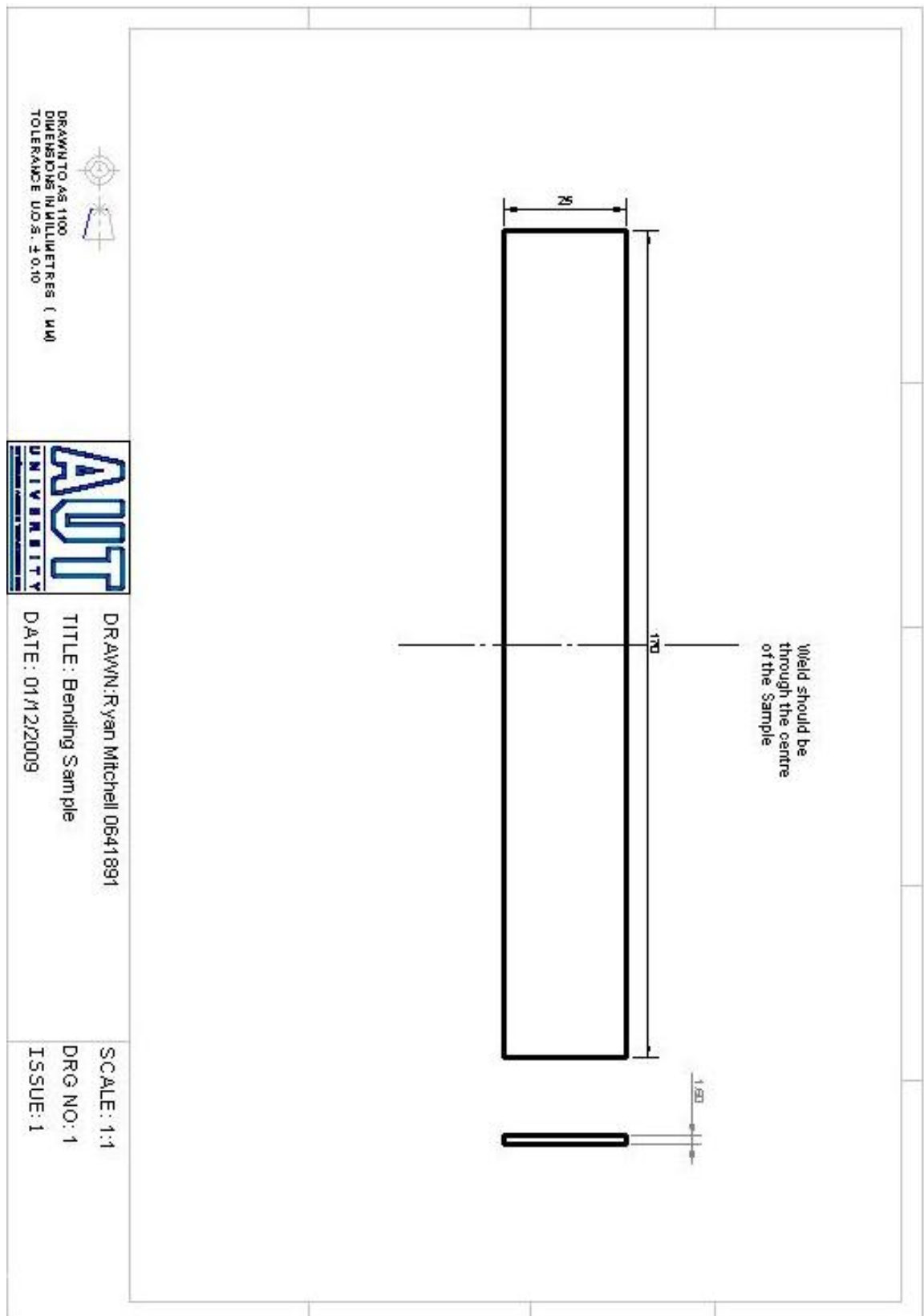
Figure A-2: Solidworks drawing for bending samples [62].
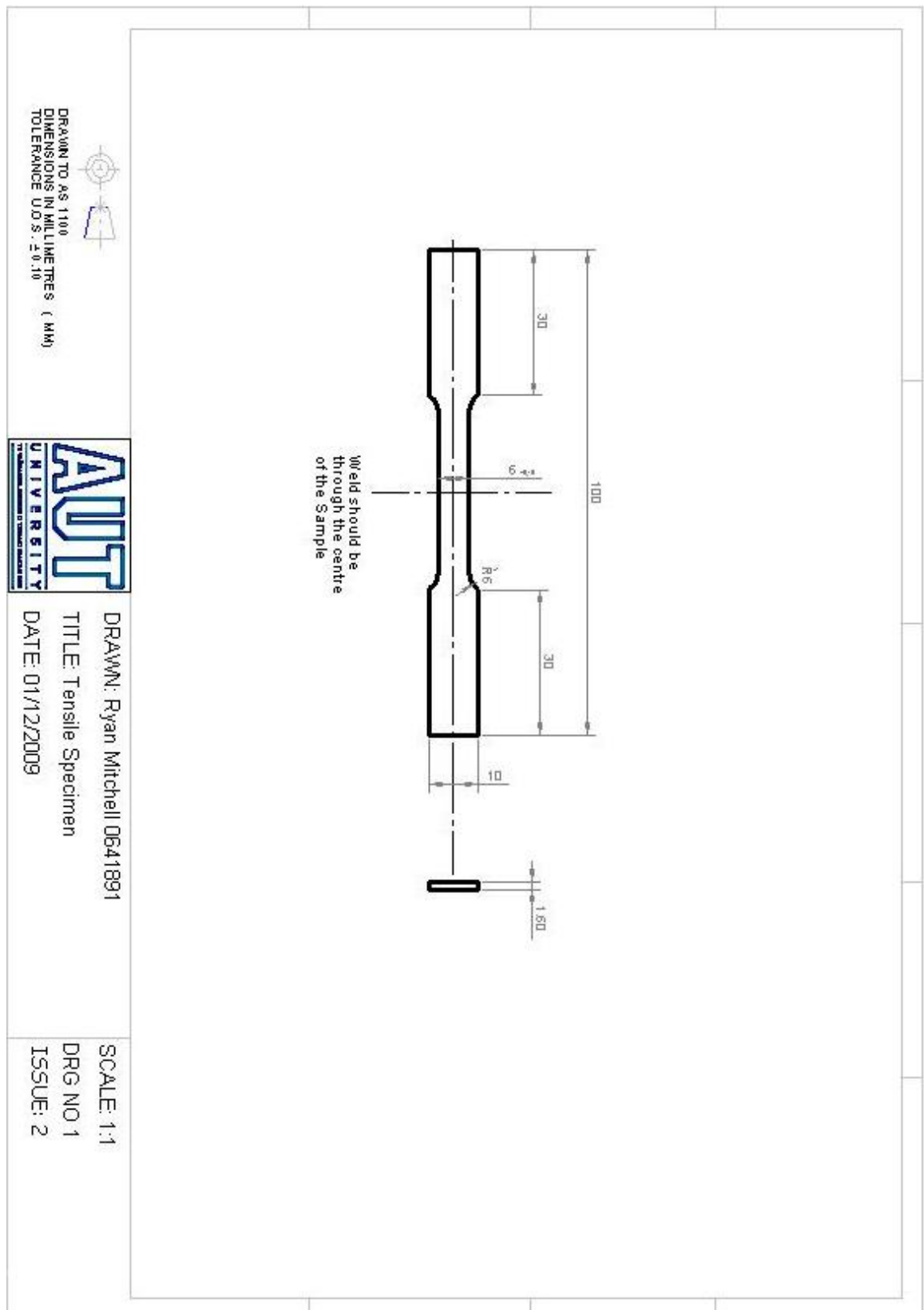
Figure A-3: Solidworks drawing for undersized tensile samples [63].

Appendix F   Co-authored Publications

Appendix F-1: Proceedings, International Conference on Structural Integrity and Failure 2010, Auckland University, New Zealand

Characteristics of Electron Beam Welded Ti & Ti alloys

Ryan Mitchell [1, a], Andrew Short [2,b], Timotius Pasang [1,c] and Guy Littlefair [1,d]

[1] Dept of Mechanical and Manufacturing Engineering, Level 3 WS Bldg, 24 St Paul Street, AUT University, Auckland 2010, New Zealand

[2] Melt Tools Ltd. 60 Kiwi Esplanade, Mangere Bridge, Manukau 2022, New Zealand

[a] ryan.mitchell.nz@gmail.com, [b] andrew@melttools.com [c] tpasang@aut.ac.nz
[d] guy.littlefair@aut.ac.nz

Abstract. Similar and dissimilar butt joint welds comprising combinations of commercially pure grade 4 titanium (CP-Ti), Ti-6Al-4V (Ti-64) and Ti-5Al-5V-5Mo-3Cr (Ti-5553) were created using the electron beam process. The resultant welds were studied by means of metallography, optical microscopy, mechanical testing and scanning electron microscopy. Mechanical testing was performed on welded samples to study the joint integrity and fracture characteristics. A scanning electron microscope investigation was performed on the fracture surface to reveal their fracture modes. While all weldments were crack free and most weldments exhibited mechanical properties comparable to the base metal, negligible ductility was exhibited during tensile testing joints of Ti-5553 welded to either Ti-64 or Ti-5553.

Introduction

Titanium and its alloys offer high strength, low weight, hence, high-strength-to-weight ratio and excellent corrosion resistance. With such properties, they have been used, primarily on critical components, in various areas such as aerospace, automotive, chemical industries, sports equipment, and most recently in medical. The elements that stabilise the α phase in titanium alloys are often described in terms of an aluminium equivalent (Eq. 1), and elements that stabilise the β phase are often described in terms of a molybdenum equivalent (Eq. 2) [1].

$$Al_{eq} = Al + 0.33Sn + 0.17Zr + 10 \cdot O \tag{1}$$

$$Mo_{eq} = Mo + 0.67V + 0.28N + 0.2Ta + 0.4W + 2.5Fe + 1.25Cr + 1.7Mn + 1.25Ni + 1.7Co \tag{2}$$

where the element levels are in wt %

As such, titanium and its alloys may be categorised as unalloyed, α and near-α alloys, α+β alloys and metastable β. These alloys may be fusion welded together, insomuch as the weldments exhibit acceptable mechanical properties. While titanium and its alloys cannot be fusion welded to ferrous or aluminium alloys due to the formation of brittle intermetallic phases in the fusion zone [2], a variety of dissimilar weldments are possible using various combinations of titanium and its alloys. Electron beam welding is perhaps the most suitable process for studying the welding metallurgy and mechanical properties of such weldments as the molten metal in the weld zone is removed from atmosphere and the possibility of subsequent interstitial element ingression in the fusion zone. Furthermore, such weldments are subject to minimal heat input and exhibit the best ductility and toughness of the fusion processes [2]. This paper provides a report of metallurgical and mechanical properties for similar and dissimilar butt welds created by electron beam welding the various possible combinations of unalloyed titanium (ASTM grade 4), the most common titanium alloy α+β Ti-6Al-4V and a relatively new metastable β alloy Ti-5Al-5V-5Mo-3Cr.

Experimental Procedure

Substrates comprising commercially pure grade 4 titanium (CP-Ti), Ti-6Al-4V (Ti-64) and Ti-5Al-5V-5Mo-3Cr (Ti-5553) were used for the investigations. The alloying elements were determined using a ICP scan and the C, N, O interstitials by Leco combustion (Table 1).

Table 1 : Chemical Composition [wt%]

	Ti	Al	V	Mo	Cr	Fe	C	O	N	Al_{eq}	Mo_{eq}
CP-Ti	Bal	0.16	<0.01	<0.01	<0.01	0.22	0.01	0.28	0.01	2.96	0.55
Ti-64	Bal	6.08	3.85	<0.01	0.02	0.17	0.02	0.05	<0.01	6.58	3.03
Ti-5553	Bal	5.03	5.1	5.06	2.64	0.38	0.01	0.14	<0.01	6.43	12.80

The CP-Ti and Ti-64 substrates for the butt joints (measuring 60x30x1.6mm) were cut from 1.6mm sheet using a guillotine. The Ti-5553 specimens were cut from 8mm plate to dimensions of approximately 60x30x1.8mm using electronic discharge machine (EDM) wire cutting. The specimen thickness was further reduced using a linisher to 1.7mm. Before welding, the joint edges were filed, cleaned with a dedicated Scotch-Brite® and then cleaned with acetone. Autogenous butt welds were made in the down-hand position using 150kV welding voltage, a traverse speed of 8.5mm/s and welding currents shown in Table 2. The beam was focused on a targeting block before welding giving the smallest, most localised, intense spot. The resultant fusion zone dimensions were obtained from optical measurements of the top and bottom surfaces of the weldments (Table 2).

Table 2: Weld parameters and fusion zone dimensions

Substrate A	Substrate B	Welding current [mA]	Fusion zone top width [mm]	Fusion zone bottom width [mm]
CP-Ti	CP-Ti	3.2	2.75 ± 0.05	1.24 ± 0.11
CP-Ti	Ti-64	3.0	2.66 ± 0.06	1.25 ± 0.05
CP-Ti	Ti-5553	3.0	2.61 ± 0.04	0.65 ± 0.44
Ti-64	Ti-64	3.0	2.61 ± 0.06	1.28 ± 0.04
Ti-64	Ti-5553	3.0	2.57 ± 0.05	0.67 ± 0.16
Ti-5553	Ti-5553	3.0	2.25 ± 0.16	1.01 ± 0.12

Figure 1 : (a) top surface (b) transverse cross-section

Two subsize tensile specimens (ASTM E 8M – 04) were made from each weldment (**Error! Reference source not found.**) and also each base metal. With the former specimens, the weld located transversely and in the centre of the yield zone. A 25mm extensometer was used to measure the specimen elongation during testing. The tensile tests were conducted at a speed of 3 mm/min. Macro and micro optical examination and hardness testing was conducted on transverse cross sections of the weldments and sections revealing the rolled microstructure of the base metal. Standard metallography procedures for titanium were used. The fracture surfaces of the tensile specimens for each base metal and weld combination were examined using SEM to identify the fracture mode. A micro Vickers testing machine was used (following ASTM E 384 – 99$^{\varepsilon}$1). The average hardness in the fusion zone of the similar and dissimilar weldments was calculated from hardness measurements taken down the centre of the transverse section. A transverse hardness profile across the weld was taken horizontally spanning 8mm across the weld zone. Wrap-around guided bend tests to generate 2.3% elongation (ANSI-AWS B4.0-92: Figure A3) were performed on the weld face and root face for all weld combinations except for Ti5553.

Results

The results of the mechanical tests including fracture location and tensile test fracture modes are shown in Table 3. Root and face bend tests of the CP-Ti to CP-Ti, CP-Ti to Ti-64, Ti-64 to Ti-64 revealed adequate ductility in all instances. No bend tests were conducted on samples with Ti-5553

alloy due to the negligible ductility. The transverse hardness profiles revealed a variety of behaviours as shown in Figure 2.

Table 3 : Mechanical properties, fracture location and tensile test fracture modes of base metal and weldments.

Substrate A	Substrate B	$\sigma_{y,0.2}$ [MPa]	σ_{UTS} [MPa]	Elongation at Fracture [%]	Mean Hardness [$H_{V\,0.3}$]	Location of Fracture	Fracture Mode
CP-Ti	-	630 ± 4	693 ± 7	27.4 ± 0.6	250 ± 17	-	Ductile
Ti-64	-	941 ± 1	983 ± 1	13.1 ± 0.5	332 ± 9	-	Ductile
Ti5553	-	1028 ± 8	1053 ± 7	12.7 ± 0.7	333 ± 10	-	Ductile
CP-Ti	CP-Ti	528 ± 5	660 ± 8	22.5 ± 2.1	255 ±18	CP-Ti BM	Ductile
CP-Ti	Ti-64	547 ± 11	673 ± 6	19.3 ± 0.9	272 ± 8	CP-Ti BM	Ductile
CP-Ti	Ti-5553	566 ± 32	655 ± 1	15.5 ± 1.5	396 ± 8	CP-Ti BM	Ductile
Ti-64	Ti-64	959 ± 3	1010 ± 2	8.5 ± 0.9	332 ± 4	Fusion Zone	Ductile+Brittle
Ti-64	Ti-5553	-	899 ± 103	0.9 ± 0.4	405 ± 11	Fusion Zone	Ductile+Brittle
Ti-5553	Ti-5553	-	778 ± 16	0.8 ± 0.4	289 ± 3	Fusion Zone	Ductile+Brittle
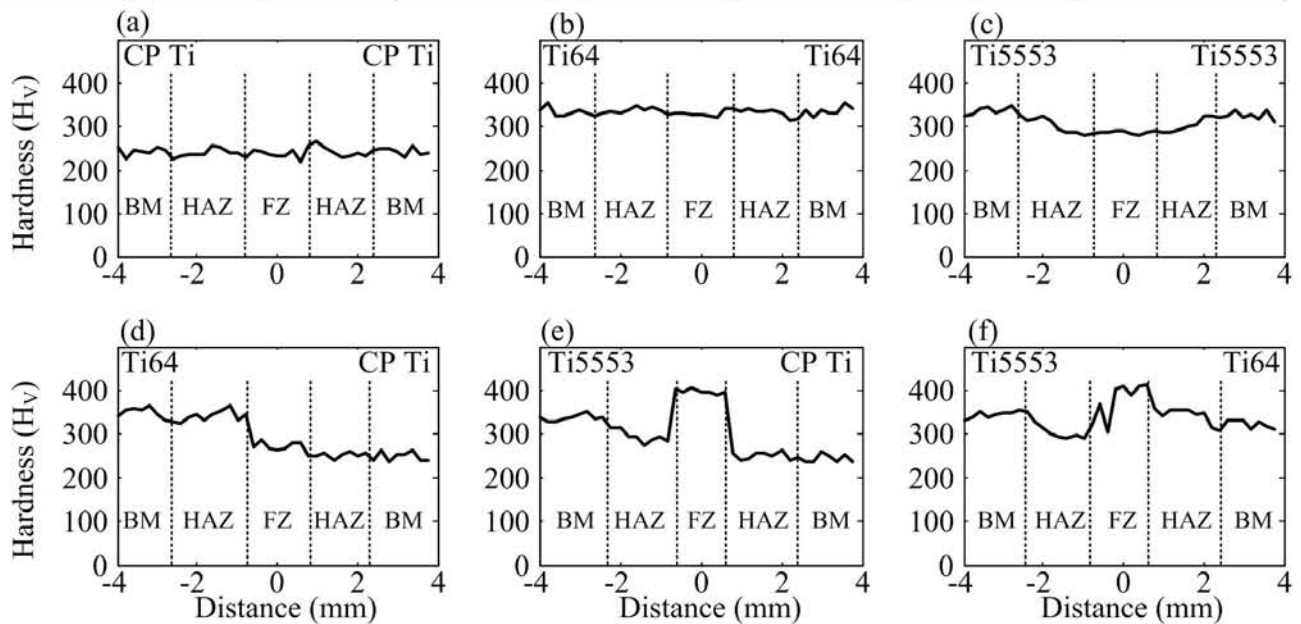
Figure 2: Transverse hardness profiles of similar (a, b, c) and dissimilar (d, e, f) butt weldments. BM = base metal, HAZ = Heat affected zone, FZ = fusion zone.
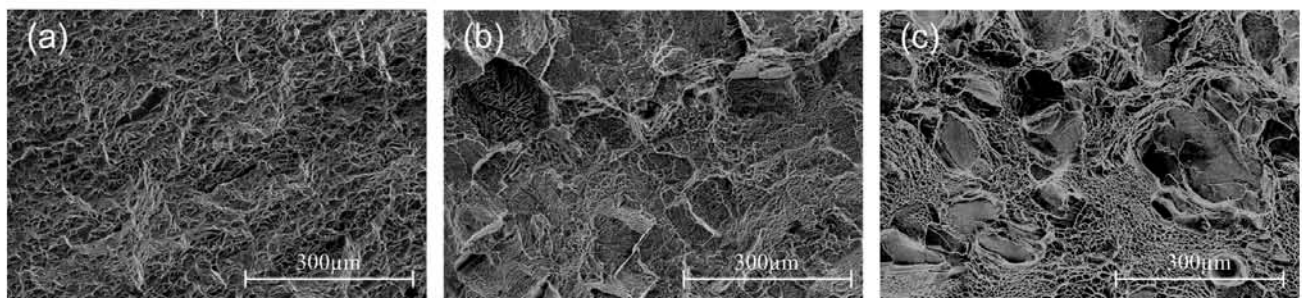
Figure 3: Representative SEM images of the fracture surfaces (a) Ti -CP base metal (b) Ti-64 fusion zone (c) Ti-5553 fusion zone

Discussion

The tensile and hardness properties for the base metal and weldments are generally comparable with that found in the literature (CP-Ti [3], Ti-64 [3-5], Ti-5553 [2], CP-Ti to CP-Ti [3] and Ti-64 to Ti-64 [3-6]). No literature was available to compare weldments involving either dissimilar joints or Ti-5553. The CP-Ti to Ti-64 and CP-Ti to Ti-5553 weldments fractured in the CP-Ti basemetal and exhibited mechanical properties comparable to CP-Ti to CP-Ti, albeit with reduced ductility. This

122

behaviour may be attributed to the lower strength and therefore preferential yielding of the CP-Ti basemetal. The Ti-5553 to Ti-64 and Ti-5553 to Ti-5553 weldments fractured in the fusion zone significantly before the yield strength of either material was reached indicating an embrittled fusion zone. The transverse hardness profiles are relatively constant for CP-Ti to CP-Ti and Ti-64 to Ti-64 (Figure 2 a, b). However, a softening effect is revealed in the heat-affected zone (HAZ) and fusion zone (FZ) of the Ti-5553 (Figure 2 c). The dissimilar CP-Ti to Ti-64 hardness profile is evident from the supposition of the associated similar substrate hardness profiles (cf. Figure 2 a, b with d). However, the CP-Ti to Ti-5553 and Ti-5553 to Ti-64 weldments reveal a marked hardening in the fusion zone (cf. Figure 2 a, b, c with e, f). The differing hardness may be attributed to the formation of a fine α phase and/or a brittle omega phase which may be resolved using a transmission electron microscope (TEM).

One method to achieve a more favourable fusion zone microstructure for welds involving Ti-5553 may be to modify the fusion zone chemistry by selecting an appropriate filler material. A number of practical diagrams have been developed using nickel and chromium equivalents for the Fe-Cr-Ni alloy system e.g. Shaeffler, Delong or WRC-1992. This method has yet be developed for titanium alloys using the aluminium and molybdenum equivalents [7]. An obvious filler material would be an unalloyed grade as such joints have shown enhanced ductility for thick Ti-64 specimens [8]. However, it is evident from the hardness profile of CP-Ti to Ti-5553 that the fusion zone would still exhibit hardening. A second method would involve an ageing treatment to reduce the detrimental fusion zone microstructure [9]. Further studies should also investigate the properties of similar joints made using the gas tungsten arc (GTAW) welding process.

Summary

Similar and dissimilar combinations of commercially pure titanium (CP-Ti), Ti-6Al-4V (Ti-64) and Ti-5Al-5V-5Mo-3Cr (Ti-5553) may be welded using the electron beam process to produce crack-free welds. However, tensile properties comparable to the base material could only be achieved with CP-Ti to CP-Ti, CP-Ti to Ti-64, Ti-64 to Ti-64 and CP-Ti to Ti-5553. Where Ti-5553 was welded to either Ti-64 or Ti-5553, the weldment exhibited negligible ductility. Future work should investigate post weld heat treatments, alloying wires and/or complementary welding processes to improve the ductility of the fusion zone in such weldments.

Acknowledgments

References

1. Lütjering, G. and J.C. Williams, *Titanium* 2003, Berlin Springer. 23 - 30
2. Nyakana, S., J. Fanning, and R. Boyer, *Quick reference guide for β titanium alloys in the 00s.* Journal of Materials Engineering and Performance, 2005. **14**(6): p. 799-811.
3. Wanjara, P., M. Brochu, and M. Jahazi, *Thin Gauge Titanium Manufacturing Using Multiple-Pass Electron Beam Welding.* Materials and Manufacturing Processes, 2006. **21**(5): p. 439-451.
4. Murthy, K.K. and S. Sundaresan, *Fracture toughness of Ti-6Al-4V after welding and postweld heat treatment.* Welding Journal, 1997. **76**(2): p. s81-s91.
5. Rao, K.P., K. Angamuthu, and P.B. Srinivasan, *Fracture toughness of electron beam welded Ti6Al4V.* Journal of Materials Processing Technology, 2008. **199**(1-3): p. 185-192.

6. Wanjara, P., M. Brochu, and M. Jahazi, *Ti-6Al-4V electron beam weld qualification using laser scanning confocal microscopy.* Materials Characterization, 2005. **54**(3): p. 254-262.

7. Jones, S.A., *Refinement of Ti6Al4V weld metal structures during gas-tungsten arc welding.* 2003, Open University (United Kingdom).

8. Barreda, J.L., et al., *Electron beam welded high thickness Ti6Al4V plates using filler metal of similar and different composition to the base plate.* Vacuum, 2001. **62**(2-3): p. 143-150.

9. Jones, N.G., et al., *β Phase decomposition in Ti–5Al–5Mo–5V–3Cr.* Acta Materialia, 2009. **57**(13): p. 3830-3839.

Appendix F-2: Proceedings, XXX. Verformungskundliches Kolloquium 2011, Planneralm, Austria.

STRAIN DISTRIBUTION IN TENSILE TEST OF ELECTRON BEAM WELDED DISSIMILAR TITANIUM ALLOYS

T. Pasang[(1)], J. C. Sabol[(2)], W. Z. Misiolek[(2)], R. Mitchell[(1)], A. Short[(3)]

[(1)]Dept. of Mechanical & Manufacturing Eng., AUT University, Auckland – New Zealand
[(2)]Institute for Metal Forming, Lehigh University, Bethlehem, Pennsylvania - USA
[(3)]Melt Tools Ltd and AUT University, Auckland – New Zealand
Corresponding author: tpasang@aut.ac.nz

Introduction

There is a need to optimize the engineering and economical performance of titanium products which find increasing use in aerospace, biomedical and petrochemical applications. One way of tailoring titanium properties is through welding of dissimilar titanium alloys. However, the deformation behaviour of such welded components is unknown. Therefore, an extensive analysis of the deformation behaviour of Electron beam Welded (EBW) dissimilar titanium alloys was performed.

Background and Experimental Procedure

Previous works on characterisation of EBW dissimilar titanium alloys involving Ti-6Al-4V (Ti64) and Ti-5Al-5V-5Mo-3Cr (Ti5553) revealed that the weld zone was susceptible to cracking during tensile testing [1]. The total strain measured was 1% accompanied by a tensile strength of about 900 MPa. It is worth noting that Ti64 and Ti5553 alloys have comparable tensile strengths, i.e. 983 MPa and 1053 MPa, respectively. On the other hand, EBW specimen of commercially pure titanium (CP Ti) and Ti64 as well as CP Ti and Ti5553 fractured at the base metal of CP Ti due to its lower strength i.e. around 690 MPa [1]. This strength value is comparable or slightly lower than that of CP Ti alone. The total strain measured on the CP Ti/Ti64 and CP Ti/Ti5553 was between 15 and 20%. Note that all these strain values were measured within the total gage length, and not specifically within the weld areas.

Micrographs of fracture surfaces from a scanning electron microscope (SEM), showed microvoid coalescence (dimples) rather than typical brittle fracture characteristics on all samples including those that fractured at strains of 1%. This observation led to the interest in localized strain measurements during deformation in the vicinity of the weld area. Tensile testing was selected as a method of studying strain distribution simulating the same phenomenon during metal forming operations.

Strain distribution within a sample during tensile testing can be measured using various techniques such as (i) clip-on extensometers, (ii) directly-mounted strain gages, (iii) optical devices, and (iv) video extensometers. The first two types are of contact-typed, and the last two are categorised as non-contact. Both the optical and the video extensometers are fairly useful if strain on a particularly small area of interest is to be determined.

Aramis - a system combining a non-contact 3D image correlation photogrammetry, a pair of high speed cameras and a computer/software (Figure 1) [2], was employed to measure the full field strain distribution in the vicinity of the welds on EBWed similar and dissimilar titanium during tensile testing. The frequency at which images are captured can be varied depending on the resolution needed and time allowed per test. An interval of one second was used throughout all of the experiments conducted in this study. In order for the software to recognize any movement or deformation during a tensile test in the progressing images, black-and-white paint must applied on the surface of interest to provide sufficient contrast. The black paint on top of the white surface should appear as spots. Any changes in the spots' locations on the sample surface are captured by the cameras, stored and processed by the computer/software. This is one of the main advantages Aramis that all data can be stored for post-analysis [2].
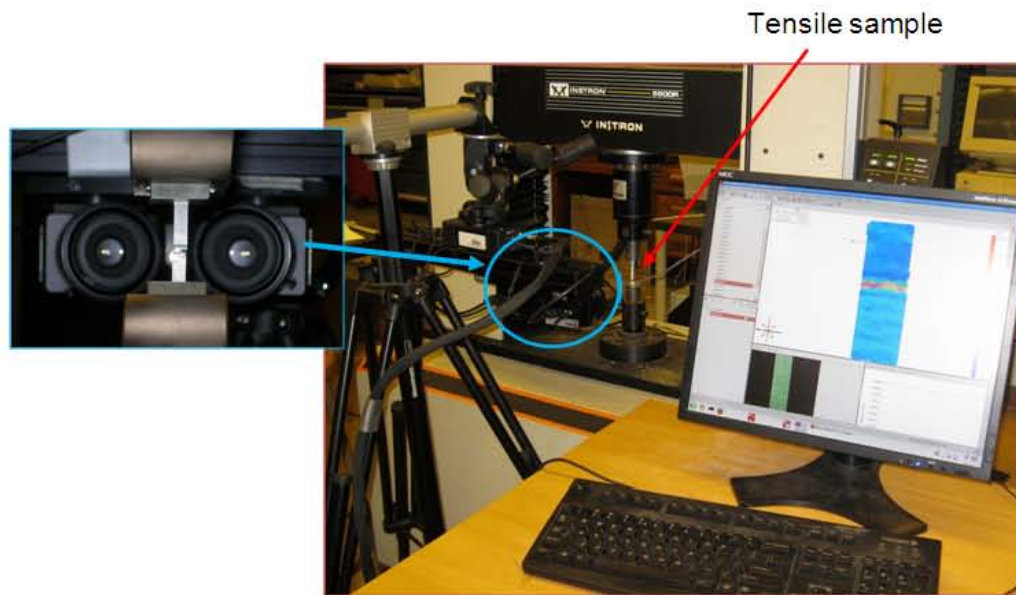
Figure 1. Photograph showing a set-up of the tensile test and a welded sample fractured in front of two cameras used in this experiment (inset).

Sub-size tensile samples according to ASTM E8 were used in this investigation. An Instron 5500R tensile frame with a 100kN and a cross head speed of 3mm/min was used.

Results and Discussion

EBW produces a relatively narrow weld zone, i.e. in these cases ≤ 3 mm width. Therefore, any strain that occurred within this area is extremely difficult to measure. Localized strain on a welded part is important for design purposes, e.g. to know the ductility and fatigue resistance of the welds. If one is to determine localized strain during tensile testing of an EBW sheet, the non-contact type measurements would be an appropriate option.

A typical metallography cross-section of an EBWed sample is shown in Figure 2a. Depending on the location, the width of the weld zone is between 1.5 mm (at the bottom) to 3 mm (at the top surface). The top surface is placed facing the cameras (Figure 1-inset). The weld zone has a columnar grain structure. A distinct fusion line can be seen on both sides of the weld. On the Ti5553 side, the grain structures are more obvious and appear more

equiaxed in the heat affected zone (HAZ). The beta phase is present in the Ti5553. The HAZ on Ti64 side consists of α-prime (martensite).

Figure 2b shows no strain at the initial stage. Figure 2c is an example of the localized strain distribution at the gage length prior to fracture. It is clearly shown that strains were highly concentrated at the weld region. The recorded strain for this particular case was about 10% before the sample fractured. There is a need to analyze and compare total elongation to the localized elongation at the weld region since they represent different values for different material combinations (see Table 1). It also implies that the weld zone has higher ductility than it was previously thought.
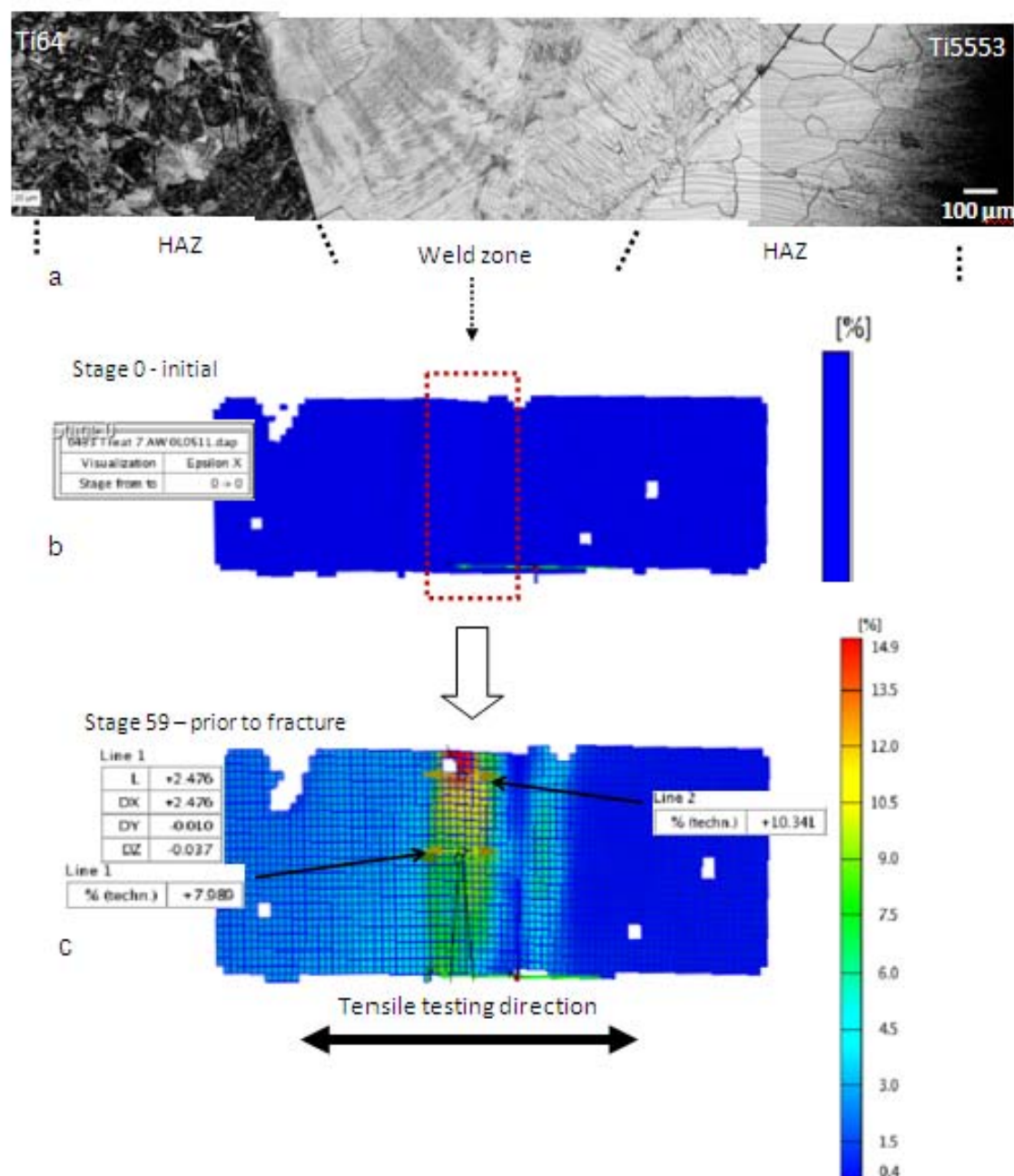
Figure 2. Images showing (a) a weld profile, (b) initial stage prior to sample being pulled, and (c) highly localized strains at the weld zone. All images correspond to the as-welded Ti64/Ti5553.

Table 1. Preliminary tensile test data

Welding combinations	UTS or Premature Fracture Strength (MPa)	Yield Strength (MPa)	Total Elongation at Fracture (%)	Localized deformation in the vicinity of the weld (%)	Fracture Location***
CP Ti/CP Ti	552	430	35.9	21.0	BM-CP Ti
CP Ti/Ti64	505	400	26.3	1.5	BM-CP Ti
CP Ti/Ti5553	505*	400	17.5**	1.8	WZ
Ti64/Ti64	796*	740	15	10.2	WZ
Ti64/Ti5553	744*	715	12	10.1	WZ
Ti5553/Ti5553	678*	N/A	10.5	4.2	WZ

* Indicates premature fracture before necking
** Indicates adjustment of strain due to grip settling
*** WZ = weld zone; BM = base metal

Summary

With the assistance of the Aramis system, we have observed noticeable ductility within the weld area reaching around 10%. This information shows a higher degree of complexity for different combinations of materials resulting in fracture mostly in the weld region. Additional analysis is needed to formulate conclusions of the study.

References

1. R. Mitchell, A. Short, T. Pasang and G. Littlefair, *"Characteristics of EBW Ti Alloys"*, Structural Integrity and Failure, SIF 2010, University of Auckland.
2. M. Lee, M. Pecht, J. Tyson and T. Schmidt, *"Application of 3D Measurement System with CCD Camera in Microelectronics"*, http://www.trilion.com/

Appendix F-3: Proceedings, International Conference on Technology of Plasticity 2011, Aachen, Germany. Also to be published in Steel Research International.

Metallurgical Characterization of Deformed Electron Beam Welded Dissimilar Titanium Alloys

T. Pasang[1,2)*], J.C. Sabol[2)], W.Z. Misiolek[2)], R.M. Mitchell[1)], A.B. Short[3)], G. Littlefair[1)], A.J. Thome[2)]

[1)] Mechanical and Manufacturing Engineering, AUT University, Auckland / New Zealand; [2)] Institute of Metal Forming, Lehigh University, Bethlehem, Pennsylvania / USA; [3)] Melt Tools and AUT University, Auckland / New Zealand

* Corresponding author: E-mail address: tpasang@aut.ac.nz; Tel.: +64-9-921 9999 x8760

Abstract

The metallurgy of Electron Beam Welded (EBW) dissimilar titanium alloys was investigated by means of metallography, mechanical testing, scanning electron microscopy (SEM) and electron microprobe analysis (EPMA). Commercially pure Ti (CP Ti), Ti-6Al-4V (Ti64), and a relatively new Ti-5Al-5V-5Mo-3Cr (Ti5553) alloy were used in this investigation. Dissimilar titanium alloys were butt welded, resulting in various welding combinations, i.e. CPTi/Ti64, CP Ti/Ti5553 and Ti64/Ti5553 which were analyzed with the above techniques. The performed studies show complex deformation patterns during testing of EBW titanium samples.

Keywords: Material characterization, Dissimilar titanium, Electron beam welding

Introduction

There is a need to optimize the engineering and economical performance of titanium products which find increasing use in aerospace, biomedical and petrochemical applications. One way of tailoring titanium properties is through welding of dissimilar titanium alloys. However, the deformation behaviour of such welded components is unknown. Therefore, an extensive analysis of the deformation behaviour of Electron Beam Welded (EBW) dissimilar titanium alloys was performed.

Previous works on material characterisation of EBW dissimilar titanium alloys involving Ti-6Al-4V (Ti64) and Ti-5Al-5V-5Mo-3Cr (Ti5553) revealed that the weld zone was susceptible to cracking during tensile testing (Mitchell et al., 2010). The strain measured over a 25mm gauge length (total strain) was 1% and was accompanied by a tensile strength of about 900 MPa. It is worth noting that Ti64 and Ti5553 alloys have comparable tensile strengths, which are 983 MPa and 1053 MPa, respectively. However, EBW specimens of commercially pure titanium (CP Ti) and Ti64 (CP Ti/Ti64) as well as CP Ti and Ti5553 (CP Ti/Ti5553) fractured at the base metal of CP Ti due to its lower strength of which is approximately 690 MPa [1]. The total strain measured on the CP Ti/Ti64 and CP Ti/Ti5553 was between 15 and 20%. Note that all these strain values were measured within the total gauge length, and not specifically within the weld areas or their vicinities. One should remember that there are five distinct regions within the gauge length in dissimilar metal weld joints, namely base metal of two dissimilar alloys, the heat affected zone (HAZ) of two alloys and a fusion zone.

Mitchell et al. (2010) presented micrographs of fracture surfaces from a scanning electron microscope (SEM), showing microvoid coalescence (dimples) rather than typical brittle fracture characteristics on all samples including those that fractured at strains of 1%. This observation led to the interest in localized strain measurements during deformation in the vicinity of the weld area. Tensile testing was selected as a method of studying strain distribution of butt joints comprising of various titanium alloys; the same phenomenon during metal forming operations, such as taylor welded blanks are also studied in this manner.

Strain distribution within a sample during tensile testing can be measured using various techniques such as (i) clip-on extensometers, (ii) directly-mounted strain gages, (iii) optical devices, and (iv) video extensometers. The first two are categorised as contact, and the last two are categorised as non-contact methods. Both the optical and the video extensometers are fairly useful if strain distribution on a particularly small area of interest is to be determined.

Aramis - a system combining a non-contact 3D image correlation photogrammetry, a pair of high speed cameras and a computer/software (Tyson et al., 2002), was employed to measure the full field strain distribution in the vicinity of the welds between EBW dissimilar titanium during tensile testing. The frequency at which images are captured can be varied depending on the resolution needed and time allowed per test. In order for the computer software to measure strain, it must be able to track reference points. This is made possible by spraying a high contrast pattern on the test specimens. The pattern is typically composed of a white background underneath relatively small, uniform black spots. The Aramis software allows the user to define the reference points and then tracks them throughout the test. Once the test is completed and images are captured, the data can be stored for post processing. This feature is one of the main advantages associated with the Aramis software (Tyson et al., 2002).

Methods

Three different types of titanium were used in this investigation. They were commercially pure titanium (CP Ti), Ti6Al4V (Ti64) and a relatively new aerospace titanium alloy known as Ti-5Al-5V-5Mo-3Cr (Ti5553). These materials represent three different classes of titanium, namely unalloyed (CP Ti), α/β alloy (Ti64) and β-alloy (Ti5553). Their chemical compositions are shown in **Table 1**. The CP Ti and Ti64 were supplied in a 1.6 mm thick sheet. The Ti5553 was supplied as 7 mm thick plate and was reduced down to 1.6 mm thick using electronic discharge machining (EDM). Before welding, the joint edges were filed, cleaned with a dedicated Scotch-Brite® pad and then cleaned with acetone. Autogenous butt welds were made in the down-hand position using a 150kV welding voltage, a traverse speed of 8.5mm/s and welding current of 3.0 mA. The beam was focused on a targeting block before welding giving the smallest, most localised, intense spot of about 2 mm.

Following welding, metallographic samples and tensile test specimens were machined in the perpendicular direction to the welded joints. Standard metallographic preparation was performed on the welded samples consisting of grinding from 120 grit to 2400 grit SiC paper, polishing to 0.05μm SiO_2, then etching with Krolls etchant (100 mL water + 2 mL HF + 5 mL HNO_3). Light optical microscopy was used to characterize the macro- and microstructures on the weld zones and the base metals. Hardness profile across the welds were made using the Vickers scale with a load of 300g ($HV_{0.3}$). A scanning electron microscope was employed to reveal the grain structures and to study the fracture modes of the tensile tested samples. Compositional variations across the welds from one base metal to the other base metal were measured using JEOL 733 SuperProbe operated at 15kV and 20nA.

Table 1. Chemical composition of the titanium (wt.%).

Elements	CP Ti	Ti64	Ti5553
Ti	Bal.	Bal.	Bal.
Al	0.16	6.08	5.03
V	<0.01	3.85	5.1
Mo	<0.01	<0.01	5.06
Cr	<0.01	0.02	2.64
Fe	0.22	0.17	0.38
C	0.01	0.02	0.01
O	0.28	0.05	0.14
N	0.01	<0.01	<0.01

The tensile specimens were tested at room temperature with special attention given to the weld area. Two cameras of a Trilion (3D image capturing) system were dedicated to record the localized deformation (i.e. elongation) and Aramis software was used to calculate the localized strains within the vicinity of the weld area. An image collection interval of one second was used throughout all of the experiments conducted in this study. Two subsize tensile specimens (ASTM E 8M – 04) were made from each weldment combination **(Table 2)** with the weld located transversely in the center of the gauge length. The tensile tests were conducted with a crosshead speed of 3 mm/min and a 100kN load cell.

Results

Optical micrographs from the three weldments showing the base metal, HAZ and fusion zones are given in **Fig. 1** to **3**. Representative microstructures of the CP Ti/Ti5553 weld are provided in **Fig. 1**. The base metal of CP Ti clearly shows equiaxed grains with an average grain size of about 20 μm. α-phase is dominant in the base metal. Acicular α and α-prime (martensite) can be seen around the HAZ and the fusion zone. The latter is due to increasing martensite formation elements diffusing from Ti5553. The fusion lines are fairly distinct **(Fig. 1 b,c,d)** and the grain size increases towards the fusion zone. A lamellar structure is clearly present in the fusion zone **(Fig. 1c)**. The β phase grains are equiaxed. The grains in the HAZ grow in an epitaxial manner into the fusion zone. The grain size decreases towards the Ti5553 base metal.

Table 2. Results of Tensile Testing.

Welding combinations	UTS or Premature Fracture Strength (MPa)	YS (MPa)	Total Elong. at Fracture (MPa)	Localized Def. in the Weld Vicinity (%)	Fracture Location ***
CPTi/Ti64	505	400	26	2	BM CPTi
CPTi/Ti5553	505*	400	18**	2	BM CPTi
Ti64/Ti5553	744*	715	12	10	FZ

* Indicates premature fracture before necking
** Indicates adjustment of strain due to grip settling
*** BM = base metal; FZ = fusion zone

Fig. 2 shows the CP Ti/Ti64 weldment. The locations of the fusion lines for this specimen are not very clear due to the similar microstructural features in the HAZs and fusion zone as well as the significant grain coarsening in the HAZ (which results in large β grains in this region). However, α-prime phases are very clear especially on the Ti64 side **(Fig. 2c)**. On the CP Ti side, martensite was evident around the fusion line, which dissapears towards the HAZ and base metal **(Fig. 2b)**. For Ti64/Ti5553 weldment **(Fig. 3)**, the fusion lines are very visible. Columnar grains are clearly evident in the fusion zone and epitaxial grain growth was also clear. Note that a cellular structure is very prominent in the fusion zones of both CP Ti/Ti5553 and CP Ti/Ti5553 weldments while it is not very clear in the CP Ti/Ti64 weldment. This is most likely due to stronger martensite formation occurring in the latter specimen. Transverse hardness profiles for the three specimens are provided in **Fig. 4** indicating substantial hardening of the fusion zone in the CP Ti/Ti5553 and Ti64/Ti5553 specimens.

A typical metallographic cross-section of an EBW sample is shown in **Fig. 5a**. The width of the weld zone is

between 1.5 mm (at the bottom) and 3 mm (at the top surface).

Fig. 5b shows the initial stage of the tensile specimen from the Aramis software. In comparison, **Fig. 5c** shows an example of the localized strain distribution at the gage length prior to fracture. It is clearly shown in **Fig. 5c** that strains were highly concentrated at the weld region. The recorded strain for this particular case was about 14.9% before the sample fractured. There is a need to analyze and compare total elongation to the localized elongation at the weld region since they represent different values for different material combinations (see **Table 2**).
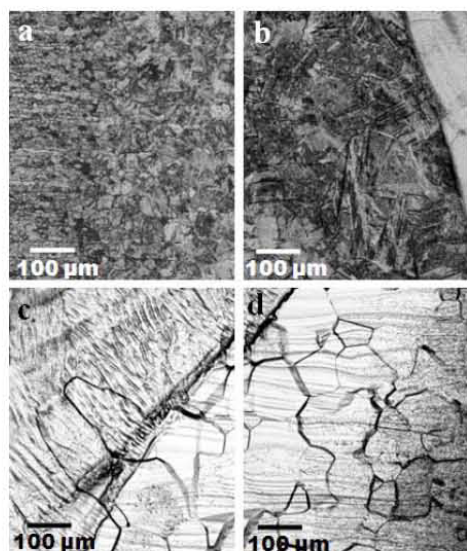
Figure 1. Photomicrographs of the CP Ti/Ti5553 as welded specimen (a & b: CP Ti base metal-HAZ and HAZ- fusion line, respectively; c & d: Ti5553 weld zone-fusion line and HAZ-base metal, respectively).
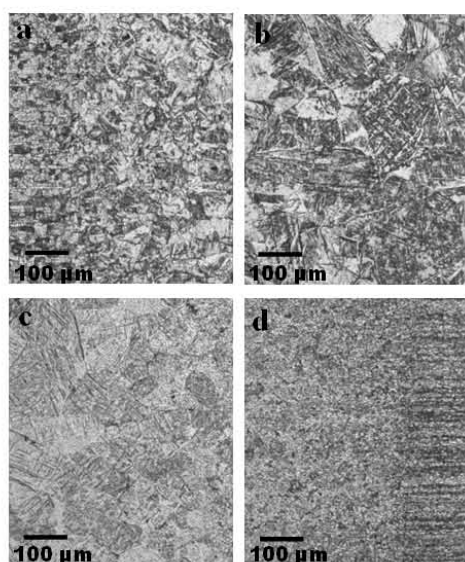
Figure 2. Photomicrographs of the CP Ti/Ti64 as welded specimen (a & b: CP Ti base metal-HAZ and HAZ- fusion line, respectively; c & d: Ti64 weld zone-fusion line and HAZ-base metal, respectively).
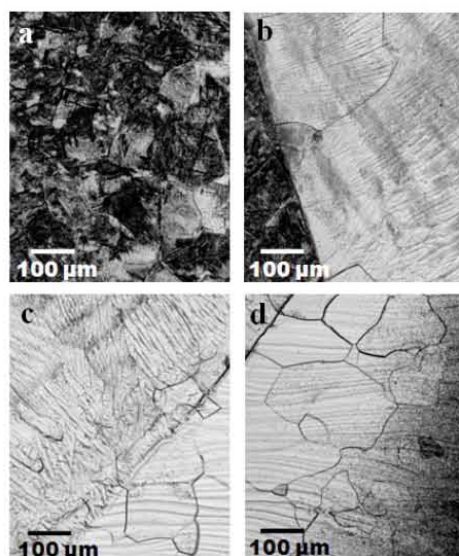
Figure 3. Photomicrographs of the Ti64/Ti5553 as welded specimen (a & b: Ti64 base metal-HAZ and HAZ- fusion line, respectively; c & d: Ti5553 weld zone-fusion line and HAZ-base metal, respectively)
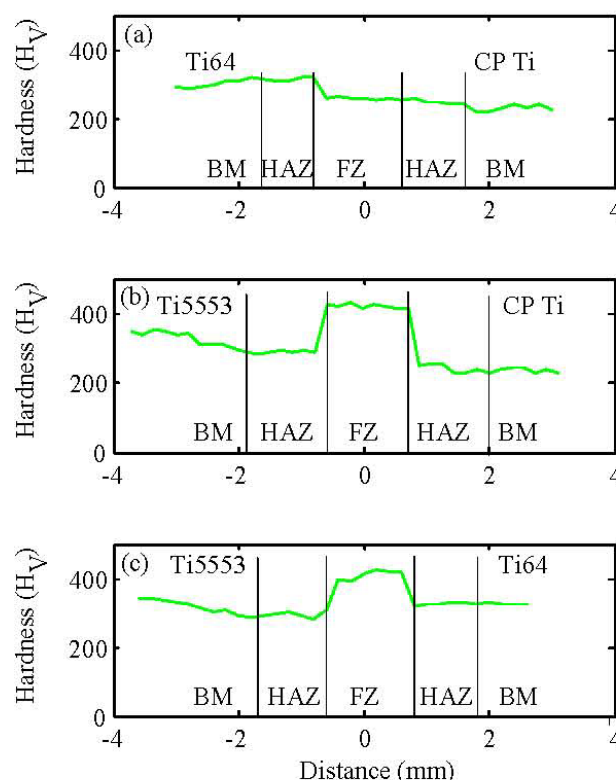
Figure 4. Hardness profile across the welds of (a) CP Ti/Ti64, (b) Ti5553/CP Ti, (b) and (c) Ti5553/Ti64 welds.

The results of an investigation into the compositional variations across the weld zone for each specimen is given in **Fig. 6**. It can be seen that there is a sharp drop in composition in the weld zones towards the base metal of CP Ti on the CP Ti/Ti64 and CP Ti/Ti5553 weldments.

SEM images of CP Ti/Ti5553 and Ti64/Ti5553 are provided in **Fig. 7a** and **7b** respectively, revealing microvoid coalescence on the fracture surface. It should be noted that

the CP Ti/Ti64 specimens fractured at the CP Ti base metal, such that the fracture surface for this specimen is similar to **Fig. 7a**.
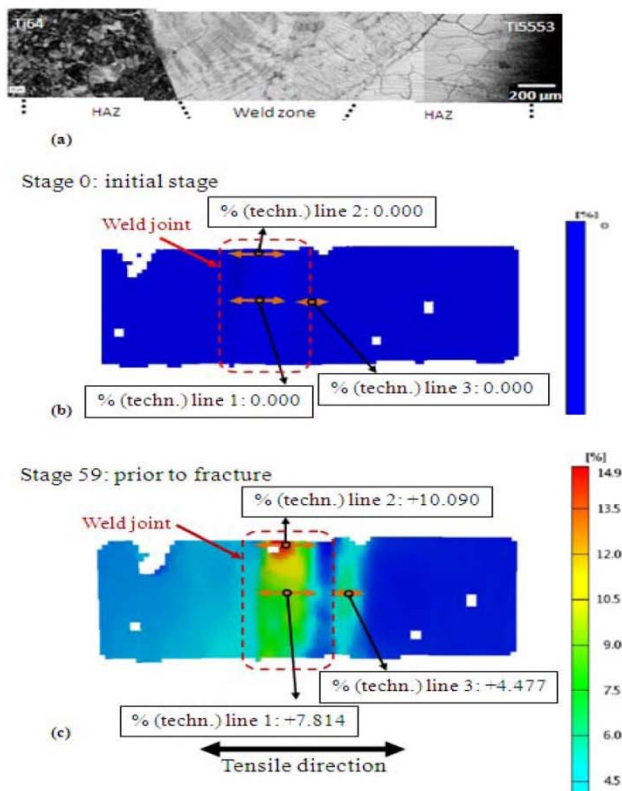
Figure 5. Images showing (a) a photomicrograph of a weld cross section, (b) initial stage prior to sample being pulled, and (c) highly localized strains at the weld zone. All images correspond to the as-welded Ti64/Ti5553 specimen.
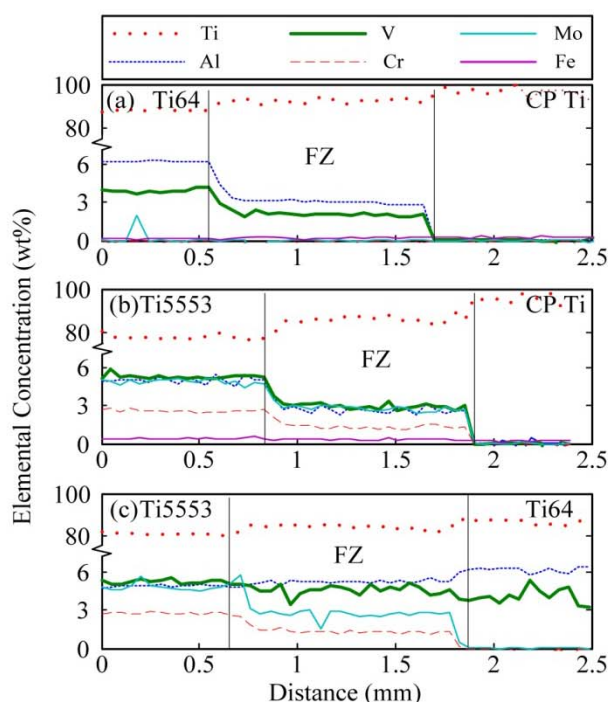
Figure 6. Elemental concentration (wt.%) profile across the welds of (a) CP Ti/Ti64, (b) Ti5553/CP Ti, (b) and (c) Ti5553/Ti64 welds.
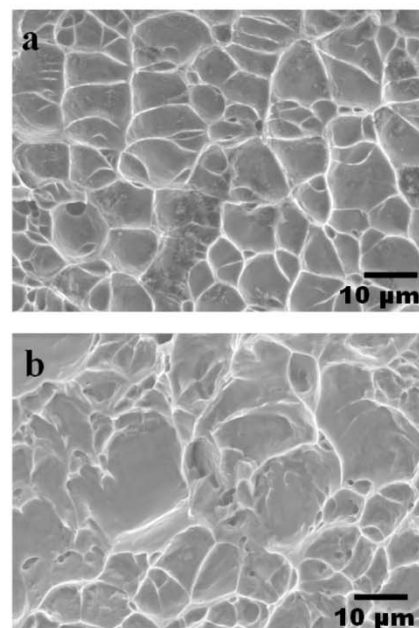
Figure 7. SEM images of (a) CP Ti/Ti5553 and (b) Ti64/Ti5553 showing microvoid coalescence fracture characteristics. Note that CP Ti/Ti64 specimen fractured at the CP Ti base metal, so the fracture characteristic is similar to (a).

Discussion

Welding of dissimilar titanium alloys have not been studied extensively. Liu et al. (1994) investigated the welding characteristics of Ti6Al4V and Beta-C^{TM} (Ti3Al8V6Cr4Mo4Zr) alloys. It was observed that (i) the solidification mode changed from cellular-growth to cellular-dendritic typed, (ii) steepend compositional gradients especially at the fusion line, (iii) hardness of HAZ at Ti6Al4V side was higher than that of Beta-C^{TM} side. The first two were associated with higher solute content of the Beta-C^{TM} compared to Ti6Al4V alloy, while the latter was related to the ability of Ti6Al4V to transform from beta-phase to alpha-prime (martensite) upon quenching. Similar observations were obtained in this work. Furthermore, it is worth mentioning that in the present work the lower hardness in HAZ of CP Ti as well as Ti5553 was attributed to completely opposite mechanism i.e. lack of solute in CP Ti to transform to martensite and too much solute (beyond the martensitic transformation line) in Ti5553.

The EBW process produces a relatively narrow weld zone, i.e. in these cases ≤ 3 mm width. Therefore, any strain that occurred within this area is extremely difficult to measure.

The reduced elongation of dissimilar weldments compared to similar weldments and ductile fracture surfaces may be explained with consideration of the five distinct regions of the dissimilar weldments. In composite weldments with base materials that have a significant yield strength mismatch, the base-material and HAZ of the weaker base-material will undergo significant plastic deformation and work-hardening before the base-material and HAZ of stronger base-materials are plastically de-

formed. Therefore, such specimens can be expected to have reduced elongation than weldments comprising similar and comparable base-metals as well fracture occurring in the weaker, more ductile, however work hardened material.

However, in composite weldments with base materials that have matching yield strengths, strain can be localised in region within the fusion zone or HAZ if they have comparably low strength (i.e. the weakest link). Such behaviour was observed for the Ti64/Ti5553 specimen where the majority of the strain was observed to occur in the fusion zone **(Fig. 5c)**. It is interesting to note that the fusion zone of the Ti64/Ti5553 specimen was significantly harder than the either base metal suggesting hardness does not compare well with strength and that slip mechanism in this region are particularly active. Future studies could investigate the mechanical behaviour of an all-weld specimen for this material using micro tensile specimens.

Localized strain on a welded part is important for design purposes, e.g. to know the ductility and fatigue resistance of the welds. If one is to determine localized strain during tensile testing of an EBW sheet, the non-contact type measurements are an appropriate option. Welding characteristics of the titanium alloys investigated are completely different; unalloyed titanium (CP Ti) is the easiest to weld and beta titanium is the most difficult to weld. The main challenge of fusion welding dissimilar titanium alloys arises from differences in chemical composition between the alloys. The resultant fusion zone has vastly different structures and properties compared to either base-metal. A concentration gradient develops and solute redistribution occurs. The solutes at higher concentrations (Ti, Al, V, Mo and Cr) will diffuse towards the side with a lower concentration.

Conclusion

With the assistance of the Aramis system, we have observed noticeable ductility within the weld area reaching up to 14.9%. This information shows a higher degree of complexity for different combinations of materials resulting in fracture mostly in the weld region. However, a more detailed study of the relationship between EBW and the resulting microstructure is needed.

Acknowledgement

References

Liu, P.S., Baeslack III, W.A., Hurley, J., 1994. Welding Journal, Research Supplement 73 (7), p. 175-s.

Lütjering, G. and Williams J.C., 2003. Titanium, Berlin Springer, p. 23-42.

Mitchell, R., Short, A., Pasang, T., Littlefair, G., 2010. Characteristics of EBW Ti Alloys, Structural Integrity and Failure - SIF, University of Auckland.

Tyson, J., Schmidt, T., Galanulis, K., 2002. Advanced Photo- grammetry for Robust Deformation and Strain Measurement. Proceedings of SEM 2002 Annual Conference, Milwaukee, WI.

Appendix F-4: Proceedings, 4th Manufacturing Engineering Society International Conference 2011, Cadiz, Spain.

Metallurgy and Deformation of Electron Beam Welded Similar Titanium Alloys

Timotius Pasang[(1)], Joseph C. Sabol[(2)], Wojciech Z. Misiolek[(2)], Ryan Mitchell[(1)], Andrew B. Short[(3)], Guy Littlefair[(4)]

[(1)]Dept. of Mechanical & Manufacturing Engineering, AUT University, Auckland – New Zealand
tpasang@aut.ac.nz
[(2)]Institute of Metal Forming, Lehigh University, Bethlehem, Pennsylvania - USA
[(3)]Melt Tools Ltd and AUT University, Auckland - New Zealand
[(4)]School of Engineering, Deakin University, Geelong - Australia

ABSTRACT

Butt welded joins were produced between commercially pure titanium and various titanium alloys using an electron beam welding technique. The materials used represent commercially pure grade, α-β alloy and β alloy. They were CP Ti, Ti-6Al-4V (Ti64) and Ti-5Al-5V-5Mo-3Cr (Ti5553), respectively. Grains were largest in the FZs of the different weldments, decreasing in size towards the heat affected zones (HAZs) and base metals. Hardness measurements taken across the traverse cross-sections of the weldments were constant from base metal-to-weld-to-base metal for CP Ti/CP Ti and Ti64/Ti64 welds, while the FZ of Ti5553/Ti5553 had a lower hardness compared with the base metal. During tensile testing the CP Ti/CP Ti weldments fractured at the base metal, whereas both the Ti64/Ti64 and Ti5553/Ti5553 broke at the weld zones. Fracture surface analysis suggested microvoid coalescence as the failure mechanism. The compositional analysis showed a relatively uniform distribution of solute elements from base metal-to-weld-to-base metal. CP Ti has always been known for its excellent weldability, Ti64 has good weldability and, preliminary results indicated that Ti5553 alloy is also weldable.

Keywords: electron beam welding, titanium, Aramis system

RESUMEN

Las soldaduras a tope se producen normalmente utilizando titanio puro y varias aleaciones de titanio, mediante el uso de la técnica del haz de electrones. Los materiales utilizados en este estudio representan a un grado puro, aleación α-β y aleación β. Concretamente, estos materiales fueron CP Ti, Ti-6Al-4V (Ti64) y Ti-5Al-5 v-5Mo-3Cr (Ti5553), respectivamente. Se vio que los granos eran mayores en las zonas de fusión de las diferentes soldaduras, disminuyendo en tamaño hacia las zonas afectadas térmicamente y los metales base. Las mediciones de dureza a través de las secciones transversales fueron constantes para las soldaduras con CP Ti/CP Ti y Ti64/Ti64, mientras que la zona de fusión del Ti5553/Ti5553 tuvo una menor dureza en comparación con el metal base. Durante las pruebas de resistencia, las soldaduras CP Ti/CP Ti se fracturaron en el metal base, mientras que las soldaduras Ti64/Ti64 y Ti5553/Ti5553 lo hicieron en las zonas de soldadura. Los análisis de fractura mostraron que la posible causa de estas roturas era la coalescencia de microcavidades. El análisis posterior de la composición mostró una distribución relativamente uniforme de elementos de metal de base para soldadura a base de metal. CP Ti siempre ha sido conocido por su excelente soldabilidad, Ti64 tiene buena soldabilidad y los resultados preliminares indican que la aleación Ti5553 también puede ser soldada.

Palabras clave: soldadura por haz de electrones, titanio, sistema Aramis

1. Introduction

Welding of titanium and its alloys is generally performed in a controlled atmosphere due to high reactivity at temperatures above 500°C [1]. Electron beam welding (EBW) is one of the best methods to weld titanium. EBW provides a fully controlled atmosphere to avoid the presence impurities or interstitial elements, and embrittlement associated with oxygen or hydrogen. It is generally agreed that fusion zones (FZs) and heat affected zones (HAZs) are more susceptible to cracking/fracture compared with the base metal during deformation. Therefore, the deformation characteristics of these areas during tensile testing were investigated using optical metrology.

Welding characteristics of CP Ti have been investigated by many researchers. Some of the most significant observations are summarized in the following section. Lathabai et al. [2] conducted GTAW on CP Ti Grade 2 using keyhole and conventional methods. They reported columnar grains in the fusion zone (FZ) which were significantly coarser than those observed in the HAZ and base metal. The columnar grains in the fusion zone were a result of epitaxial growth from the HAZ. The HAZ consisted of equiaxed transformed β grains which increase in size as the FZ is approached. Within these grains, colonies of α-phases were present. Interestingly, despite all the differences in the microstructures (size and phase) between the welded and the unwelded samples, the hardness and tensile test results were comparable. Note that all the tensile samples fractured at the weld area. Lynch et al. [3] conducted failure analysis of aircraft ducts made of 0.5mm and 0.8 mm thick CP Ti Grade 3. In the HAZ, the thinner section had coarse acicular α whereas the thick section had needle-like α phase. It was stated that even though the base metal exhibited equiaxed α-phase while the HAZ exhibited acicular α, there was no significant hardness different between these two areas. Gorinin et al. [4] reported a huge difference in microstructures between fast-cooled (500°/sec) and slow-cooled (20°/sec) CP Ti samples. The fast-cooled sample had needle (martensite-like structure) and lamellar-shaped α-phase, while the slow-cooled sample showed a coarse acicular α with serrated boundaries.

Research on Ti6Al4V (Ti64) including its weldability has been the subject of research since this alloy was introduced in the late 1950s. The Ti64 alloy is used in more than 50% of all applications that employ titanium and its alloys thereby proving its versatility. Irisarri et al. [5] indicated the presence of a small amount of acicular α and larger amount of α-prime (martensite) in the HAZ of Ti64 welds. α-prime covers the entire FZ. Huiquang et al. [6] studied the effect of heat input on the microstructure and fracture behaviour of Ti64. They observed columnar grains oriented perpendicular to the direction of the radial fusion boundary. It was also concluded that the amount of lamellar structure increases (decreasing quantity of equiaxed grains) with heat input. Hardness profiles showed an increased in hardness in the FZ compared with the base metal. Furthermore, micropores were detected, and were claimed to be associated with low vacuum during the electron beam welding process or poor cleanliness of the base metal surface. It was argued that the increased hardness, hence less ductile, coupled with the presence of micropores contributed to the fracture in the weld region. The tensile tested samples fractured transgranularly with fine dimples on the fracture surface. High FZ hardness due to the presence of α-prime was also reported by Rao et al. [7].

Although relatively limited, investigations on weldability of a few beta-titanium alloys have also been conducted by various researchers [8-10]. It was reported that large, columnar grains were present in the FZs, and smaller and nearly equiaxed grains in the HAZ. The grain size was found to decrease towards the base metal. Becker and Baeslack [10] studied the propertiesand microstructure of three metastable titanium alloys, i.e. Ti-15V-3Cr-3Al-3Sn (Ti15-333), Ti8V-7Cr-3Al-4Sn-1Zr (Ti87341)and Ti-8V-4Cr-2Mo-2Fe-3Al (Ti84223) and revealed lower strength in the weld zones compared with the base metals. Fracture modes of the weldments indicated transgranular microvoid coalescence.

In the current investigation, butt welded joins were produced between commercially pure titanium and various titanium alloys using an electron beam welding technique. The materials used were commercially pure titanium (CP Ti), Ti-6Al-4v (Ti64) an alpha-beta alloy and Ti-5Al-5V-5Mo-3Cr (Ti5553), a beta alloy. On the one hand, even though fusion welding characteristics of CP Ti and Ti64 have been studied extensively only a few have published their EBW characteristics. Welding characteristics of Ti5553, on the other hand, have not been reported elsewhere.

In order to determine the localized strain in the vicinity of the EBW welds during tensile testing in this study, a non-contact 3D image correlation photogrammetry system known as ARAMIS was used. ARAMIS employs a pair of high speed cameras and a computer/software to measure the full field strain and two dimensional strain distributions during tensile testing [11]. In order for the computer software to

measure strain, it must be able to track reference points. To do this, a high contrast pattern is sprayed on the test specimens. The pattern is typically composed of a white background underneath relatively small, uniform black spots. The ability of the ARAMIS system to capture the deformation/strain on the samples depends on the quality of the background pattern. The ARAMIS software allows the user to define the reference points and then tracks them throughout the test. Once the test is completed and images are captured, the data can be stored for post processing. This feature is one of the main advantages associated with the ARAMIS software [11].

2. Experimental Procedure

2.1. Materials

Three different types of titanium representing unalloyed, α/β alloy and β-alloy were butt welded using an Electron Beam Welder. They were commercially pure Ti (CP Ti), Ti-6Al-4V (Ti64), and Ti-5Al-5V-5Mo-3Cr (Ti5553) alloys, respectively. The CP Ti and Ti64 materials were supplied with a thickness of 1.6 mm while the Ti5553 alloy had a thickness of about 8 mm. The Ti5553 samples were reduced to 1.6 mm thick.

2.2. Electron Beam Welding

Autogenous butt welds were made in the down-hand position using 150kV welding voltage, a traverse speed of 8.5mm/s and welding current of about 3 mA. The beam was focused on a targeting block before welding giving the smallest, most localised, intense spot. Prior to welding the joint edges were filed, cleaned with a dedicated Scotch-Brite® and then cleaned with acetone.

2.3. Metallography and Microscopy

Following welding, samples were sectioned and prepared accordingly for optical microscopy, hardness and tensile testing, and electron microscopy. Standard metallography practice was performed on the welded samples consisting of grinding from 120 up to 2400 SiC paper, polishing up to $0.3\mu m$, followed by final polishing with colloidal silica suspension. The samples were then etched with Krolls reagent (100 mL water + 2 mL HF + 5 mL HNO_3). Light optical microscopy was used to characterize the microstructures of the weld zones and the base metals. Compositional variations across the welds i.e. from the base metal to FZ were measured using a JEOL 733 SuperProbe operated at 15kV and 30nA along the mid-thickness position.

2.4. Mechanical Testing

Microvickers hardness tester ($HV_{0.3}$) was used to reveal the hardness across the welds of metallograhically-prepared samples. Tensile test specimens were machined in the perpendicular direction to the welded joints. Two subsize tensile specimens (ASTM E 8M – 04) were made from each weld joint with the weld located transversely in the centre of the gauge length. The tensile tests were conducted at room temperature with a crosshead speed of 3 mm/min and a 100kN load cell. Two cameras were dedicated to record the localized deformation (i.e. elongation) and ARAMIS, a non-contact 3D image correlation photogrammetry system, was used to calculate the strains within the vicinity of the weld area. An image collection interval of one second was used throughout all of the experiments conducted in this study. The fracture surfaces were further examined using a scanning electron microscope to reveal their fracture modes.

3. Results and Discussions

The FZ width of EBW is approximately 2 mm on the top surface and around 0.8 mm at the bottom. For comparison, MIG and TIG welds would produce a weld zone width between 3 to 4 mm for the same sheet thickness.

Figure 1 shows the microstructure from the base metal to the weld zone of the three weldments. The base metal of CPTi consists of equiaxed α-grains with an average size of 10 μm. Acicular alpha phases are observed from the HAZ to the FZ with larger grain size compared with the base metal (Figure 1a). In the FZ, with grain size of up to 200 μm, fine acicular alpha were evident (Figure 1b). Note that fine acicular alpha can be mistaken for α-prime (martensite).

Figures 1c and d show the microstructures of the base metal, HAZ and FZ of the Ti64/Ti64 weldment. Grains in the HAZ were slightly larger than those in the base metal, and the grain size increased

significantly in the FZ. α-prime (martensite) was faintly observed in the HAZ and is very clear in the FZ. The formation of martensite in Ti64 is associated with fast cooling rates from melting, such as in EBW.

For the Ti5553/Ti5553 weld, large columnar grains and epitaxial grain growth were observed in the FZ. The grains consist of cellular-dendritic type structures which are associated with constitutional supercooling during solidification. The higher solute content in Ti5553 alloy associated with alloying elements i.e. Al, V, Cr and Mo, effectively increases the degree of constitutional supercooling. Furthermore, cellular solidification is likely to take place, and cells are clearly observed in the Ti5553/Ti5553 weld. This is further enhanced by the absence of a martensitic transformation in the Ti5553 alloy. CP Ti does not have a sufficient solute content to induce celular solidification or a martensitic transformation, while the martensitic transformation in Ti64/Ti64 weld obscures observation of both the cellular and epitaxial growth. The HAZ has retained beta phase with equiaxed grains. The degree of grain coarsening increases from the base metal to the FZ.
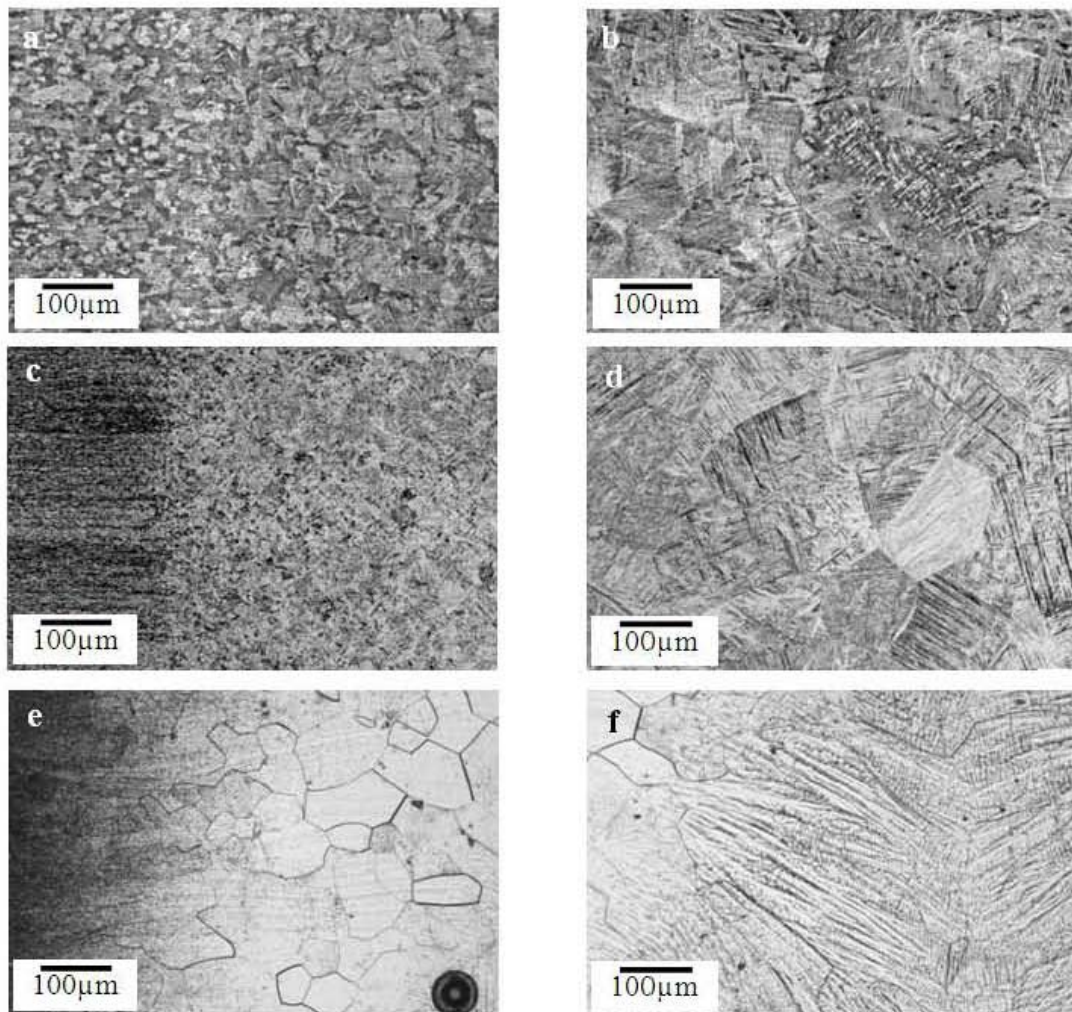

Figure 1. *Photomicrographs showing microstructures of CP Ti/CP Ti (a & b), Ti64/Ti64 (c & d), and Ti5553/Ti5553 (e & f). a, c and e correspond to base metals and HAZs, while b, d and f are of FZs. Note a pore on the Ti5553/Ti5553 HAZ/FZ boundary.*

Hardness values were relatively constant across the welds except for Ti5553/Ti5553 where lower hardness was observed in the FZ and HAZ (Figure 2). Similar results have been reported elsewhere [12]. The cause of this low hardness, hence strength, in the weld zone of Ti5553/Ti5553 welds is unclear. However, the cause may be associated with the dissolution of alpha phase in the FZ and HAZ, leaving only retained beta phase, leading to a reduced hardness in these regions. For both CP Ti/CP Ti and Ti64/Ti64 welds, the relatively plateau hardness values from the base metal-to-welds-to-base metal were associated with lack of solutes and abundance of solutes, respectively.

140

Table 1 presents a summary from the tensile testing of both the unwelded and welded samples. Interestingly, the CP Ti/CP Ti welds fractured at the base metal and not on the weld zones as the other two (Ti64/Ti64 and Ti5553/Ti5553) welds. The weld zones showed fairly high ductility where its elongation could reach up to 76% of the total elongation.
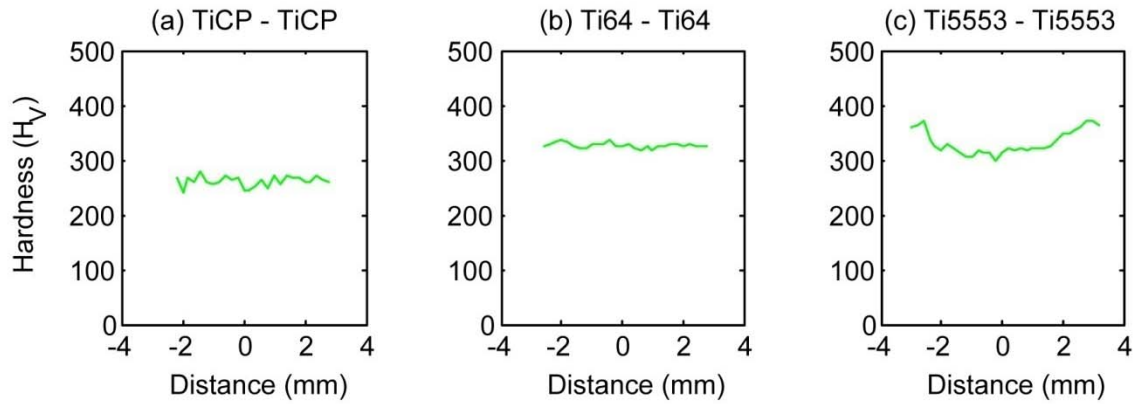

Figure 2. Hardness profiles of the three welding combinations

Table 1. Mechanical properties of base metals (BM) and weldments

|	Yield Strength (MPa)	Ultimate Tensile Strength (MPa)	Total Elongation at Fracture (%)	Localized deformation in the vicinity of the welds (%)	Fracture Locations
CP Ti - unwelded	630	693	27	N/A	BM
Ti64 - unwelded	941	983	13	N/A	BM
Ti5553 - unwelded	1028	1053	12	N/A	BM
CP Ti/CP Ti	425	550	37	20	BM
Ti64/Ti64	720	770*	13	10	WZ
Ti5553/Ti5553	N/A	680*	11	4	WZ

* these results are slightly lower than previously reported; BM = base metal; WZ = weld zone
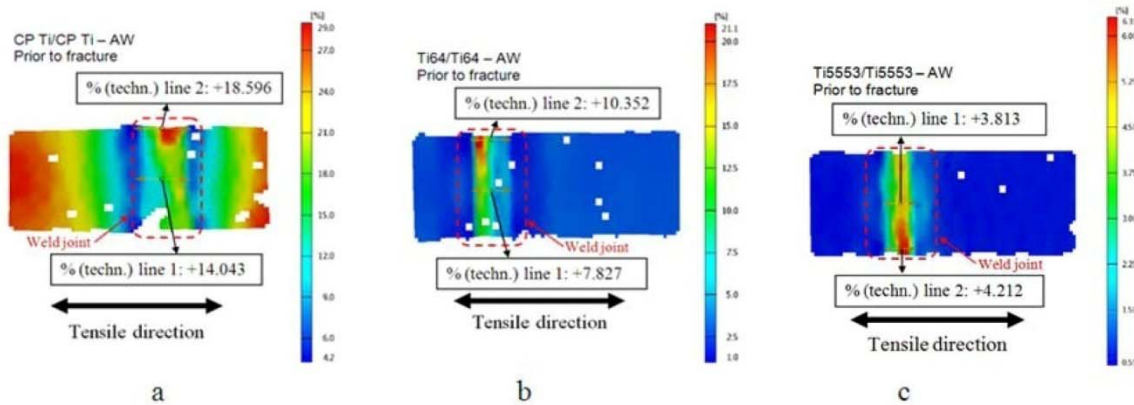
Figure 3. Strain distributions across the welds on the as-welded (a) CP Ti/CP Ti, (b) Ti64/Ti64, and (c) Ti5553/Ti5553 alloy.

The images from Aramis (Figure 3) strongly indicated the strain localization in the weld zone for all the welds combination. The CP Ti/CP Ti weld, additionally, had high strain distributions outside the weld zone where fracture eventually occured. The maximum localized strain distribution across the welds are approximately 18.6%, 10.4%, and 4.2% for the CPTi/CPTi, Ti64/Ti64, and Ti5553/Ti5553 welds respectively. The strain distributions across the center of the CPTi/CPTi, Ti64/Ti64, and Ti5553/Ti5553 welds are 14.0%, 7.8%, and 3.8% respectively. This trend in decreasing strain distribution between the three different alloys can be attributed to the increasing amounts of solute elements in Ti64 and Ti553.

As the amount of solutes increases, the alloys will become stronger; however, more brittle. Therefore, the % elongation will decrease as shown in Table 1 and the amount of strain experienced in the weld until failure will also decrease.
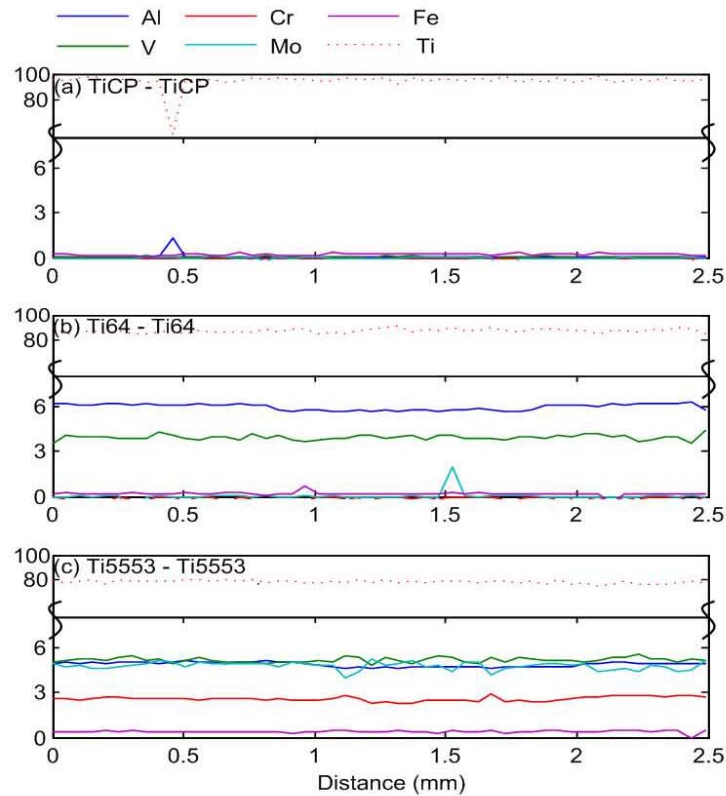
Figure 4. Compositional analysis across the welds of the three welding combinations

The EPMA results (Figure 4) generally showed uniform distribution of the solute elements in both the weld zone and base metal. These would have been expected as the EBW process used in this investigation was autogeneous (no filler metal added). However, there is a clear loss of aluminium in the FZ of the Ti64/Ti64 and Ti5553/Ti5553 welds as summarized in Table 2. The preferential vaporisation of aluminium (and chromium to a lesser extent) is due to the low boiling temperature of aluminium i.e. about 2441°C compared with the other alloying elements. The vaporisation of certain elements during welding with the electron beam process is the key mechanism leading to the formation if the keyhole weld pool. Typically, high-vacuum EBW beams can be focused dow to spot sizes in the range of 0.010 to 0.050 inches in diameter, with a power density of 10^6 W/in^2. This high level of beam spot intensity is sufficient to to vaporize almost any material, forming a vapor hole that pentrates deep into the workpiece.

The CP Ti/CP Ti weldments fractured at the base metal rather than in the FZ with relatively high elongation. The Ti64/Ti64 and Ti5553/Ti5553 weldments fractured in the FZ/HAZ interface area, with the latter showing very little elongation (Figure 3c). This could be associated with the presence of "brittle" transgranular facets fracture on one half of the weld (adjacent to the top surface of the weld) with the bottom half showing evidence of microvoid coalescence (dimples) features (Figure 5c). At higher magnifications (1000x), the fracture surface of the "brittle" facets showed fine and shallow dimples indicating less ductility compared with the bottom surface.

Table 2. Summary of chemical composition from EPMA analysis

Weld	Mean aluminium (wt.%) Base metal	Mean aluminium (wt.%) FZ	Mean aluminium loss (%)
CP Ti/Cp Ti	Trace	Trace	N/A
Ti64/Ti64	6.09	5.70	-6.43
Ti5553/Ti5553	4.95	4.66	-5.92
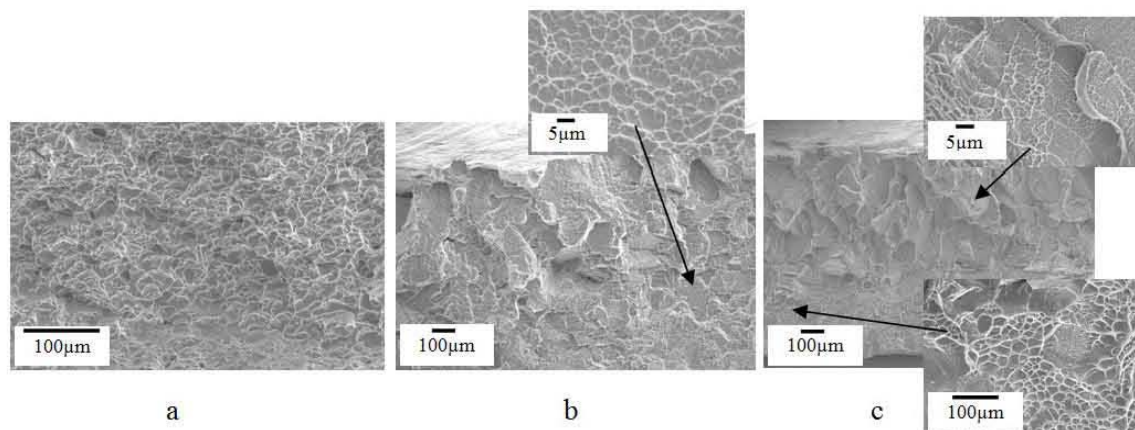
Figure 5. *SEM micrographs showing fracture surfaces of (a) CP Ti/CP Ti weld that fractured on the base metal, (b) Ti64/Ti64 weld, and (c) Ti5553/Ti5553 weld. Both Ti64/Ti64 and Ti5553/Ti5553 welds fractured in the weld zone. All fracture surfaces showed microvoid coalescence (dimples).*

4. Conclusions

Ti64 and Ti5553 alloys showed that they are prone to cracking/fracture at the welds area, while CP Ti did not. Both CP Ti and Ti64 have been known to exhibit excellent and good weldability, respectively, and Ti5553 alloy appears to be weldable. The ARAMIS system can be used to measure localized strain on a relatively narrow area such as weld zone. The weld zones appear to have fairly high ductility as shown in the ARAMIS results as well as the fracture surfaces.

5. Acknowledgements

6. References

[1] G. Lütjering, J.C. Williams, *"Titanium"*, Berlin Springer, 2003.

[2] S. Lathabai, B.L. Jarvis, K.J. Barton, *Comparison of Keyhole and Conventional Gas Tungsten Arc Welds in Commercially Pure Titanium*, Materials Science and Engineering A299, p.81–93, 2001.

[3] S.P. Lynch, B. Hole and T. Pasang, *Failures of Welded Titanium Aircraft Ducts*, Engineering Failure Analysis, 2 (4), p. 257-273, 1995.

[4] I.V. Gorinin, J.B. Florinsky and B.B. Chechukin, *The Development of the Structure and Mechanical Properties of Titanium Welds*, The Science, Technology and Application of Titanium, R.I Jaffee and N.E. Promisel (editors), Pergamon Press, p. 843-846, 1968.

[5] A.M. Irisarri, J.L. Barreda and X. Azpiroz, *Influence of the Filler Metal on the Properties of Ti-6Al-4V Electron Beam Weldments. Part I: Welding Procedures and Microstructural Characterization*, Vacuum 84, p. 393–399, 2010.

[6] Wu Huiqiang, Feng Jicai and He Jingshan, *Microstructure Evolution and Fracture Behaviour for Electron Beam Welding of Ti-6Al-4V*, Bulletin of Materials Science 27 (4), 387-392, 2004.

[7] K. Prasad Rao, K. Angamuthu, P. Bala Srinivasan, *Fracture toughness of electron beam welded Ti6Al4V*, Journal of Materials Processing Technology 199, p. 185–192, 2008.

[8] W. Hatch, *Investigation of the Weldability of Ti-8Mo-8V-2Fe-3Al*, Fall Meeting of AIME, Detroit, Michigan, 1971.

[9] M.A. Greenfield and C.M. Pierce, *Postweld Aging of a Metastable-Beta Titanium Alloy*, Welding Journal 52 (11), Research Supplement, p. 524-527, 1973.

[10] D. Becker and W.A. Baeslack III, *Property-Microstructure Relationships in Metastable-Beta Titanium Alloy Weldments*, Welding Journal 59 (2), p.85s-92s, 1980.

[11] J. Tyson, T. Schmidt, and K. Galanulis, *Advanced Photo- grammetry for Robust Deformation and Strain Measurements*, Proceedings of SEM 2002 Annual Conference, Milwaukee, WI, 2002.
[12] R. Mitchell, A. Short, T. Pasang and G. Littlefair, *Characteristics of EBW Ti Alloys*, Structural Integrity and Failure, SIF 2010, University of Auckland, 2010.